Summer 2018

A Stepwise Compression-Relaxation Testing Method for Tissue Characterization and Tumor Detection Via a Two-Dimensional Tactile Sensor

Yichao Yang
Old Dominion University, yyang007@odu.edu

A STEPWISE COMPRESSION-RELAXATION TESTING METHOD FOR TISSUE CHARACTERIZATION AND TUMOR DETECTION VIA A TWO-DIMENSIONAL TACTILE SENSOR

by

Yichao Yang
B.S. June 2009, Yantai University, China
M.E. June 2013, University of Electronic Science and Technology of China, China

A Dissertation Submitted to the Faculty of
Old Dominion University in Partial Fulfillment of the
Requirements for the Degree of

DOCTOR OF PHILOSOPHY

MECHANICAL ENGINEERING

OLD DOMINION UNIVERSITY
August 2018

Approved by:

Julie Zhili Hao (Director)

Stacie I. Ringleb (Member)

Siqi Guo (Member)

Krishnanand Kaipa (Member)

ABSTRACT

A STEPWISE COMPRESSION-RELAXATION TESTING METHOD FOR TISSUE CHARACTERIZATION AND TUMOR DETECTION BASED ON A TWO-DIMENSIONAL TACTILE SENSOR

Yichao Yang
Old Dominion University, 2018
Director: Dr. Julie Zhili Hao

This dissertation presents a stepwise compression-relaxation (SCR) testing method built upon a two-dimensional (2D) tactile sensor for mechanical characterization of soft tissues and tumor detection. The core of the 2D sensor entails one whole polydimethylsiloxane (PDMS) microstructure embedded with a 3×3 sensing-plate/transducer array. A soft sample was compressed by the 2D sensor with a step incremental depth at a ramp speed, and then relaxed for certain hold time. When a soft sample was compressed by the 2D sensor, the sensing-plates translated the sample response at different tissue sites to the sensor deflections, which were registered as resistance changes by the transducer array.

Instant elasticity ($E_{instant}$) and loss factor (tan δ) extracted from the measured data were used to quantify the sample elasticity and viscoelasticity, respectively. First, a three-way ANOVA analysis was conducted on the data of soft materials (PDMS/silicone rubbers) to evaluate the influence of testing parameters (incremental depth, hold time, and ramp speed) on the measured results. The results revealed that both $E_{instant}$ and tan δ were significantly dependent on testing parameters. Next, the measured results on the soft tissues showed different elasticity and viscoelasticity between muscle tissues and fat/skin tissues. The measured results on the tumor tissues indicated different elasticity and viscoelasticity among the five breast tumor (BT) tissues, and between the two pancreatic tumor (PT) tissues before and after treatment. Due to the

larger sample size of the BT tissues, the elasticity distribution among the measure BT tissue sites was used to determine the location, shape and size of the tumor in a BT tissue.

The correlation of stress drop ($\Delta\sigma$) (obtained from the difference between the instant and relaxed sensor deflections at each step incremental depth) with the applied strain (ε) was used for tumor detection. Pearson correlation analysis was conducted to quantitatively analyze the measured $\Delta\sigma$-ε relation as slope of stress drop versus applied strain ($m=\Delta\sigma/\varepsilon$) and coefficient of determination (R^2) as a measure of the goodness of fit of the linear regression for distinguishing tumor tissue from normal tissue. The measured results on soft materials showed that m was significantly dependent on testing parameters, but R^2 showed no significant dependency on testing parameters. The measured results on the tumor tissues indicated R^2 was significantly varied among the center, edge and outside sites of the BT tissues. However, no difference was found between the BT outside sites and the normal tissues. R^2 also revealed significant difference between before and after treatment of the PT tissues, while no difference between the PT tissues after treatment and the normal tissues. R^2 of the PT tissues before treatment was significantly different from that of the BT center sites, but m failed to capture their difference. Furthermore, dummy tumors made of silicone rubbers were found to behave differently from the native tumors.

In summary, the feasibility of the SCR testing method for tissue characterization and tumor detection was experimentally validated on the measured soft samples, including PDMS, silicone rubbers, porcine and bovine normal tissues, mouse BT and PT tissues. Future work will investigate the feasibility of the SCR testing method for differentiation between benign tumors and malignant tumors.

This dissertation is dedicated to my parents and wife.

ACKNOWLEDGMENTS

This work would never have been possible without all the support, encouragement, and inspiration of many people. I would like to take the opportunity to express my gratitude.

First and foremost, I would like to express my deepest appreciation to my advisor, Dr. Julie Zhili Hao, director of the Micro Devices and Micromechanics Laboratory (MDML), Old Dominion University. It has been an honor to be her Ph.D. student. Her enthusiasm and extraordinary view on research have made a deep impression on me. Dr. Hao has supported me not only by providing a research assistantship for five years, but also academically and emotionally through the bumpy road to finish this dissertation. This dissertation would not have been possible without her guidance and persistent help. I appreciate this great study opportunity provided by Dr. Hao, which broadened my mind and significantly affect my future career path.

My committee members guided me through all these years. I would like to thank Dr. Stacie I. Ringleb, Dr. Siqi Guo, Dr. Krishnanand Kaipa, and former committee member Dr. Helmut Baumgart, for their continuous support, encouragement, guidance, cooperation, and insightful comments.

Many special words and thanks should go to all the professors, classmates, and staff for their support during my Ph.D. study. They broadened my horizons and always helped me out when I got any difficulties. I want to thank our department of mechanical and aerospace engineering and Old Dominion University, for providing us with a good study environment. For this, I would like to give my sincere gratitude to the department chair Dr. Sebastian Bawab, GPD Dr. Miltos Kotinis, former GPD Dr. Han Bao, Dr. Abdelmageed Elmustafa, Dr. Dipankar Ghosh, and Dr. Shizhi Qian. I also want to thank Ms. Diane Mitchell, and Mr. June Blount for their kind support throughout my study at Old Dominion University. My thanks also go to my group members, Ms. Wenting Gu, Ms. Jiayue

Shen, Ms. Dan Wang, and Mr. Siqin Dong for sharing ideas, stories, and thoughts, for all the generous help in the device fabrication and tissue measurements, and for every beautiful moments we have spent together. The MDML group has been a source of friendships as well as good advice and collaboration.

My study and life experience over the past five years has helped build my character and turn me into a more mature person. My time at Old Dominion University was made enjoyable in large part due to many friends who became a part of my life. I would like to thank all the people who helped me grow. I am grateful for time spent with roommates, Mr. Liang Meng, Mr. Wenshuo Zhou, Mr. Yuan Lin, Mr. Siyuan Liu, Mr. Peijie Tang, Mr. Sihang Li, Mr. Tianqi Pan, Ms. Yu Duan, and Ms. Chi Li, for sharing peer opinion and giving me sincere encouragement. I am also hugely appreciative to Dr. Wenfeng Zheng, Dr. Xiaolu Li, and Dr. Shan Liu, especially for sharing their life experience and giving me the courage to chase my dream. It is my great honor to have friendships with these people being pure and good in their lives.

I gratefully acknowledge all my teachers at different stages of education for their devoted work in supervising and mentoring me.

Last, but by no means least, I would like to express my gratitude to my family for their love and encouragement. I want to thank my father and mother for supporting me in fulfilling my academic pursuit in a foreign country and respecting every decision I made. My parents formed part of my vision and taught me what is important in life. I owe my deepest gratitude to my loving, patient, encouraging and supportive wife Ms. Qing Huang, for her understanding of my pursuit towards my goal and aspirations. A special thanks to my father in law, mother in law, brother in law for their love. Their patience and sacrifice will remain my strength and inspiration throughout my life.

TABLE OF CONTENTS

Page

Page

LIST OF TABLES

Table Page

LIST OF FIGURES

Figure Page

Figure Page

Figure Page

Figure Page

CHAPTER 1

INTRODUCTION

1.1 Techniques for Tissue Characterization and Tumor Detection

Approximately 1.7 million new cancer cases are expected to be diagnosed in 2018, and an estimated 609,640 Americans are expected to die of cancer in 2018. Cancer is the second most common cause of death in the USA [1]. Thus, cancer diagnosis and treatments are of utmost importance, and the early detection and diagnosis is important for surviving this fatal disease. The earliest cancer signs are detectable by medical imaging often before symptoms appear [2]. To detect various forms of cancer, diagnosis is based on the information from anatomical imaging techniques, which include mammography (MG) [3], computer tomographic (CT) [4], and magnetic resonance imaging (MRI) [5], ultrasound [6], etc. [7]. MG, CT, and MRI are non-invasive. However, CT and MRI are expensive. MRI requires complicated system. The imaging resolution of ultrasound is low [7]. Therefore, non-invasive diagnostic methods with high sensitivity and specificity to reduce the cost and painful procedures would be beneficial for cancer diagnosis. Moreover, tumor treatments demand monitoring tumor progression and therapeutic responses, due to unpredictable significant variability among individuals [8].

By modifying the biological composition and structure, a tumor alters the tissue mechanical properties [2, 8]. In fact, the mechanical property that is known to be linked to the tumor formation is due to the modified structure of ECM proteins [8-11]. Many physical properties of the tumor-associated ECM are fundamentally different from those of normal tissue stroma. Based on several studies using atomic force microscopy (AFM) and micro-sensors, it is known that the stiffness of the epithelial and stromal layer in tumor tissue significantly differs from the normal tissue [12]. For example, tumor stroma is typically stiffer than normal stroma.

An important current area of cancer research is to determine whether biomechanical properties of ECM can provide more specific diagnostic information about the course of cancer-related processes, and thus serve to specify appropriate therapies and monitor therapeutic responses [8].

As such, the mechanical properties of a tumor have been intensively studied for their potential to provide specific diagnostic information about tumor status and progression, and consequently monitor therapeutic responses. Based on the rationale that mechanical properties of a tumor can serve as biomarkers of its biological features, noninvasive mechanical techniques have been aggressively pursued [2, 13-19].

Generally speaking, these mechanical techniques for tumor detection mainly fall into two categories: elastography and mechanical imaging. The first difference is that mechanical imaging (MI) reconstructs the internal mechanical structure of tissue using the data of stress pattern over the compressed tissue, while the elastography is based on detection of strain induced in the tissue by various static or dynamic mechanical stimuli. Therefore, MI are also called stress imaging, in contrast to other elastography techniques, which are used in estimating tissue displacement and referred to as strain imaging. The second difference is that the methods for obtaining 3D tissue images used in MI are much simpler than that used in elastography, and therefore MI is low cost and easy to use [20].

1.1.1 Elastography

Elastography, also referred as elasticity imaging, offers great potential to characterize cystic and solid breast tumor using a combination of standard ultrasound imaging and innovative software technology [21]. Elastography was developed in the late 1980s to early 1990s to improve the diagnostic value of ultrasound imaging [20]. The success of ultrasound elastography has inspired other investigators to develop analogs based on other imaging modalities [20], such

as the magnetic resonance elastography [22, 23], and the optical coherence tomography elastography [16, 24, 25]. There are mainly two categories of elasticity imaging: compression or strain elastography, and shear wave Elastography. Compression elastography is a qualitative method that measures stiffness based on soft tissue distortion caused by minimal manual compression. Conversely, shear wave elastography is a quantitative method that uses an acoustic radiation force pulse sequence to generate shear waves, which propagates perpendicular to the ultrasound beam, and causes transient displacements. The distribution of shear-wave velocities at each pixel is directly related to the shear modulus, which is used as an absolute measure of the tissue's elastic properties. [21, 26].

In compression elastography, the movement of the tissue occurs in the direction of US beam propagation. The most common way to deform the tissue is to apply a slight manual longitudinal compression/decompression using a conventional transducer, or alternatively deformation can be produced by respiratory movements [27]. The absolute value of the deformation along the longitudinal axis is proportional to the intensity of the compression exerted. However, the force exerted by manual compression is unknown to the equipment [27]. The impossibility of defining the intensity of the force exerted allows calculation only of the deformability ratio of the various tissues and not the absolute elasticity. For this reason, elastography by compression provides only qualitative and not quantitative information. While in shear wave elastography, which employs a primary acoustic impulse focused on a region of interest where it generates pressure waves in transverse propagation to deform the tissues. The primary impulse is followed by a few interrogating impulses distributed in the surrounding tissues and designed to calculate the propagation velocity of pressure waves [27]. Since the waves travel faster in stiff tissues than in non-stiff tissues, propagation velocity and attenuation

of the waves are related to the stiffness and viscoelasticity of the tissue [27]. Thus, shear wave elastography is a quantitative imaging technique that provides quantitative measures of tissue stiffness.

Although current approaches of elastography vary considerably, the essence of elastography can be summarized as the following three aspects: first, exert a stimuli on the tissue using mechanical sources, such as quasi-static, harmonic or transient; next, measure the internal tissue displacements using an ultrasound, magnetic resonance or optical displacement estimation method; finally, infer the mechanical properties from the measured mechanical response using either a simplified or continuum mechanical model [20]. If compression or vibration is applied to the tissue, the embedded tumor deforms less than its surrounding normal tissue due to its high stiffness characteristics. Given that fact, elastography records the distribution of tissue elasticity [21].

By displaying the conventional B-mode (2D mode) sonographic image and the elastography side by-side, the relative dimensions of the lesions in both image displays was directly compared [21]. Either length or area of the tumor in the greatest dimension can be utilized to measure the magnitude of the tumor. A study to explore the clinical value of real-time ultrasound elastography in differentiating malignant from benign breast tumors and to determine an optimal cutoff for the traced area ratio by receiver operator characteristic (ROC) analysis for differential diagnosis between malignant and benign breast masses [28]. A feasibility study on 58 *ex vivo* samples from patients undergoing mastectomy or wide local excision was presented in [16]. The objective of their study was to evaluate the potential of optical coherence micro-elastography (OCME) for imaging breast microarchitecture. To achieve this, they used an OCME system developed in their laboratory to image freshly excised benign and malignant

human breast tissue. They demonstrated the performance of OCME to visualize tissue microarchitecture in benign and malignant human breast tissues.

While in most approaches of model-based elastography, the mechanical behavior of soft tissues is modeled using the theory of linear elasticity, Hooke's law, which is an appropriate model for linear elastic materials. A study to investigate the potential value of magnetic resonance elastography (MRE) to improve the differentiation between benign and malignant tumors was presented in [15]. They concluded that a good separation exists between benign and malignant tumors in elasticity, corresponding with specific signal intensity and morphologic data. A study to assess the feasibility of using non-invasive MRE for determining the stage of live fibrosis was presented in [29]. Their results showed that the mean hepatic shear elasticity increased with increasing stage of fibrosis. Most recently, a study to evaluate the diagnostic value of MRE to distinguishing benign and malignant breast tumors was presented in [30]. Their results showed that the combination of MRE and MRI improved the accuracy of breast tumor detection. Furthermore, they confirmed that phase angle has a significant role in predicting tumor malignancy [30]. MRE might provide additional information to improve differentiation of malignant and benign breast lesions but further developments and clinical studies are necessary.

It is well known that most materials, including soft tissues, deviate from Hooke's law in various ways. For example, soft tissues that exhibit both fluid-like and elastic (i.e. viscoelastic) mechanical behavior which is deviated from Hooke's law [31]. For a viscoelastic material such as breast tissue, the relationship between stress and strain varies with time. In general, there are three unique mechanical behaviors exhibited in viscoelastic materials [20]: first, strain increases with time when stress is sustained over a period of time, this phenomenon is known as viscoelastic creep; second, stress decreases with time when strain is held constant, a phenomenon

known as viscoelastic relaxation; third, during cyclic loading, mechanical energy is dissipated in the form of heat, this phenomenon is known as hysteresis. Several promising model-based elastography approaches have been proposed for reconstructing viscoelasticity [20]. A quasi-static method (step-and-hold and low-frequency harmonic stimuli) based on ultrasound was applied to gelatin hydrogel during creep and stress relaxation experiments in confined and unconfined geometries for characterizing the viscoelastic properties [32, 33]. A transient elastography method based on plane shear waves was used to measure the viscoelastic properties of soft tissues [34]. A viscoelastic approach based on a novel 2-D sonoelastographic technique for estimating local shear velocities from propagating shear wave interference patterns (termed crawling waves) was presented in [35]. A preliminary patient study was presented to determine whether viscoelastic features improved benign and malignant differentiation for non-palpable breast tumors discovered on mammographic scanners [2]. Their results demonstrated that the retardation time provided statistically significant contrast [2]. In addition, soft tissues display nonlinear mechanical behavior because of the geometric nonlinearity or material nonlinearity [36].

However, a challenge still exists in the calculation of tumor stiffness, and the instrument of elastography is also expensive and a dedicated operator is always required [7]. It is important to emphasize that Elastography only indicates the relative stiffness of breast tumor within its surrounding normal tissue. Therefore, tumors will exhibit varying shades of gray in fatty breast tissue as opposed to dense breast tissue [21]. This limits the ability to utilize Elastography in a mass screening protocol.

1.1.2 Mechanical Imaging

Mechanical Imaging (MI), which is also called “tactile imaging” or “stress imaging”, is a

method of medical diagnostics that capable of 3D visualization of the internal tissue structures [37]. MI differs from conventional Ultrasonic Elastography, Shear Wave Elastography, and Magnetic Resonance Elastography in that it evaluates soft tissue mechanical structure using stress data rather than dynamic or static strain data. MI is a branch of Elastography, closely mimicking manual palpation because the MI probe with a force sensor array mounted on its tip acts as human fingertips during clinical examination.

The MI measurement probe with a pressure sensor array mounted on its tip acts similar to human fingers by compressing the breast tissue and measuring the resulting pressure distribution on the surface. Upon compression, a tumor produces a change in the surface stress on the examined breast tissue site, which can then be detected by pressure sensor, similar to the sense of touch. MI is intrinsically a 3D imaging modality because the surface stress patterns obtained at different levels of tissue compression are used for the 3D image reconstruction of the examined tissue in terms of its elasticity [13].

Mechanical imaging is a promising field in biomedical engineering, numerous methods and devices have been developed for implementing MI technology in various medical applications during the last decade [31, 38-43]. Several mechanical testing methods have been developed, such as indentation, aspiration, shear strain, and compressive testing for measuring the mechanical responses of soft tissues [44-46]. Among them, indentation is a commonly used mechanical testing method for soft tissues due to its relative simplicity in application and popularity among researchers [46]. Currently, testing equipment dedicated for indentation, such as standard micro/nano-indenters and customized indenters, are widely available [46]. There are mainly two different types of indentation methods: dynamic and quasi-static (e.g., creep, stress relaxation) tests [47]. For the dynamic tests, the system input is a pre-defined force/stress

function exerted on a tissue, such as sinusoid, and the output is the displacement/strain response of the tissue. The amplitude of the displacement/strain response and phase lag between the displacement/strain and force/stress can be measured over a range of frequencies [48, 49]. In creep/stress relaxation tests, with the force or displacement as the input parameter, the recorded data on a tissue are the force-displacement relations from multiple data points, which eliminate measurement errors from uncertainty in contact point between an indenter and a tissue.

For many of the applications, where tissue abnormalities are located within a few centimeters under the accessible tissue surface, the sensitivity and specificity of MI may be comparable to those of sophisticated MRE and USE devices [20]. The diagnostic accuracy, procedure cost and cost-effectiveness of currently available technique for breast screening and diagnosis including mammography, ultrasound, magnetic resonance imaging and mechanical imaging was reviewed, and mechanical imaging was found to have the potential to provide the best cost-effective solution [50]. The Young's modulus of normal and diseased human livers in an *in vivo* condition was measured using indentation test, and a diseased liver was found to be stiffer than a normal liver [38]. A torsional resonator device (TRD) was developed to estimate the complex shear modulus of the liver against shear strain [42]. A motorized endoscopic grasper (MEG) was developed to measure the mechanical behavior of porcine livers according to the compressive stress [43]. Using SureTouch™ system, a breast mechanical imager was developed for breast tumor characterization and differentiation between benign and malignant tumors [13]. They have developed an examination procedure and algorithms to provide assessment of breast tumor features such as hardness related parameters, mobility, and shape. Clinical results for 179 cases, collected at four different clinical sites, have demonstrated that the breast mechanical imager provides a reliable image formation of breast tissue abnormalities and calculation of

lesion features. A piezoelectric finger (PEF) was developed to be used as a prescreening tool in women who do not receive the maximum benefit from mammographic surveillance [19]. The PEF was a radiation-free, portable, and low-cost breast tumor detector does not require skilled interpretation. Although the PEF was quite good at identifying the location of the lesion within the breast, the size prediction *in vivo* was not reliable [19]. A compact tactile imaging (TI) system was developed to guide the clinician or the self-user for noninvasive detection of breast tumors. Their system measured the force distribution based on the difference in stiffness between a palpated object and an abnormality within [17]. Also, the performance of their device was better in detecting shallow and deep inclusions than intermediate ones. It detected the deep inclusions better than the intermediate ones because deep inclusions were constrained by the lower boundary (bottom surface) of the silicone sample when the sample was compressed by the device [17]. A tactile sensation imaging system (TSIS) was developed to capture images of the embedded lesions using total internal reflection principle [7]. They investigated a tissue inclusion characterization method for the application of early breast tumor identification [7]. A Tactile Imaging (TI) system using simple algorithms for extracting breast lump features from measurements of contact pressure was developed. They have developed models that predict these pressure distributions from geometric and material properties. Their result demonstrated that tactile imaging has the potential to improve the accuracy of clinical breast examination [18].

MI is simple, fast, inexpensive and safe [20]. The data obtained by MI allows the calculation of mechanical properties of tissues, such as Young's modulus, elasticity contrast, nonlinearity, heterogeneity index, tumor size, shape and mobility, which could be altered by the cancer progression [51]. MI technology is potentially applicable to any field of medical diagnostics and treatment monitoring where manual palpation is used [52]. A compact hand-held

MI probe may help surgeon to more accurately and objectively map the boundaries of affected tissue. However, MI cannot be used for imaging tissue structures located well below the limit of manual palpability [20]. In addition, the challenges in expanding the field of applications of MI are mainly in adapting the geometry of the probe with the force sensor array to new anatomical sites and tissue types and creating data processing algorithms and MI probe manipulation techniques for new users and applications.

1.2 Motivation

Based on the rationale that mechanical properties of a tumor can serve as biomarkers of its biological features, noninvasive mechanical alternatives to the anatomical imaging techniques and biopsies have been aggressively pursued [2, 13, 15, 17-19]. As discussed in the prior sections, these mechanical alternatives fall into two categories: elastography and mechanical imaging. Currently, elastography is generally limited to the mechanical characterization of tumors that have already been identified through an independent screening method. Elastography always requires expensive and complicated equipment, highly intensive and computationally costly motion tracking algorithms, and complex algorithms for extracting mechanical properties from the measured mechanical responses [7]. Owing to the simplicity for its implementation, mechanical imaging offers a low-cost, simple-use alternative to elastography [12, 53]. Some studies aimed to develop tactile sensor arrays as a low-cost, simple-use screening tool solely for tumor detection [17, 18], and other studies examined tactile sensor arrays for both tumor detection and differentiation [7, 13, 19]. However, most studies on mechanical imaging utilized only Young's modulus for tumor detection and differentiation. A cutoff value for identifying the existence of a tumor was arbitrarily chosen, in the sense that no strict criterion was established for its justification. By creating complex algorithms for processing the measured data using a

commercially available sensor array, two mechanical parameters: hardness and nonlinearity, were measured and used for tumor differentiation [13, 51]. While clinical studies on the efficacy of this sensor array for tumor differentiation revealed contradictory results [13, 51, 54].

The majority of the studies on elastography and mechanical imaging have treated healthy tissue embedded with a tumor as a linear elastic medium for more straightforward and tractable interpretation of elasticity results. In reality, tumors and healthy tissues are viscoelastic and nonlinear, and then exhibit a much more complicated dynamic behavior than an idealized linear elastic body. Thus, elasticity alone does not ensure the diagnostic accuracy of tumor characterization. In fact, breast tissues demonstrate highly nonlinear stress-strain behavior, and their Young's modulus almost doubles when strain increases from 5% to 20% [55]. Moreover, tumors tend to be more nonlinear than healthy tissues. Thus, nonlinearity difference between a healthy tissue and a tumor becomes even much more pronounced with an increase in strain and has been explored for improved diagnostic accuracy [56]. However, overlap has been observed in nonlinearity between tumor tissue and healthy tissue.

To date, elasticity and viscosity are the two most studied mechanical properties for tumor detection and differentiation. Elasticity may serve well for tumor detection, but fails to differentiate malignant tumors from benign tumors, due to overlap in elasticity between them [13, 57, 58]. In contrast, viscosity has been found to serve as a better indicator for tumor differentiation, with a clear margin between malignant tumors and benign tumors [2, 13, 59-62]. For instance, retardation time obtained from creep testing shows a significant difference between benign breast tumors and malignant breast tumors [2]. By performing creep testing on human breast tissues *in vivo* and applying a first-order Kelvin-Voigt model to fit the measured data, a contrast parameter associated with retardation time was identified as a new biomarker for tumor

differentiation [62]. Meanwhile, healthy breast tissues were differentiated from tumorous tissues *in vivo* by utilizing a viscosity-related coefficient obtained by fitting continuous compression data with a five-element Maxwell-Wiechert model [61]. A viscosity parameter, derived by fitting stress relaxation data using a Kelvin-Voigt fractional derivative (KVFD) model, reveals a pronounced difference between cancerous prostate tissues and healthy prostate tissues [60].

The viscosity of a tissue needs to be evaluated from its time-dependent behavior. Two common testing methods for measuring the time-dependent behavior of a tissue are stress relaxation and creep testing, but these experimental data are prone to misalignment errors (i.e., uncertainty in contact point) and tissue surface unevenness. The tissue viscosity is then quantified by fitting the experimental data with a chosen model. A Maxwell model and a Kelvin-Voigt model are commonly used to fit the data from stress relaxation and creep testing for quantifying the tissue viscosity as relaxation time and retardation time, respectively [61, 63, 64]. However, curve-fitting based on these two models typically suffers from low quality of fitness, and the derived model parameters for tissue viscosity have been found to be sensitive to the duration of the relaxation data used in the model fitting [63]. Therefore, new material models, such as Kelvin-Voigt fractional derivative (KVFD) model [64] and the above-mentioned Maxwell-Wiechart model [61], have been proposed for improving the quality of fitness and alleviating the sensitivity of the extracted model parameters to the experimental data collected on different types of tissues using different testing methods.

Stepwise compression-relaxation testing entails a cycle of multiple increasing applied strains as step inputs and followed by a period of stress relaxation at each applied strain, and thus is robust to misalignment errors and tissue surface unevenness, as compared with one step stress relaxation and creep testing [65]. In recent years, the stepwise compression-relaxation testing

method has gained great popularity in measuring a variety of native soft tissues and biomaterials, including cartilage tissues, vascular tissue constructs, breast tumor tissues and collagen gels [66-70]. The measured data are instant stress and relaxed stress at the beginning and end of each applied strain, respectively, and are further processed to obtain instant/relaxed elasticity by extracting the slope of instant/relaxed stress versus applied strain. The tissue viscosity is quantified as the slope of the difference between instant stress and relaxed stress versus applied strain [69, 70], which is essentially the slope of stress drop ($\Delta\sigma$) versus applied strain (ε), $m=\Delta\sigma/\varepsilon$. The slope of single-layer vascular tissue constructs was found to be significantly lower than its double-layer and triple-layer counterparts and no difference in relaxed elasticity was observed among them [69].

In this dissertation, a stepwise compression-relaxation (SCR) testing method was implemented on a 2D tactile sensor that entails a 3×3 sensing-plate/transducer array built into a single PDMS microstructure for tissue characterization and tumor detection. Built upon a 1D sensor previously developed by our group [71], the 2D tactile sensor features simplicity in design and fabrication, low cost, ease of use and performance robustness. In the preliminary work [72], a 2D tactile sensor is implemented and its feasibility for tissue palpation is validated using a few soft tissues such as PDMS samples, chicken hearts, and mice breast tumor tissues. In this 2D sensor, the sensing-plate array is built into one whole microstructure, and thus interacts with the surface of an object in a continuous manner. Consequently, similar tilt angles are formed at different contact locations of the sensing-plates with an object. This will greatly alleviate errors associated with misalignments in the measured results. The measurement errors associated with performance variation among the sensing-plate/transducer array was tackled and verified with experimental results. Two mouse breast tumor tissues were measured, and their stiffness

distribution was obtained for tumor detection. The ultimate goal of this study [72] is to offer the SCR testing method as a robust diagnostic method for tissue characterization and tumor detection.

In the SCR testing method, the 2D sensor features simple fabrication, easy use, and low cost characteristics; misalignment issue is tackled by the continuous manner of the sensor sensing-structure; both elasticity and viscoelasticity of soft tissues are measured simultaneously; effects of testing parameters on the measured results are investigated; mechanical properties of tumor tissue are explored to determine tumor existence, tumor location, tumor size and tumor shape; and the correlation of the measured tissue stress drop and applied strain are quantitatively analyzed as slope of stress drop and strain, m, and coefficient of determination, R^2, to distinguish tissue sites among tumor center, edge, outside region, and normal tissue.

1.3 Objectives

This dissertation aims to develop a stepwise compression-relaxation (SCR) testing method based on a two-dimensional (2D) tactile sensor to measure the mechanical properties of soft tissues. In particular, this work investigates the potential mechanical biomarkers based on the measured results for differentiation between tumor tissue and normal tissue. To implement the SCR testing method, a 2D sensor was designed, fabricated and characterized. Built upon the 2D sensor, a pre-defined compression pattern was used to measure several groups of the soft samples, including PDMS samples and silicone rubbers, porcine and bovine tissues, and mouse breast and pancreatic tumor tissues. Firstly, effects of the testing parameters (incremental depth, hold-on time and ramp speed, etc.) of the SCR testing method on the measured results of the PDMS/silicone rubbers were evaluated. Next, the SCR testing method was used to measure the porcine/bovine tissues and mouse breast/pancreatic tumor tissues to validate its feasibility for

mechanical characterization of soft tissues. The measured mechanical properties were used for tumor detections, including determination of the tumor existence, tumor location, tumor size and tumor shape within a tumor tissue; and differentiation among tissue sites of tumor center, tumor edge, tumor outside region, and normal tissue.

The specific aims includes: 1) design and develop a tactile sensor with a 2D sensing-plates/transducer array for measuring the mechanical properties of soft tissues; 2) design and develop a mechanical testing method based on the 2D tactile sensor for characterization of the elasticity and viscoelasticity of soft tissues; validate the feasibility of the testing method and investigate the effects of testing parameters on the measured result; and 3) determine the mechanical biomarker from the measured mechanical properties for detection of tumor existence, location, size, and shape; and differentiation among tissue sites of tumor center, edge, outside region, and normal tissues with statistically significant difference.

1.4 Dissertation Organization

The previous sections have provided a literature review of the techniques used for tissue characterization and tumor detection, and the dissertation motivation and objectives.

Chapter Two presents the 2D tactile sensor used as a basis for implementing the SCR testing method. A brief introduction of the sensor working principle, sensor fabrication and sensor performance characterization were presented. Furthermore, technical issues associated with the sensor fabrication and the misalignment issues encountered in the sensor-tissue interaction were also discussed.

Next, the relevant analytical model of the SCR testing method for extracting the mechanical properties (elasticity and viscoelasticity) of soft tissues was described in detailed in Chapter Three.

In Chapter Four, first, the measured data of the PDMS and silicone rubbers were used to investigate the effects of the testing parameters (incremental depth, hold time, and ramp speed) on the measured mechanical properties. Next, porcine/bovine tissues and PDMS sample with embedded inclusions were measured to validate the feasibility of the SCR testing method for measuring the mechanical properties of soft tissues. Details about the sample preparation, experimental setup, experimental procedures, and statistical analysis, results, and discussion were presented.

Chapter Five presents the tumor detection based on the elasticity extracted from the measured results. Five breast tumor (BT) tissues were measured *ex vivo*, and two pancreatic tumor (PT) tissues were measured *in vivo*. Details about the sample preparation, experimental setup, experimental procedures, results and discussion were presented.

Chapter Six presents the tumor detection based on the correlation between stress drop and applied strain. First, effects of the testing parameters on the measured correlations between stress drop and applied strain were investigated. Next, statistical analysis was conducted to compare the measured results among the tissue sites of the tumor center, edge, outside region, and the normal tissues to investigate its feasibility for distinguishing tumor tissue and normal tissue.

Lastly, Chapter Seven presents a summary of the main findings of this dissertation, and several directions for future research.

CHAPTER 2

A TWO-DIMENSIONAL TACTILE SENSOR

This chapter presents a two-dimensional (2D) tactile sensor for measuring the mechanical properties of soft tissues and tumor detection. The 2D sensor consists of a polydimethylsiloxane (PDMS) microstructure embedded with a 3×3 sensing-plate/transducer array. Distributed deflections acting on the sensing-plates were registered as resistance changes of the transducers. Details about the sensor design, fabrication process, and characterization have been reported in the previous work [71, 73]. A brief introduction of the 2D sensor was presented in this chapter for completeness, which included: the sensor working principle, sensor fabrication, sensor characterization, and the associated technique issues occurred in the fabrication process and misalignment issues occurred at the sensor-tissue interaction.

2.1 Sensor Design and Operation

The core of the sensor is one whole polydimethylsiloxane (PDMS) microstructure embedded with a 3×3 sensing-plate/transducer array (Figure 2.1). The transducer array is implemented through an electrolyte-filled serpentine-shape microchannel and a set of electrode pairs aligned with the sensing-plate array. Electrolyte underneath a sensing-plate serves as a resistive transducer, whose resistance is a function of the bottom deflection of the sensing-plate and is routed out by the electrode pair [71, 74]. The serpentine-shape microchannel contains three sub-microchannels in parallel for realizing three rows of the transducer array and meanwhile reducing the number of reservoirs. Three electrode pairs are aligned along each sub-microchannel for implementing three transducers in a row. The distributed deflection acting on top of the sensing-plate array translates to geometrical changes of the transducer array and registers as resistance changes. Two reservoirs at the ends of the whole microchannel are utilized

for injecting electrolyte into the microchannel and further providing a conduit for electrolyte flowing in and out during the sensor operation. Figure 2.1(c) depicts the equivalent electrical circuit of the transducer array and its signal routing. To acquire the resistance change of a transducer, a high-frequency AC voltage signal is applied to one electrode of a transducer, while the other electrode of a transducer outputs an AC current signal [71, 73]. To avoid electrical interference among the transducers, a common input is applied to all the transducers, and the output of each transducer is connected to the same electrical circuit and is recorded as a DC voltage output [71, 73].

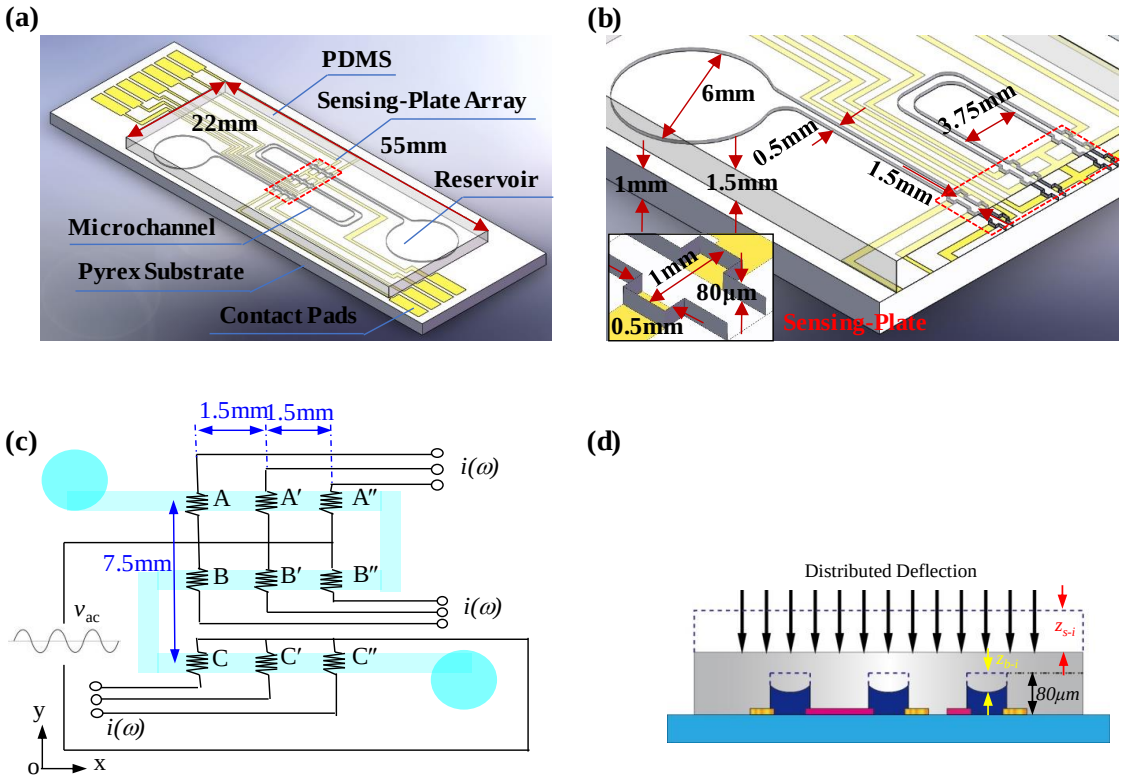

Figure 2.1 A 2D tactile sensor for tissue palpation (a) whole configuration, (b) key dimensions of the PDMS microstructure embedded with a 3×3 sensing-plate/transducer array, (c) equivalent circuit model of the 3×3 resistive transducer array with one common input to all the transducers, and (d) working principle: side-view (drawn not to scale for clear illustration).

The key design parameters and their values of the sensor are listed in Table 2.1. The spatial resolution of the transducer array is 1.5mm along the x-axis and 3.75mm along the y-axis. The effective sensing region of the sensor is 3mm×7.5mm, defined by the distances between the sensing-plate centers at the array sides. While the microstructure is made of 10:1 PDMS material, the electrolyte used is 1-ethyl-3-methylimidazolium dicyanamide (EMIDCA).

Table 2.1 Key parameters and their values of the 2D distributed sensor.

Design parameter	Value	Symbol
Microstructure thickness	1mm (sensor #1) 1.2mm (sensor #2)	h_m
Transducer height	80μm	h_e
x-axis spatial resolution	1.5mm	d_x
y-axis spatial resolution	3.75mm	d_y
Dimension of the effective sensing region	3mm×3.75mm	$2d_x \times 2d_y$
Diameter of the reservoirs	5mm	D_r
In-plane dimension of a rectangular sensing-plate	0.5mm×1mm	$l_p \times w_p$

2.2 Sensor Fabrication

A standard PDMS-based fabrication process for microfluidic devices was employed to fabricate this sensor and the details about the fabrication process can be found in the literature [71]. After the sensor was fabricated, electrolyte was injected into the microchannel using a syringe through a reservoir. PDMS was used to seal the reservoirs of the sensor so that the sensor can be flipped over to palpate a soft tissue. Figure 2.2 shows the pictures of the fabricated sensor. Two sensors of identical in-plane dimensions were fabricated, with Sensor#1 having a thicker PDMS microstructure than Sensor#2. Two designs of the sensor: circular sensing-plates (Sensor#1) and rectangular sensing-plates (Sensor#2), respectively, are built into the microstructure and aligned right on top of each transducer, as shown in Figures 2.2 (c) and 2.2(d). Thus, the transducer array coincides with the sensing-plate array in the microstructure. These

sensing plates are expected to not only achieve high sensitivity, but also alleviate the structural crosstalk and the transducer crosstalk.

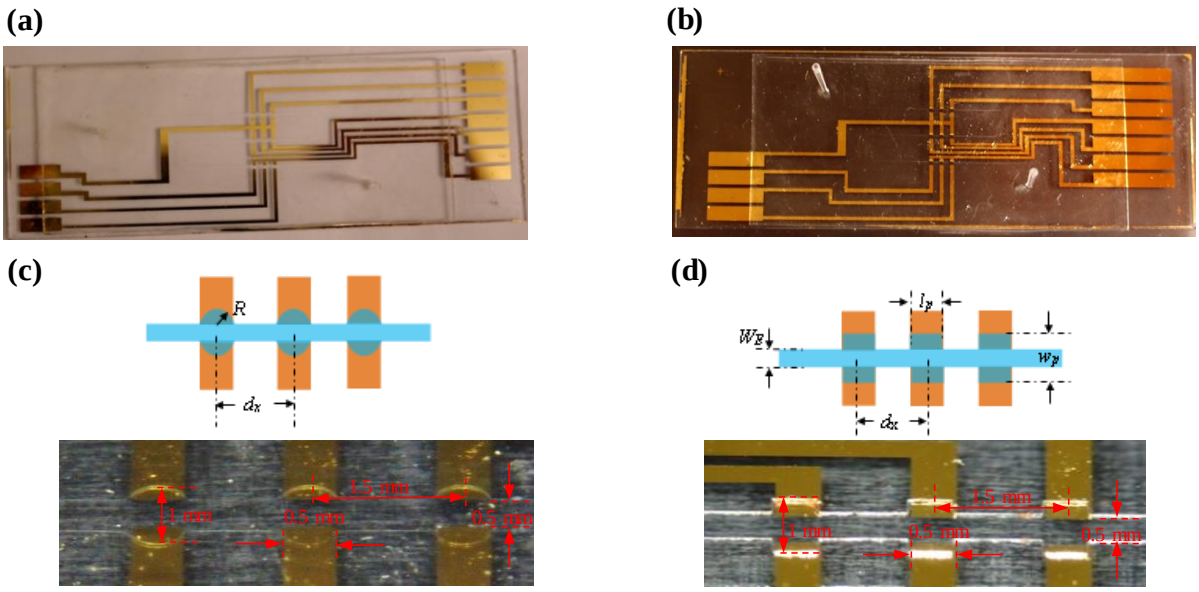

Figure 2.2 Pictures of the fabricated sensor (a) Sensor#1, (b) Sensor#2, and one row of sensing plates and transducers and the key dimensions of (c) Sensor#1, and (d) Sensor#2, respectively.

2.3 Fabrication Variation, Misalignment Issue and Correction Mechanism

Arising from fabrication variation, the transducer height, as the smallest design parameter, may vary among the transducer array, and thus cause performance variation among them. In contrast, the rest design parameters are much larger, and thus the effect of their variation on the sensor performance is negligible. Hence, only the transducer height is considered to be different among the sensing-plate/transducer array in the following analysis.

Prior to aligning a probe or a tissue on the sensor, the height of the *i-th* transducer is defined as its original height, $h_{e\text{-}i}$, and the resistance of the *i-th* transducer is defined as its original resistance:

$$R_{0-i} = \frac{\rho \cdot w_p}{l_p \cdot h_{e-i}} \tag{2.1}$$

where ρ is the electrical conductivity of the electrolyte used, and w_p and l_p are the in-plane dimension of a sensing plate. Based on Equation 2.1, the original transducer height of a transducer can be obtained by measuring its original resistance. Table 2.2 summarizes the measured original resistances of the transducer array and their original heights of the two sensors. The original transducer height varies among the transducer array in each sensor.

The deflections at the top, $z_{s\text{-}i}$, and the bottom, $z_{b\text{-}i}$, of the *i-th* sensing-plate are different (Figure 2.3(a)). A finite element model was created in COMSOL to simulate the deflections at the top and the bottom of a sensing-plate (Figure 2.3(b)). The model includes the PDMS microstructure and a cylinder probe on its top. As the input, the displacement of the probe coincides with the top deflection of the microstructure but leads to a smaller bottom deflection of the microstructure. The key parameters used in the model are summarized in Table 2.3.

With either deflection as reference, the *i-th* sensing-plate can be treated as a spring with its top stiffness, $k_{s\text{-}i}$, and the bottom stiffness, $k_{b\text{-}i}$:

$$F_i = k_{s-i} \cdot z_{s-i} = k_{b-i} \cdot z_{b-i} \tag{2.2}$$

where F_i denotes the force accompanying the deflection. The thickness of the *i-th* sensing-plate, $h_{s\text{-}i}$, is the subtraction of the original transducer height, $h_{e\text{-}i}$, from the microstructure height, h_m:

$$h_{s-i} = h_m - h_{e-i} \tag{2.3}$$

According to the thin-plate theory [75], the stiffness of the sensing-plate is a function of its thickness:

$$k_{s-i}, k_{b-i} \propto \frac{E \cdot (h_m - h_{e-i})^3}{(1-\upsilon^2)} \tag{2.4}$$

where E and υ are the elasticity and the Poisson's ratio of PDMS, respectively.

Later on, the top stiffness of the sensing-plate is utilized to obtain the stiffness of a tissue, and thus we analyze how the top stiffness, $k_{s\text{-}i}$, of the sensing-plate varies with its thickness. The stiffness of a sensing-plate with the designed thickness, h_e, are treated as the nominal stiffness, k_s.

This nominal sensing-plate experiences a nominal load, F_s, and a nominal deflection, z_s. According to Equation 2.4, the stiffness of the *i-th* sensing-plate is related to the nominal stiffness by:

$$\frac{k_{s-i}}{k_s} \propto \frac{(h_m - h_{e-i})^3}{(h_m - h_e)^3} = 1 - \frac{3}{h_m}(h_{e-i} - h_e) \tag{2.5}$$

Table 2.2 Measured original resistances and original heights of the transducer array in the two sensors.

	Sensor#1		Sensor#2	
	$R_{0\text{-}i}$ (Ω)	$h_{e\text{-}i}$ (μm)	$R_{0\text{-}i}$ (Ω)	$h_{e\text{-}i}$ (μm)
A	3919	102	4051	99
A'	3857	104	4304	93
A"	3729	107	4292	93
B	4603	87	4768	84
B'	4564	88	4920	81
B"	4835	83	5330	75
C	5446	73	3184	126
C'	5596	71	2973	135
C"	5492	73	2903	138
k_s (N/m)	0.43		0.67	
k_b/k_s	11		60	

where $h_m >> h_e$ is utilized. By treating the average transducer height of each sensor in Table 2.2 as the nominal design, the fabrication variation in transducer height causes a stiffness variation of <6% and <9% among the sensing-plates for Sensor #1 and Sensor #2, respectively.

To characterize the performance of the sensor, a rigid cylinder probe of 0.8mm-in-radius and 11mm-length is aligned on top of a sensing-plate row and deflects a row at a time. The transducer height may change due to misalignment. The height of the *i-th* transducer after alignment is defined as the initial transducer height, $h_{e\text{-}i}$. Consequently, the initial resistance, $R'_{0\text{-}i}$, of the *i-th* transducer after alignment becomes:

$$R'_{0-i} = \frac{\rho \cdot w_p}{l_p \cdot h'_{e-i}} \tag{2.6}$$

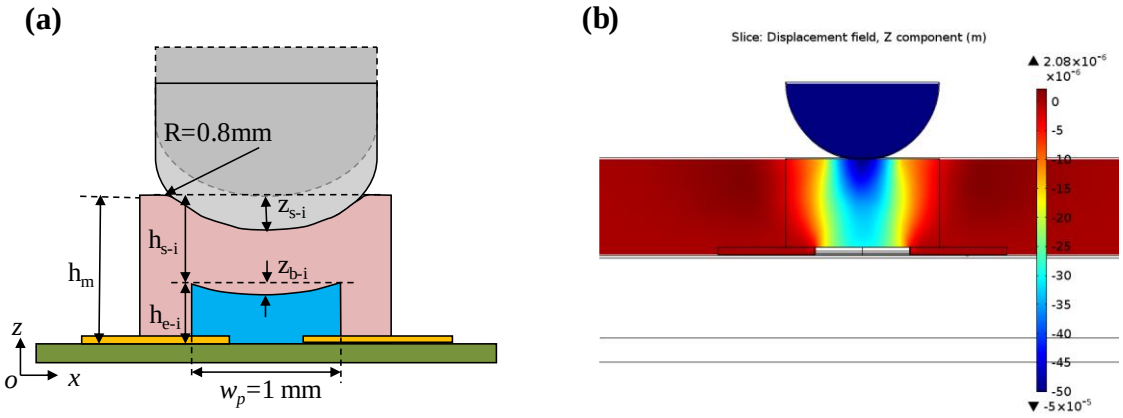

Figure 2.3 Deflection acting on the top of a sensing-plate from a cylinder probe translates to a geometrical change in the transducer underneath (a) schematic (b) simulation.

Table 2.3 Key parameters and their values of the finite element model.

Design parameter	Value	Symbol
Young' modulus of the PDMS	700 KPa	E_{PDMS}
Poisson' ratio of the PDMS	0.45	υ_{PDMS}
Density of the PDMS	1000 kg/m^3	ρ_{PDMS}
Young' modulus of the probe	100 GPa	E_{probe}
Poisson' ratio of the probe	0.30	υ_{probe}
Density of the probe	7850 kg/m^3	ρ_{probe}

Prior to moving the probe to deflect a sensing-plate row, this initial resistance was measured. The resistances of the corresponding transducer row were recorded as a function of the probe displacement, which coincided with the top deflection of the sensing-plate row. Calculated relative to the initial resistance (initial transducer height), the resistance change of the *i-th* transducer is a function of the bottom deflection of the *i-th* sensing-plate:

$$\Delta R_i = R_i - R'_{0-i} = \frac{\rho \cdot w_p}{l_p \cdot h'_{e-i}} \cdot \left[\left(1 - \frac{z_{b-i}}{h'_{e-i}} \right)^{-1} - 1 \right] = \frac{\rho \cdot w_p}{l_p \cdot (h'_{e-i})^2} \cdot z_{b-i} = \frac{(R'_{0-i})^2 \cdot l_p}{\rho \cdot w_p} \cdot z_{b-i} \tag{2.7}$$

where the relation of $z_{b-i} << h_{e-i}$ is utilized. Therefore, the bottom deflection of the *i-th* sensing-plate can be obtained from the resistance change and the initial resistance of the *i-th* transducer:

$$z_{b-i} = \frac{\Delta R_i}{(R'_{0-i})^2} \cdot \frac{\rho \cdot w_p}{l_p} \tag{2.8}$$

The above equation alleviates the out-of-plane misalignment error shown in Figure 2.7(a) from the measured results.

2.4 Sensor Characterization

The same experimental setup for measuring the performance of the 1D sensor [76] is utilized to characterize the performance of the 2D tactile sensor. The details about this setup can be found in the literature. For completeness, a brief description of the experimental setup was given here. As depicted in Figure 2.4, the whole experimental setup is built on an optical table. The PCB mounted with a fabricated sensor is fixed on a 5-axis manipulator. A function generator is connected to the common input of the transducers. The outputs of the transducers are connected to their own dedicated electronics on PCBs for converting their AC current outputs to their corresponding DC voltage signals, V_{DC}, which feeds into a DAQ card (NI PXI-6133) and further recorded by a custom LabVIEW program.

A cylinder probe was used to generate varying deflection distributions on the microstructure of the 2D sensor. Since the probe was rigid relative to the sensor, the probe displacement simply represents the deflection of the microstructure. The probe was mounted on a micropositioner for static performance characterization. Meanwhile, a load cell (ATI, nano17) was incorporated into the setup to capture the overall force experienced by the 2D sensor, in response to a distributed deflection input. Having a length of 15mm and a radius of 0.79mm, the cylinder probe was aligned with a row of the sensing-plate array at a time in order to exert deflection on the three rows individually.

Prior to testing the 2D sensor, a probe was manually aligned with the sensor through visual examination. The 5-axis manipulator was then manually adjusted to better align the axis of

the cylinder probe. Different from our previous work, the signals of the sensor are not monitored during alignment in this work. The micropositioner was utilized to exert a pre-defined static deflection pattern on the sensor through a probe. The position of the probe after being aligned is treated as its original position. The probe is brought down to a pre-defined displacement at a time at a speed of 1mm/s and stays at this displacement for 5s. Then, the probe is brought back to its original position at the same speed and stays there for 5s. This cycle repeats with a displacement increment of 15μm consecutively until reaching the final displacement of 600μm. The output signals of the sensor and the readout of the load cell are recorded at a sampling rate of 500Hz in response to the static inputs.

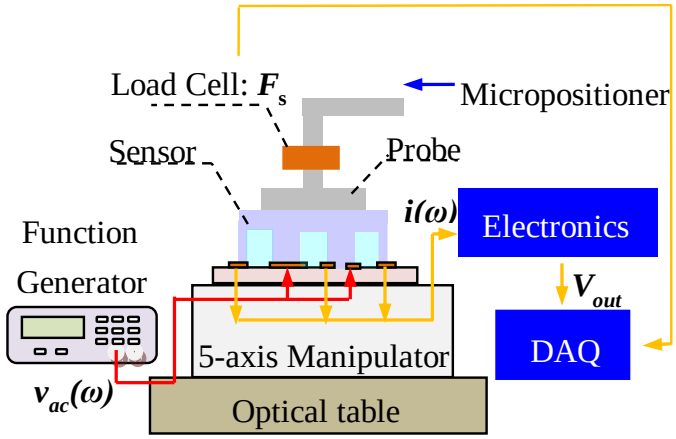

Figure 2.4 Schematic of the experimental setup for characterizing static performance of the 2D tactile sensor.

Figure 2.5 plots the measured resistance changes of the transducer array and the overall force as a function of the top deflection of a sensing-plate row for Sensor#1. Note that there is a slight resistance drop in the transducers free of deflection, which is believed to result from the electrolyte in the deflected transducers flowing into them. It can be seen that the same top deflection acting on the transducers gives rise to a large variation in the resistance change (from 1310Ω in A to 4437Ω in C at z_{in}=400μm), owing to the transducer height variation from

fabrication variation and misalignment. According to Equation 2.7, the resistance change is proportional to the squared initial resistance, and thus is highly sensitive to the initial transducer height. Based on Equation 2.8, Figure 2.6 plots the bottom deflection of the sensing-plates as a function of their top deflection. It can be seen that the bottom deflection of the sensor (varying from 24μm in B to 45μm in B at z_{in}=400μm) is much less immune to the transducer height variation than the resistance change. The bottom deflection variation is believed to result from a combination of the in-plane misalignment shown in Figure 2.7(b), experimental noise, as well as the small stiffness variation among the sensing-plates. Note that this in-plane misalignment is not encountered when the sensor palpates a soft tissue.

According to the relation of the force versus the top deflection of a sensing-plate row, the averaged stiffness of a sensing-plate is calculated and included in Table 2.2. The top deflection, z_s, of a sensing-plate will be used to obtain the tissue mechanical properties in the following chapter. Therefore, the averaged relation of the bottom deflection versus the top deflection of the

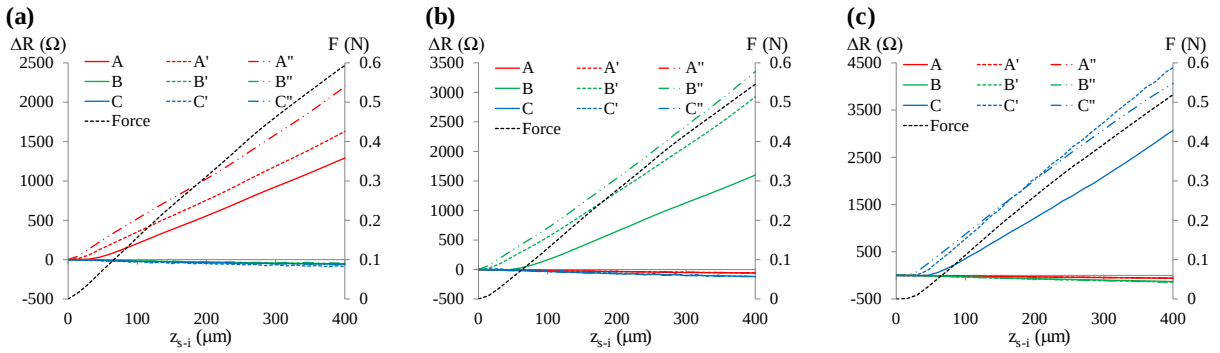

Figure 2.5 Measured resistance changes, Δ*R*, and the overall force, *F*, as a function of the top deflection of the sensor, $z_{s\text{-}i}$, exerted by the cylinder probe located above (a) A, A′and A′′ (b) B, B′ and B′′(c) C, C′ and C′′.

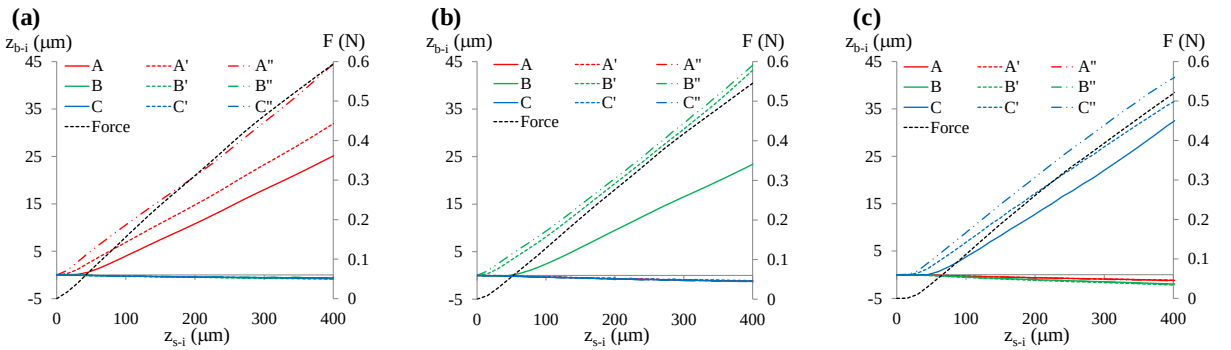

Figure 2.6 Measured deflection at the bottom of the sensing-plates, $z_{b\text{-}i}$ in the sensor from the measured average resistance changes as a function of the deflection at top of the sensor, $z_{s\text{-}i}$, exerted by the cylinder probe located above (a) A, A′and A′′ (b) B, B′ and B′′(c) C, C′ and C′′.

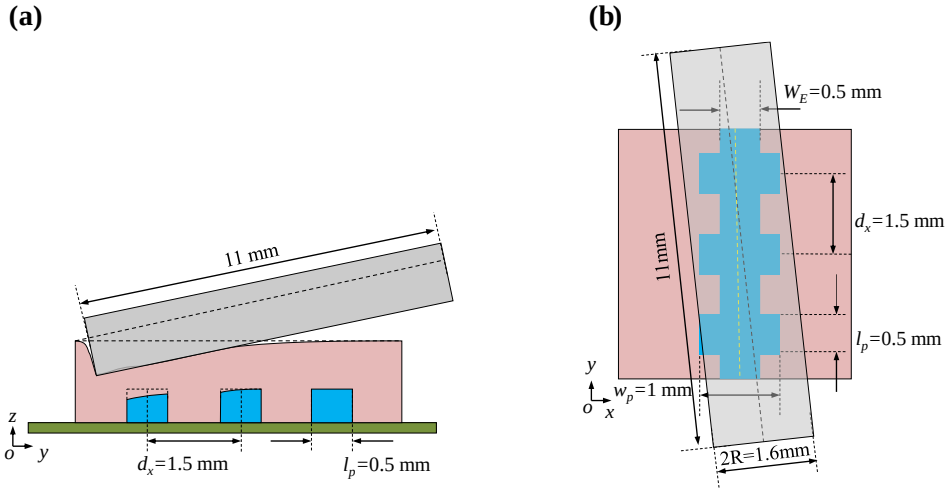

Figure 2.7 Misalignment of a 0.8mm-in-radius and 11mm-long rigid cylinder probe with a sensing-plate row for performance characterization of the sensor (a) out-of-plate misalignment (b) in-plane misalignment (out of proportion for clear illustration).

sensing-plate array for Sensor#1 is extracted from Figure 2.6:

$$k_b \approx 11 \cdot k_s \quad \text{(Sensor \#1)} \tag{2.9}$$

Similarly, the averaged relation for Sensor #2 can also be obtained:

$$k_b \approx 60 \cdot k_s \quad \text{(Sensor \#2)} \tag{2.10}$$

Note that the detailed results on Sensor #2 are omitted, due to their similarity to the results on Sensor #1.

2.5 Technical Issues

2.5.1 Interference Among the Transducers

Because of the inter-connection of electrolyte in the transducer array, electrolyte in the transducers under a probe needs to flow through the rest transducers and into the two reservoirs. Then, a geometrical reduction in a transducer being pressed is accompanied by a geometrical increase in the transducers un-pressed, which is observed in the static performance characterization of the sensor. However, this interference among the transducers is trivial to the static performance of the sensor.

2.5.2 Effects of the Key Design Parameters on the Sensor Performance

By comparing the measured results of the two fabricated sensors, the shapes of sensing-plates do not affect the static performance of the sensor. Although the reservoirs in Sensor #1 are much larger than those in Sensor #2, the measured results shown that the size of the reservoirs does not affect the performance of the sensors. This is reasonable, since the two reservoirs are roughly 10mm away from the transducer array. However, the cross-section dimension of the microchannel plays a critical role in determining the static performance of the sensor. Fabrication variations result in varying microchannel heights among different rows of transducers and thus varying cross-sections of the microchannel. A small cross-section of the microchannel leads to a high initial resistance and thus a large slope of the measured sensor deflection-compression depth relation. This might be attributed to the fact that the cross-section of the sub-microchannel for the third row is very small, and thus electrolyte in this row cannot flow into the reservoir with relative ease to reduce such interference.

2.5.3 Effects of Misalignment Issue

The misalignment between a probe and the sensor has two aspects: on the one hand, it is

impossible to achieve perfect normal contact of a probe with the sensor (non-ideal normal contact); on the other hand, it is difficult to align a probe in contact with the sensor (uncertainty in contact point), without either deforming the sensor or having a gap with the sensor. Certainly, the two aspects are not exclusive of each other, in the sense that non-ideal normal contact will cause varying uncertainties in contact point with different transducers. For instance, the cylinder probe is always tilt toward one transducer in a row and deforms both transducers to different extents. Therefore, the transducers under the probe experience different deflections in reality, upon the same displacement exerted by a probe. Meanwhile, it is impossible to measure the exact deflections experienced by each transducer. It should be emphasized that no extensive efforts are taken in the experiments for achieving better alignment, other than manually aligning a probe with the sensor through visual examination.

Both aspects of misalignment could severely affect the absolute slope amplitudes of the measured z_s-z_{in} relations of the transducers, as evidenced in Figures 2.5 and 2.6. However, the relative slope amplitudes of the measured z_s-z_{in} relations of the transducers may serve as an indicator of the misalignment. For instance, the large slope of the measured z_s-z_{in} relation of one transducer relative to the other transducer in the same row indicates that the cylinder probe is tilt toward the former. Here, it is worth mentioning that using the slope of the measured z_s-z_{in} relation alleviates the errors associated with uncertainty in contact point, as compared with using a single data point on the measured z_s-z_{in} relation. In the static performance, those transducers not in contact with a probe exhibit a negative slope of the measured z_s-z_{in} relation, and thus enhance the information on misalignment. The relative in-phase signal amplitudes of transducers reveal to what extent the contact is or how the probe is tilt toward them. Finally, it is undeniable that fabrication variations give rise to different slopes of the measured z_s-z_{in} relations among the

transducers. However, in most cases, the measured performance variations among the transducers resulting from misalignment errors overpasses the performance variation associated with fabrication variation.

2.6 Conclusion

In this chapter, the design, working principle, performance characterization of the 2D tactile sensor for measuring distributed sensor deflections were presented. Technical issues encountered in sensor fabrication and misalignment issues occurred in the sensor-tissue interaction were also presented. The 2D tactile sensor features a whole polymer microstructure integrated with a 3×3 resistive transducer array underneath. Two designs of the sensor, employing different shapes of sensing-plates and reservoirs of different sizes, were studied to investigate how they affect the static performance of the sensor. While the shape of sensing-plates, whether circular or rectangular, showed no influence on the static performance of the 2D sensor. A cylinder probe was employed to exert varying deflection distributions on the 2D sensor. Both sensor designs were capable of measuring static deflection distribution with good repeatability. Misalignment of a probe on the sensor, namely, non-ideal normal contact and uncertainty in contact point, was identified as the most critical factor that determined how the slope of the measured relation of sensor deflection and compression depth varied among the transducers being pressed. Meanwhile, technical issues encountered in the fabrication variations was also discussed. Consequently, a correction mechanism was developed to compensate the effects of the performance variation among the sensing-plate/transducer array, and misalignment issues arising from non-ideal normal contact on the measured tissue stiffness distribution across a tissue region.

CHAPTER 3

A STEPWISE COMPRESSION-RELAXATION TESTING METHOD

This chapter illustrates the rationale of the stepwise compression-relaxation (SCR) testing method built upon the 2D sensor for measuring the mechanical properties of soft tissues and tumor detection. The rationale of the SCR testing method is illustrated, which includes how to extract instant elasticity and loss tangent from the measured sensor deflection, which is used to quantify tissue elasticity and viscoelasticity, respectively, as well as how to translate the measured sensor deflections into the relation between stress drop and applied strain which was quantitatively analyzed for distinguishing tumor tissue from normal tissue. Furthermore, effects of the tissue parameters (e.g., tissue thickness, in-plane dimension, and elasticity) on the measured tissue elasticity are studied by using finite element analysis method.

3.1 Rationale

Figure 3.1 depicts the rationale of characterizing the mechanical properties of soft tissues using the SCR testing method. The sensing-plates were designed to have the same in-plane dimension of 0.5mm×1mm. The 3×3 sensing-plates and transducers array were designed to have identical mechanical and electrical performance parameters, respectively [77]. Then, the difference in the sensor deflection among the sensing-plates solely arises from the mechanical difference among the measured tissue sites. Each sensing-plate was treated as a spring with a stiffness of k_s, and a sensor deflection, z_s. Then, the reaction force, F, to the deflection at the top of a sensing-plate becomes:

$$F = k_s \cdot z_s \tag{3.1}$$

Here, two defined tissue mechanical properties were extracted from the slope of both the instant and relaxed tissue stress-strain relations, which was different from the properties based on model parameters obtained by fitting a viscoelastic model to the experimental data.

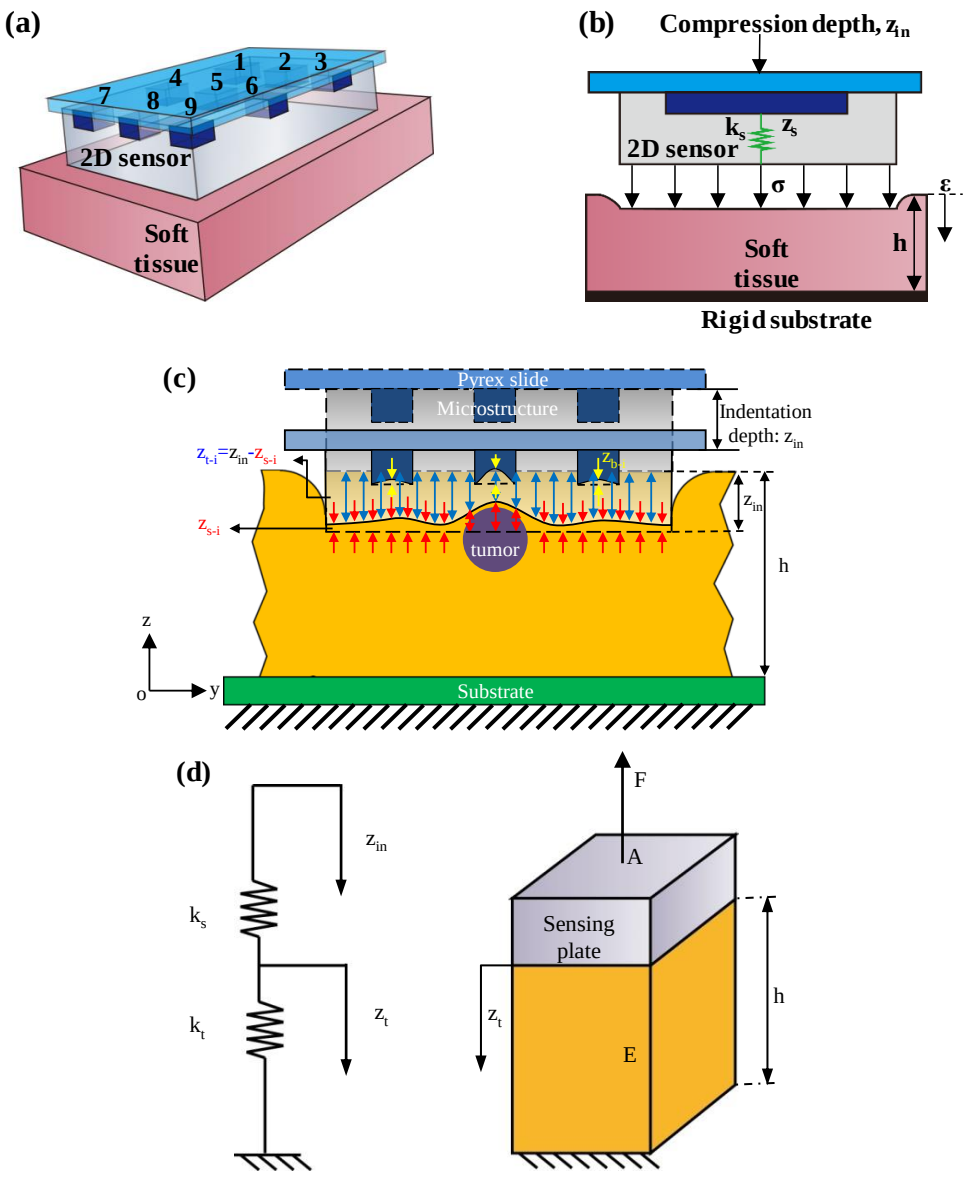

Figure 3.1 Rationale for the Stepwise Compression-Relaxation testing method (a) the whole configuration: the sensor with a 3×3 sensing-plate/transducer array compressing a soft tissue, (b) sensor-tissue interaction of one sensing-plate and the tissue segment underneath, (c) mechanical characterization of a tissue with embedded tumor using the 2D sensor, and (d) Theoretical models of a sensing-plate and the tissue segment underneath: lumped-model with two springs in series and block model with the tissue segment subjected to a deflection input, z_t, from the sensing-plate (out of proportion for better illustration).

In Figure 3.1 (a), a soft tissue was placed on a rigid substrate and the sensor is aligned on the tissue surface. Upon pressing the sensor against the tissue with a compression depth, z_{in}, both a sensing-plate and the tissue segment underneath undergo deflections. The sensor deflection at a sensing-plate, z_s, can be obtained from the readout of its transducer (Figure 3.2(b)). According to the deflection conformity, the tissue deflection, z_t, can be obtained by the difference between the compression depth, z_{in}, and the sensor deflection, z_s, of the sensing-plate:

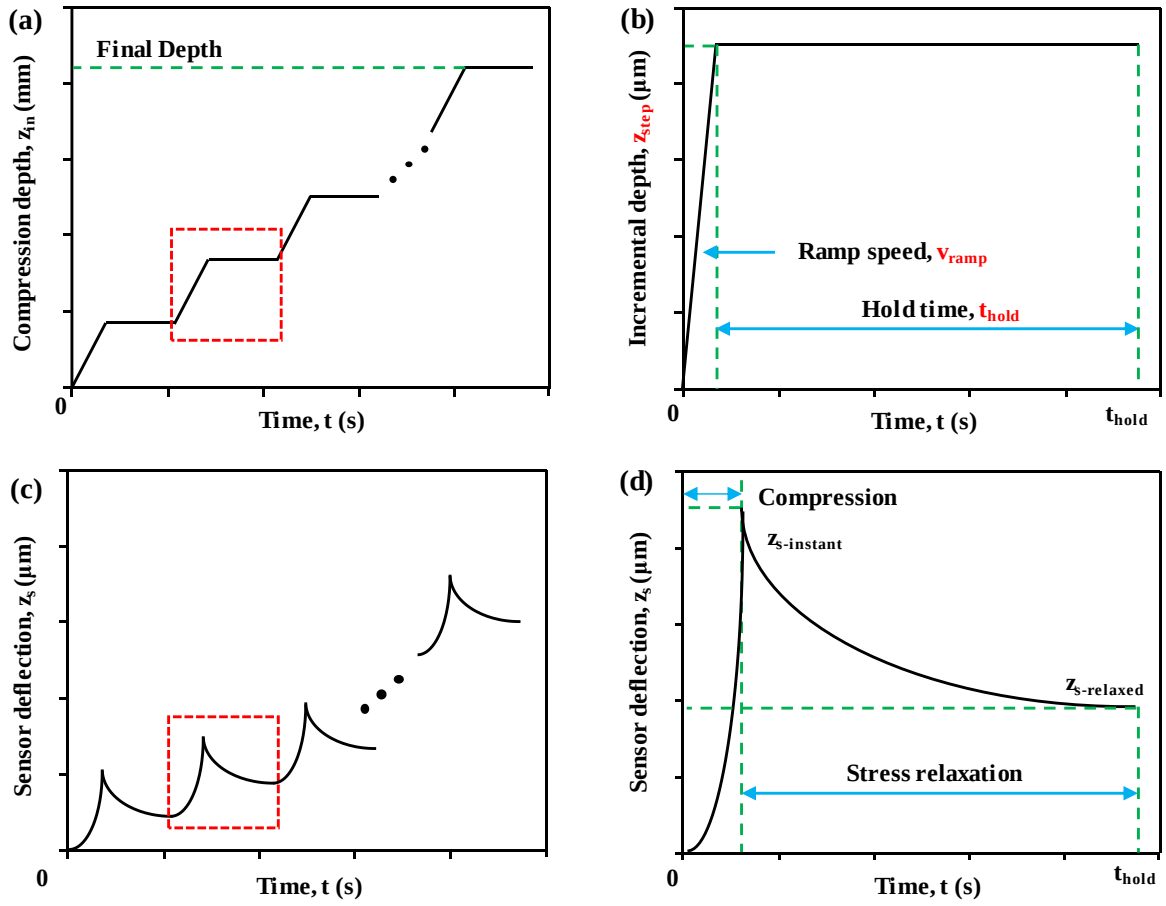

Figure 3.2 (a) Pre-defined compression pattern with a final compression depth of 3mm for soft animal tissues and 2mm for PDMS samples, (b) three testing parameters in each step incremental depth: z_{step}, hold time, t_{hold}, and ramp speed, v_{ramp}, (c) expected viscoelastic behavior of a sample captured by the sensor deflection, and (d) details of viscoelastic behavior upon each incremental compression depth.

$$z_t = z_{in} - z_s \tag{3.2}$$

The in-plane dimensions of the PDMS microstructure and a soft tissue were comparable, and thus the sensor-tissue interaction can be treated as the tissue being axially loaded by the PDMS microstructure. Upon a compression depth, the reaction force of a sensing-plate and its tissue segment was expressed by Equation 3.1. Now, we extract the tissue elasticity base on the tissue stress-strain relations. According to Equation 3.1 and Equation 3.2, the stress and the strain in the tissue segment are related to the sensor deflection at the *i-th* compression depth by:

$$\sigma_i = \frac{F_i}{A} = \frac{k_s \cdot z_{s-i}}{A} \tag{3.3}$$

$$\varepsilon_i = \frac{z_{t-i}}{h} = \frac{z_{in-i} - z_{s-i}}{h} \tag{3.4}$$

where σ_i is the tissue stress, ε_i denotes the tissue strain, h is the tissue thickness, A denotes the cross-section area of the tissue segment underneath a sensing-plate, and the subscript i denotes the parameters associated with the *i-th* compression depth. The nonlinearity of a tissue segment could be found in its stress-strain relation. Equations 3.3 and 3.4 were used to obtain the stress-strain relation of the measured tissue segment.

3.1.1 Elasticity

As shown in Figure 3.2(c), the measured data at a tissue site by the 2D sensor is the slope of the sensor deflection versus the compression depth, which is defined as the deflection slope:

$$\hat{z} = \frac{z_s}{z_{in}} \tag{3.5}$$

Note that the instant sensor deflection and relaxed sensor deflection give rise to the instant deflection slope and relaxed deflection slope, respectively. The ratio of the stiffness of the tissue segment, k_t, versus the sensor stiffness, k_s, is defined as the stiffness ratio:

$$\hat{k} = \frac{k_t}{k_s} \tag{3.6}$$

According to Equations 3.1 and 3.2, the measured stiffness ratio can be obtained from the measured deflection slope by:

$$\hat{k} = \frac{\hat{z}}{1-\hat{z}} \tag{3.7}$$

Consequently, the measured stiffness of the tissue segment can be extracted by:

$$k_t = \hat{k} \cdot k_s = \frac{\hat{z}}{1-\hat{z}} \cdot k_s \tag{3.8}$$

Evidently, the instant deflection slope and relaxed deflection slope yield the measured instant stiffness and relaxed stiffness of the tissue segment.

Varying with the tissue thickness, h, the stiffness of the tissue segment, k_t, does not represent the mechanical properties of the tissue itself. Thus, the tissue stiffness is suitable for comparing the mechanical behavior among different tissue sites in the same tissue of uniform thickness. However, owing to the thickness variation among the soft tissues, tissue stiffness could not be used for comparing the mechanical behavior among tissues with different thickness

In most related studies, a tumor tissue is treated as a semi-infinitely large medium so that the elasticity at a tissue site can be obtained from the measured stiffness by using related theoretical models [78], which have been well established in contact mechanics [79]. In this work, the in-plane dimension of the microstructure is comparable with that of a tumor tissue. During palpation, a large portion of the microstructure is in contact with the tissue surface and is pressed against the tissue. Thus, it is more suitable for treating the tissue segment underneath a sensing-plate as a block with a cross-section area, A, thickness, h, and instant elasticity, E, as shown in Figure 3.1(d). Its cross-section area is the same as the in-plane dimension of the sensing-plate.

As illustrated in Figure 3.2(c), in response to the pre-defined compression pattern, the expected corresponding viscoelastic behavior of a soft tissue. Upon each step incremental depth,

the reaction force on a tissue segment reaches its maximum value at the start of the hold time (t=0s) and then decreases to its minimum value at the end of the hold time (t=t_{hold}) due to the tissue viscosity. These two reaction forces, instant reaction force and relaxed reaction force, were recorded as the instant sensor deflection and the relaxed sensor deflection, respectively. The tissue elasticity, $E_{t\text{-}i}$, can be expressed by the ratio of the stress versus the strain:

$$E_{t-i} = \frac{\sigma_i}{\varepsilon_i} = \frac{z_{s-i}/z_{in-i}}{1-z_{s-i}/z_{in-i}} \cdot k_s \cdot \frac{h}{A} = \frac{\hat{z}}{1-\hat{z}} \cdot k_s \cdot \frac{h}{A} = k_t \cdot \frac{h}{A} \tag{3.9}$$

where $\hat{z}$ is the deflection-depth slope of sensor deflection, z_s, and compression depth, z_{in}. Evidently, the tissue elasticity can be obtained from each compression depth. However, to alleviate measurement errors associated with misalignment between the sensor and a tissue for the uncertainty in contact point, we measure the sensor deflection at multiple compression depth, via a predefined compression pattern for compressing a tissue via the sensor.

As illustrated in Figure 3.2(b), the 2D sensor is brought downward by a step incremental depth, z_{step}, at a ramp speed, v_{ramp}, and is held there for a hold time, t_{hold}, multiple times until the final compression depth, z_{final}, is reached. Then, free of measurement errors from uncertainty in contact point, the measured sensor deflection-compression depth slope defined in Equation 3.5, was used for extracting the tissue elasticity, as depicted in Equation 3.9. Thus, to alleviate measurement errors from uncertainty in contact point, the ratio of stress and strain is related to the sensor deflection versus compression depth at each data point, which is replaced with the measured deflection-depth slope in the above equation.

According to Equation 3.9, tissue elastic behavior is characterized as the tissue instant elasticity as the start of the hold time, $E_{instant}$, which is calculated as:

$$E_{instant} = \frac{\hat{z}_{instant}}{1-\hat{z}_{instant}} \cdot k_s \cdot \frac{h}{A} = k_t \cdot \frac{h}{A} \tag{3.10}$$

where $\hat{z}_{instant}$ denotes the measured instant deflection-depth slope, as illustrated in Figure 3.3(a). The measured instant and relaxed stiffness yield the measured instant and relaxed elasticity, respectively. Since the cross-section areas remain the same for the measured tissue sites in all the tumor tissues, the tissue elastic modulus is related to the measured stiffness and the tissue thickness only. As will be seen in Chapter 5, the instant and relaxed elastic modulus of the tumor tissues is very close. Later on, the instant elasticity is chosen for characterizing the elastic behavior of soft tissues as well as determining the location, shape and size of a tumor in a tissue.

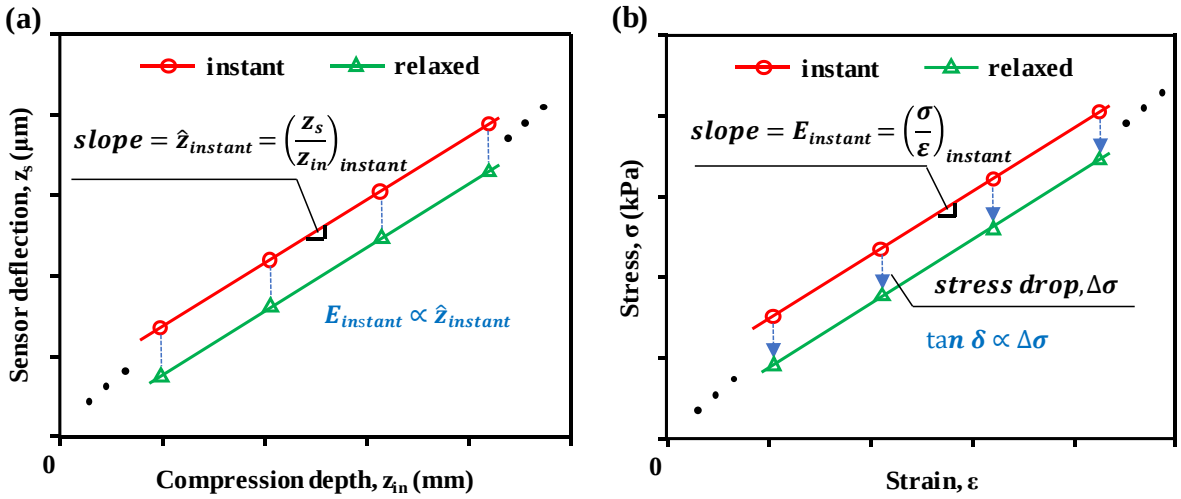

Figure 3.3 Definition of the mechanical properties derived from the Stepwise Compression-Relaxation testing method: (a) instant elasticity, $E_{instant}$, determined by the measured instant deflection-depth slope and (b) loss tangent, tan δ, determined by the measured stress drop.

3.1.2 Viscoelasticity

According to Equations 3.3 and 3.4, the stress and strain at the start and end of the hold time at the *i-th* compression depth are the instant stress and strain and the relaxed stress and strain, respectively:

$$\sigma_{instant-i} = \frac{k_s \cdot z_{s-i}(t=0s)}{A}; \varepsilon_{instant-i} = \frac{z_{in-i} - z_{s-i}(t=0s)}{h_t} \tag{3.11}$$

$$\sigma_{relaxed-i} = \frac{k_s \cdot z_{s-i}(t = t_{hold})}{A}; \varepsilon_{relaxed-i} = \frac{z_{in-i} - z_{s-i}(t = t_{hold})}{h_t} \tag{3.12}$$

As shown in Figures 2(b) and 2(d), the tissue segment undergoes stress relaxation in the hold time upon each step incremental depth, which translates to a constant strain input, ε_0:

$$\varepsilon_0 = \frac{z_{step}}{h} \tag{3.13}$$

In response to the strain input, the stress of the tissue segment varies with time:

$$\sigma(t) = E(t) \cdot \varepsilon_0 \tag{3.14}$$

where $E(t)$ is the relaxation modulus of the tissue.

Now, we define the normalized relaxation amount, $\Delta\bar{E}$, as the drop in the relaxation modulus over the hold time normalized to the instant elasticity, $E_{instant}$:

$$\Delta\bar{E} = \frac{E(t = 0s) - E(t = t_{hold})}{E_{instant}} \tag{3.15}$$

By substituting Equations 3.11-3.14 into Equation 3.15, the normalized relaxation amount can be expressed in terms of the stress drop, $\Delta\sigma_i$, over the hold time at the *i-th* compression depth:

$$\Delta\bar{E} = \frac{\Delta\sigma_i}{\sigma_{in}} = \frac{\Delta\sigma_i}{\frac{z_{step}}{h} \cdot E_{instant}} = \frac{\sigma_{instant-i} - \sigma_{relaxed-i}}{\frac{z_{step}}{h} \cdot E_{instant}} = \frac{\sigma_{instant-i} - \sigma_{relaxed-i}}{\frac{z_{step}}{h} \cdot \frac{\hat{z}_{instant}}{1 - \hat{z}_{instant}} \cdot k_s \cdot \frac{h}{A}} = \frac{\sigma_{instant-i} - \sigma_{relaxed-i}}{z_{step} \cdot \frac{\hat{z}_{instant}}{1 - \hat{z}_{instant}} \cdot \frac{k_s}{A}} \tag{3.16}$$

Figure 3.3(b) illustrates the stress drop as a function of the strain, which is obtained from sensor deflection, z_s, by using Equations 3.11 and 3.12. Owing to the small sensor deflection, the instant strain and the relaxed strain at each compressions depth are very close to each other.

The measured stress drop, $\Delta\sigma_i$, during the hold time is related to the strain drop, $\Delta\varepsilon_i$, and the instant elasticity, $E_{instant}$:

$$\Delta\varepsilon_i \propto \frac{\Delta\sigma_i}{E_{instant}} \tag{3.17}$$

According to the experimental observation, the strain drop is positively correlated to the sample thickness. According to the definition of loss modulus, the strain drop is also positively

correlated to the loss modulus. Thus, we assume that the strain drop is linearly proportional to the loss modulus and sample thickness:

$$\Delta\varepsilon_i = \frac{\Delta\sigma_i}{E_{instant}} \propto E'' \cdot h \tag{3.18}$$

where *E''* denotes the loss modulus, and h is the sample thickness.

Consequently, the loss modulus can be expressed in terms of the ratio of the stress drop versus the applied step strain:

$$E'' \propto \frac{\Delta\sigma_i}{\varepsilon_{in}} \cdot \frac{z_{step}}{E_{instant} \cdot h^2} \propto \frac{\Delta\sigma_i}{\varepsilon_{in} \cdot E_{instant}} \cdot \frac{z_{step}}{h^2} \tag{3.19}$$

By substituting Equation 3.13 and Equation 3.16 into Equation 3.19 the loss modulus can be related to the normalized relaxation amount and thickness:

$$E'' \propto \frac{\Delta\bar{E}}{h^2} \tag{3.20}$$

Then the loss tangent can be expressed as the ratio of loss modulus (Equation 3.20) to the storage modulus (instant elasticity) and gives a measure of the viscous portion to the elastic portion of the measured sample.

$$\tan\delta = \frac{E''}{E_{instant}} \propto \frac{\Delta\bar{E}}{E_{instant} \cdot h^2} \tag{3.21}$$

3.1.3 Relation Between Stress Drop and Applied Strain

As reported in literature [80], the generalized Maxwell model is given as:

$$E(t) = \sigma(t)/\varepsilon_0 = \int_0^\infty E(\lambda) \cdot \exp(-\frac{t}{\lambda}) \cdot d\lambda \tag{3.22}$$

where relaxation modulus $E(t)$ is a characteristic of soft tissue viscoelasticity to describe the stress relaxation of a soft tissue at time t, $\sigma(t)$ is the stress at time t, ε_0 is imposed strain. $E(\lambda)$ is the continuous distribution function of relaxation times, λ is the relaxation time. In response to the constant strain input at each step compression depth, the stress of a tissue varies with time is expressed as follows:

$$\sigma(t) = E(t) \cdot \varepsilon_0 = \varepsilon_0 \cdot \int_0^{\infty} E(\lambda) \cdot \exp(-\frac{t}{\lambda}) \cdot d\lambda \tag{3.23}$$

Figure 3.3(b) illustrates the stress as a function of the strain, and the stress drop, $\Delta\sigma_i$, at each step compression depth. The generalized Maxwell model depicts the relaxation modulus, $E(t)$, as follows [81]:

$$E(t) = E_{\infty} + \sum_{j=1}^{n} E_i \cdot e^{-(E_j/\eta_j)\cdot t} = E_{\infty} + \sum_{j=1}^{n} E_j \cdot e^{-t/\tau_j} \tag{3.24}$$

where E_∞ is the tissue elasticity at infinite time t=∞; E_j, η_j, and τ_j are the elasticity, viscosity, and the relaxation time constant associated with the *j-th* spring-dashpot series, and n is the total number of spring-dashpot series used in the Maxwell model. A generalized Maxwell model consists of five elements, namely a Double Maxwell-arm Wiechert (DMW), was reported as a suitable compressive material model to describe the stress relaxation of biological tissues due to the maintained balance between the mathematical simplicity and experimental performance [46]. As depicted in Figure 3.1(b), a soft tissue was modeled by the DMW model, and the stress varies with time can be expressed by:

$$\sigma_i(t) = \varepsilon_0 \cdot E_i(t) = \varepsilon_0 \cdot (E_{\infty(i)} + E_{1(i)} \cdot e^{-(E_{1(i)}/\eta_{1(i)})\cdot t} + E_{2(i)} \cdot e^{-(E_{2(i)}/\eta_{2(i)})\cdot t}) \tag{3.25}$$

where $E_1(i)$, $\eta_1(i)$, and $E_2(i)$, $\eta_2(i)$, are the elasticity and viscosity of the spring and dashpot, respectively, for the two Maxwell-arm in the DMW model, the subscript i denotes the parameters associated with the *i-th* step compression depth.

To simplify the data-processing and meanwhile capture the viscoelastic variation among different tissue sites, the following two assumptions were made: 1) a tissue segment (or tissue site) underneath a sensing-plate was under 1D axial compression by the sensing-plate; and 2) its connection to the rest tissue (including the rest tissue sites) was neglected. The sensor deflection at a tissue site was much smaller than the tissue deflection, and thus was neglected. Although this definition of the strain at a tissue site neglected the existence of the rest tissue, the measured strain still captured the effect of the rest tissue on the tissue site, since the strain at a tissue site

was a collective mechanical response of the sensor-tumor interaction. Despite the influence of the rest tissue, the measured strain at a tissue site still manifested the salient mechanical behavior of the tissue site, as will be seen later on in this work and our previous work [70].

Based on Equations 3.3 and 3.4, the stress and strain at the start and end of the hold time at the *i-th* step compression depth are the instant stress and strain and the relaxed stress and strain, respectively:

$$\begin{cases} \sigma_{instant-i} = \sigma(t=0) = (k_s \cdot z_{s-i}(t=0))/A & \text{(a)} \\ \varepsilon_{instant-i} = \varepsilon(t=0) = (z_{in-i} - z_{s-i}(t=0))/h_t & \text{(b)} \end{cases} \tag{3.26}$$

$$\begin{cases} \sigma_{relaxed-i} = \sigma(t=t_{hold}) = (k_s \cdot z_{s-i}(t=t_{hold}))/A & \text{(a)} \\ \varepsilon_{relaxed-i} = \varepsilon(t=t_{hold}) = (z_{in-i} - z_{s-i}(t=t_{hold}))/h_t & \text{(b)} \end{cases} \tag{3.27}$$

It can be assumed that in the stress relaxation phase, strain keeps unchanged. Based on Equation 3.25, the first-order derivative and second-order derivative of stress, $\Delta\dot{\sigma}$ and $\Delta\ddot{\sigma}$, can be formed as Equation 3.28(a) and Equation 3.28(b), respectively:

$$\begin{cases} \dot{\sigma}_i(t) = \varepsilon_0 \cdot \dot{E}_i(t) = -\varepsilon_0 \cdot ((E^2_{1(i)}/\eta_{1(i)}) \cdot e^{-(E_{1(i)}/\eta_{1(i)})\cdot t} + (E^2_{2(i)}/\eta_{2(i)}) \cdot e^{-(E_{2(i)}/\eta_{2(i)})\cdot t}) < 0 & \text{(a)} \\ \ddot{\sigma}_i(t) = \varepsilon_0 \cdot \ddot{E}_i(t) = \varepsilon_0 \cdot ((E^3_{1(i)}/\eta^2_{1(i)}) \cdot e^{-(E_{1(i)}/\eta_{1(i)})\cdot t} + (E^3_{2(i)}/\eta^2_{2(i)}) \cdot e^{-(E_{2(i)}/\eta_{2(i)})\cdot t}) > 0 & \text{(b)} \end{cases} \tag{3.28}$$

The first-order derivative of stress $\Delta\dot{\sigma}$ is a negative value, and thus a tissue experiences stress relaxation at the hold time and stress keeps decreasing. Now, we define the stress drop, $\Delta\sigma_i$ during the hold time at the *i-th* compression depth as:

$$\Delta\sigma_i = \int_0^{t_{hold}} \dot{\sigma}(t) \cdot dt = \sigma_i(t=0) - \sigma_i(t=t_{hold}) = \sigma_{instant-i} - \sigma_{relaxed-i} \tag{3.29}$$

By substituting Equation 3.25 into Equation 3.29, the stress drop, $\Delta\sigma_i$, at the *i-th* compression depth can be also expressed in terms of the drop of relaxation modulus, ΔE_i, throughout the hold time, t_{hold}, at the *i-th* compression depth. Thus, the stress drop defined in Equation 3.29 can be expressed as:

$$\Delta\sigma_i = \int_0^{t_{hold}} \dot{\sigma}_i(t) \cdot dt = \varepsilon_0 \cdot (E_{1(i)}(1 - e^{-(E_{1(i)}/\eta_{1(i)})\cdot t_{hold}}) + E_{2(i)}(1 - e^{-(E_{2(i)}/\eta_{2(i)})\cdot t_{hold}})) \tag{3.30}$$

As depicted in Equation 3.30, $\sigma_i(t)$, is a concave function, keeps decreasing at stress relaxation phase, and the amount of stress drop $\Delta\sigma_i$, is determined by the absolute value of the first-order derivative of stress, $\left|\dot{\sigma}_i(t)\right|$, which mainly depends on $E_{1(i)}$ and $E_{2(i)}$. Noted that a lager value of $\left|\dot{\sigma}_i(t)\right|$ means stress drops faster.

$$\begin{cases} \dot{E}_{1(i)} = 0 \wedge \dot{E}_{2(i)} = 0 \Rightarrow \left|\dot{\sigma}_i(t)\right| \rightarrow \Rightarrow \Delta\sigma_i \rightarrow & \text{(Case1)} \\ \dot{E}_{1(i)} > 0 \wedge \dot{E}_{2(i)} > 0 \Rightarrow \left|\dot{\sigma}_i(t)\right| \nearrow \Rightarrow \Delta\sigma_i \nearrow & \text{(Case 2)} \\ \dot{E}_{1(i)} < 0 \wedge \dot{E}_{2(i)} < 0 \Rightarrow \left|\dot{\sigma}_i(t)\right| \searrow \Rightarrow \Delta\sigma_i \searrow & \text{(Case 3)} \end{cases} \tag{3.31}$$

It should be noted that $E_{1(i)}$ and $E_{2(i)}$ always change in the same direction in response to compression, either increase or decrease at hold time, simultaneously, due to the configuration of the DMW model. The influence of $E_{1(i)}$ and $E_{2(i)}$ on the variations of stress drop is analyzed in Equation 3.31, where $\dot{E}_{1(i)}$ and $\dot{E}_{2(i)}$ are the first-order derivative of $E_{1(i)}$ and $E_{2(i)}$, respectively. There are three cases: 1) if $E_{1(i)}$ and $E_{2(i)}$ keep unchanged ($\dot{E}_{1(i)} = 0$ and $\dot{E}_{2(i)} = 0$), the absolute value of stress derivative remains unchanged ($\left|\dot{\sigma}_i(t)\right| \rightarrow$), and thus stress drop remains constant ($\Delta\sigma_i \rightarrow$) over the applied strain; 2) if $E_{1(i)}$ and $E_{2(i)}$ increase ($\dot{E}_{1(i)} > 0$ and $\dot{E}_{2(i)} > 0$), the absolute value of the stress derivative goes up ($\left|\dot{\sigma}_i(t)\right| \nearrow$), and thus give rise to an increased stress drop, ($\Delta\sigma_i \nearrow$) over the applied strain; and 3) if $E_{1(i)}$ and $E_{2(i)}$ decrease ($\dot{E}_{1(i)} < 0$ and $\dot{E}_{2(i)} < 0$), the absolute value of the stress derivative drops ($\left|\dot{\sigma}_i(t)\right| \searrow$), results into an reduced stress drop ($\Delta\sigma_i \searrow$) over the applied strain.

It is hypothesized that changes in physical microstructure of a tumor-affected tissue site alter the mechanical properties of the tissue [82]. Tissue elasticity, $E_{1(i)}$ and $E_{2(i)}$, changed at each of the *i-th* step compression depth, which further leading into variations in the amount of stress drop at each of the *i-th* step compression depth. Thus, tissue stress drop-strain relation holds the

potential to be used for differentiation of normal tissue and tumor tissue which reveal different viscoelastic behaviors.

3.2 Finite Element Analysis

This section aims to evaluate the sensitivity of the measured tissue elastic modulus that characterizes tissue elastic behavior to tissue parameters. With the testing parameters being fixed and the same sensor being utilized, it is desirable that the measured tissue elasticity is immune to the tissue parameters: thickness, elasticity, and in-plane dimension for achieving measurement consistency. A finite element model is created in COMSOL Multiphysics (version 5.1, COMSOL, Inc., Burlington, MA) to simulate the sensor-tissue interaction in a measurement. In the model, the sensor is represented by the PDMS microstructure and the Pyrex substrate, since electrolyte in the microchannel does not affect the elasticity measurement. The sensor is aligned at the top center of the tissue underneath.

For the boundary conditions, the bottom surface of the tissue is fixed. For the loading condition, the input is the compression depth acting on the Pyrex substrate. The output of the FE analysis is the sensor deflection (*z*-displacement) at the top center of each of the 3×3 sensing-plate array. The average value of the sensor deflections from the nine sensing-plates is used to represent the sensor deflection. Thus, the numerical analysis result is the average deflection-depth slope, which mimics the measured deflection-depth slope in experiment.

With the sensor parameters being fixed in the FE model, the tissue elasticity, thickness, and in-plane dimension are varied separately to examine how they affect the deflection-depth slope and the measured tissue elasticity. As listed in Table 3.1, there are three tissue parameters, tissue elasticity, E_t, tissue thickness, h, and tissue in-plane dimension, $x_t \times y_t$. To estimate how the simulated tissue elasticity (equivalent to the measured tissue elasticity) varies with the tissue

thickness at different tissue elasticity ranging from 25kPa to 200kPa, the in-plane dimension of the tissue is fixed at 20mm×20mm, and the tissue thickness is increased by 3mm at a time in the range of 3mm-18mm. Similarly, to examine the effect of tissue in-plane dimension on the measured tissue elasticity, the tissue thickness is fixed at 12mm, the tissue elasticity is fixed at 100kPa, and the tissue in-plane dimension is varied from 10mm×10mm to 40mm×40mm with an increment of 5mm×5mm at a time.

Table 3.1 Variable tissue parameters used in the FE simulation.

Tissue parameters	Values	Symbol
Tissue elasticity, (kPa)	25-200 (increment: 25)	E_t
Tissue thickness, (mm)	3-18 (increment: 3)	h_t
Tissue in-plane dimension, (mm)	10×10-40×40 (increment: 5×5)	$x_t \times y_t$

As shown in Figure 3.4, the *z*-displacement distribution of the tissue-sensor interaction with an input compression depth of 4mm acting on the surface of a soft tissue, a higher *z*-displacement value was found in the contact surface between the soft tissue and 2D sensor. While Figures 3.5(a) and 3.5(b) illustrate the simulated *z*-displacement distribution of the contact surface on the PDMS microstructure and the top surface of the 3×3 sensing-plates/ transducer array across the x-y plane by FEM analysis, respectively. It should be noted that the distributed deflection, *z*-displacement, acting on top of the sensing-plate array translates into their geometrical changes, and registered as resistance changes. Next, the analytical method discussed in the prior section is used to relate the tissue stiffness, k_t, and tissue elasticity, E_t, of a tissue site above a sensing-plate to the deflection slope of the sensing-plate top deflection versus the compression depth. Noted that it was the average value of the sensor deflections from the nine sensing-plates that is used to represent the sensor deflection. Therefore, the numerical result was

the average deflection-depth slope, which mimics the deflection-depth slope measured in an experiment, and then Equations 3.8 and 3.10 were used to extract the tissue stiffness and the tissue elasticity from the simulated deflection-depth slope by the FEM analysis, respectively.

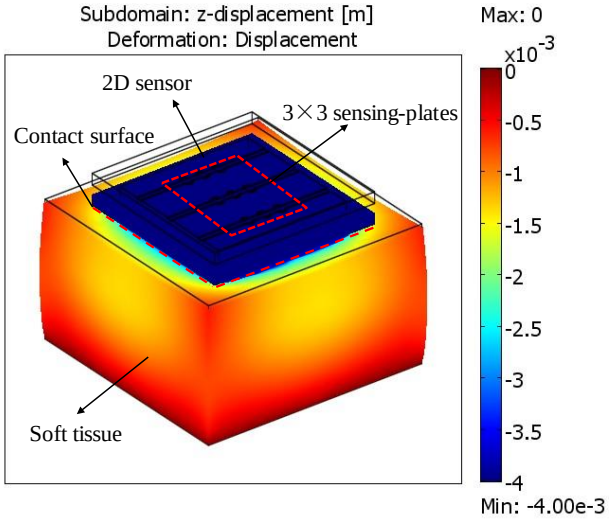

Figure 3.4 FE simulation of the *z*-displacement distributions of the tissue-sensor interaction in the measurement using the SCR testing method with a 4mm compression depth applied on the tissue surface.

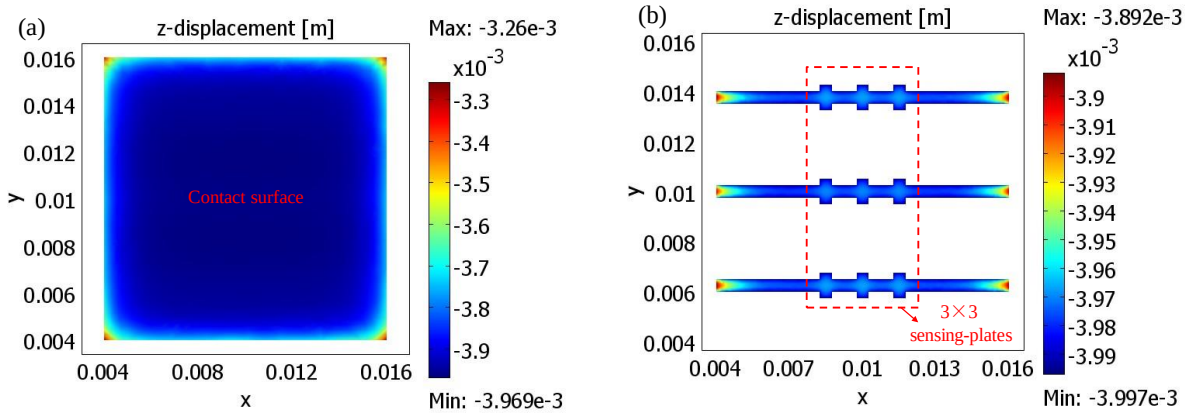

Figure 3.5 FE simulation of the *z*-displacement distribution with a compression depth input of 4mm occurring at (a) the contact surface on the PDMS microstructure of the 2D sensor across the x-y plane, and (b) the top surface of the 3×3 sensing-plates/ transducer array across x-y plane.

Figure 3.6(a) illustrates the simulated tissue stiffness from the FE analysis, equivalent to the measured tissue stiffness, as a function of the tissue thickness at different tissue elasticities ranging from 25kPa to 200kPa. The results showed that tissue stiffness dropped with the tissue thickness at the same tissue elasticity. It was clear that the simulated tissue stiffness decreased fast at small tissue thickness and decreases slow at large tissue thickness, while at the same tissue thickness, the simulated tissue stiffness increased with the tissue elasticity. At a small tissue thickness, the increase of the simulated tissue stiffness increased fast with the tissue elasticity, but, at a large tissue thickness, the increase of simulated tissue stiffness goes up slowly with the tissue elasticity. The tissue behaved as a block under the axial loading from the 2D sensor, and thus its simulated stiffness increased with its elasticity, and decreased with its thickness. However, comparison of the simulated tissue stiffness with the theoretical tissue stiffness, obtained from the analytical method, revealed that a relatively large difference between the two exists when the tissue thickness was low, such as 3mm and 6mm. When the tissue thickness was in the range of 9mm~18mm, the difference between the two remains unchanged at approximately 20%. The simulation results showed that at small tissue thickness, the constraint at the bottom surface of a tissue, equivalent to a rigid substrate, led to an increase in the simulated tissue stiffness by amplifying the force at the sensor-tissue interface; while at large tissue thickness, the bottom boundary showed less influence on the simulated tissue stiffness, due to its large distance from the sensing-plates.

As shown in Figure 3.6(b), the simulated tissue elasticity varied with the tissue thickness at different tissue elasticity. It should be noted that the simulated tissue elasticity varied very slightly with the tissue thickness, when it is in the range of 9mm-18mm. The simulated tissue elasticity at small tissue thickness (3mm and 6mm) is moderately higher than that at large tissue

thickness. This results from large measured tissue stiffness on a tissue with low thickness. Therefore, the analytical method presented in the previous section for the calculation of tissue

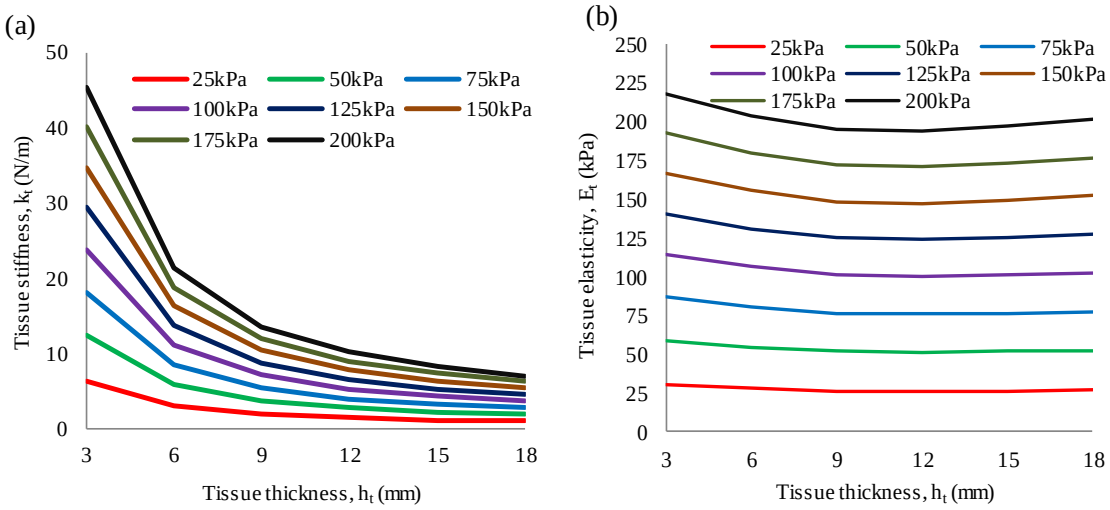

Figure 3.6 FE analysis results of (a) tissue stiffness, and (b) tissue instant elasticity as a function of tissue thickness at different tissue elasticity (E_t: 25kPa-200kPa), with the tissue in-plane dimension fixed at 20mm×20mm.

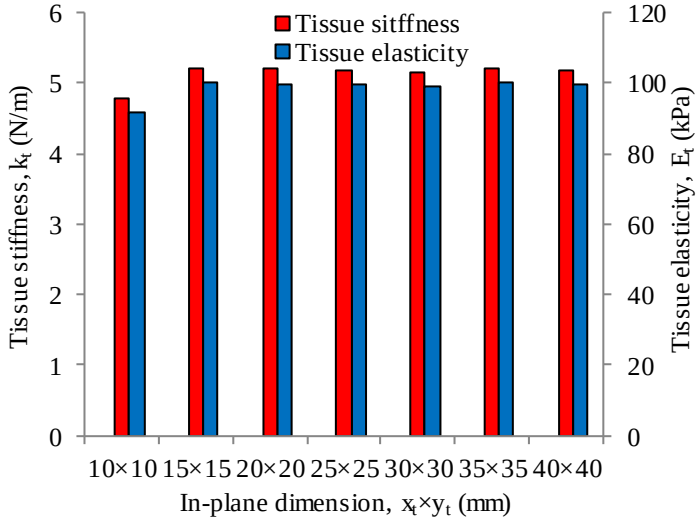

Figure 3.7 FE analysis results of tissue stiffness and estimated tissue elasticity as a function the tissue in-plane dimension, with the tissue elasticity E_t fixed at 100kPa and tissue thickness h fixed at 12mm.

elasticity was insensitive to the tissue thickness, when the tissue thickness was larger than 6mm.

However, the simulated tissue elasticity for large tissue thickness overestimates the inherent tissue elasticity in the range of 25kPa~200kPa by 20%. It was believed that this overestimate results from the neglect of the tissue between the sensing-plates in the analytical method. To compensate for the overestimate, the simulated tissue elasticity in Figure 3.6(b) was 80% of the tissue instant elasticity calculated using Equation 3.10. Moreover, an extra compensation for the measured tissue elasticity on a 3mm-thick tissue and a 6mm-thick tissue was to further reduce their tissue elasticity by 13% and 5%, respectively, which was not included in Figure 3.6(b).

Figure 3.7 shows how the simulated tissue stiffness and tissue elasticity varied with the tissue in-plane dimension, when the tissue elasticity and tissue thickness were fixed at 100kPa and 12mm, respectively. Smaller than the sensor in-plane dimension, a 10mm×10mm tissue in-plane dimension gave rise to a lower simulated tissue stiffness and tissue elasticity. The simulated tissue stiffness and the simulated tissue elasticity remained the same with the tissue in-plane dimension, when the tissue in-plane dimension was larger than that of the PDMS microstructure with 12mm×12mm. The same as Figure 3.6(b), the simulated tissue elasticity in Figure 3.7 was also compensated as 80% of the tissue instant elasticity calculated using Equation 3.10.

3.3 Conclusion

This chapter presented the SCR testing method built upon a 2D tactile sensor that allows consistent characterization of soft tissues with different thickness and differentiation of tumor tissues and normal tissues. The 2D sensor entails a polydimethylsiloxane (PDMS) microstructure embedded with a 3×3 sensing-plate/transducer array [70]. In the SCR testing method, a tissue

was compressed by the sensor with a step incremental depth at a ramp speed and then relaxed for certain hold time multiple times until a final compression depth was reached. It was noted that the compression and relaxation phase was designed to characterize the tissue elastic and viscous behavior, respectively, and the multiple step incremental compression was designed to alleviate the error caused by the uncertainty of contact points. The time-dependent response of the tissue was recorded as the sensor deflection, and the instant and relaxed sensor deflections were recorded at the start and end of the hold time, respectively. Thus, the measured results on a tissue are the relation of instant sensor deflections, relaxed sensor deflection. First, the measured sensor deflections were further related to the tissue stress-strain relation to characterize tissue mechanical properties. An analytical model was established to translate the measured data into two identified tissue mechanical properties, the instant elasticity and loss tangent, to characterize the tissue elasticity and viscoelasticity, respectively. These two tissue properties, in conjunction with the testing method, were immune to tissue thickness and measurement errors associated with misalignment, and thus allow consistent measurements among soft tissues of different thickness. The stress drop at each step incremental depth was registered as the difference between the measured instant and relaxed sensor deflections, and the measured sensor deflections were converted into the relation between stress drop and applied strain for tumor detection.

The related 3D finite element analysis was conducted to examine the sensitivity of the measured results to tissue parameters, such as tissue elasticity, thickness, and in-plane dimension. The FE analysis results indicated that the measured tissue elasticity did not vary with tissue thickness when the tissue thickness was above 6mm, and smaller tissue thickness led to a higher measured tissue elasticity, while the measured tissue elasticity was found to be insensitive to this

tissue parameter as far as the tissue in-plane dimension was larger than the sensor in-plane dimensions, 12mm×12mm, and the analytical method led to a roughly 20% overestimation on the measured tissue elasticity, when the tissue elasticity varied from 25kPa to 200kPa.

CHAPTER 4

MECHANICAL CHARACTERIZATION BASED ON MEASURED SENSOR DEFLECTIONS

Stepwise compression-relaxation (SCR) testing methods measure a variety of native soft tissues and biomaterials, including cartilage tissues, vascular tissue constructs, breast tumor tissues and collagen gels [66-70]. The measured data were the instant stress and relaxed stress at the beginning and end of each applied strain, respectively, and were further processed to obtain instant/relaxed elasticity by extracting the slope of instant/relaxed stress versus applied strain. The tissue viscosity was quantified as the slope of the difference between instant stress and relaxed stress versus applied strain [69, 70].

This chapter describes the application of the stepwise compression relaxation (SCR) testing method for mechanical characterization of soft tissues. A three-factor-three-level factorial design was first applied to the data of soft materials (PDMS/silicone rubbers) to investigate the individual and interaction effects of testing parameters on the measured mechanical properties. Next, feasibility of the SCR testing method was experimentally validated by measurements on soft tissues, including both porcine and bovine tissues. Details about the sample preparation, experimental setup, experimental procedures, measured results, discussion and conclusion were presented.

4.1 Materials and Methods

4.1.1 Sample Preparation

4.1.1.1 Soft Materials

Commercially available PDMS and silicone rubbers were used as calibration samples for evaluating the capability of the SCR testing method in distinguishing soft tissues from the

measured mechanical properties and studying the effects of testing parameters on the measured results. In this study, six PDMS samples with three different mixing ratios (curing agent to base of Sylgards 184kit, Dow Corning Corp.) of 1:10 (Young's modulus, 580kPa [83]), 1:20 (Young's modulus, 445kPa [84]), and 1:30 (Young's modulus, 170kPa [84]) were prepared using two different thickness, 6mm (1:10_6, 1:20_6, and 1:30_6) and 10mm (1:10_10, 1:20_10, and 1:30_10), respectively. On the other hand, three silicone rubbers (Mold Star^{TM}30, blue, Young's Modulus, 662kPa (MS30) [85]; Mold Max^{TM} 10T, Young's Modulus, 200kPa (MM10T), [86]; Dragon Skin$^{®}$ 10, Young's Modulus, 152kPa (DS10), [87]) were also measured in this study, respectively. The thicknesses and in-plane dimension of the soft materials were summarized in Table 4.1 (a).

4.1.1.2 Normal Tissues

Large chunks of different soft animal tissues were bought at a local grocery store. Eight soft tissue samples were prepared by cutting into them for meeting three requirements: 1) the in-plane dimension of each tissue sample was relatively larger than the in-plane dimension of the PDMS microstructure in the sensor, in order to alleviate the effect of the tissue in-plane dimension on the measured tissue elasticity; 2) the thickness of the tissue samples varied from 4mm to 19mm for examining their effect on the measured results; and 3) different types of tissues were utilized for comparison. Figure 4.1(a) shows these soft tissue samples with the sensor on their tops for comparison of the tissue size with the sensor size. The thicknesses and in-plane dimension of the soft tissues were summarized in Tables 4.1 (b) and 4.1(c).

4.1.1.3 PDMS Samples with Embedded Silicone Rubbers

Three 3mm-thick PDMS samples with 1:30 (mixing ratio of curing agent and base of Sylgards 184kit, Dow Corning Corp.) were prepared. As shown in Figure 4.1(b), the PDMS

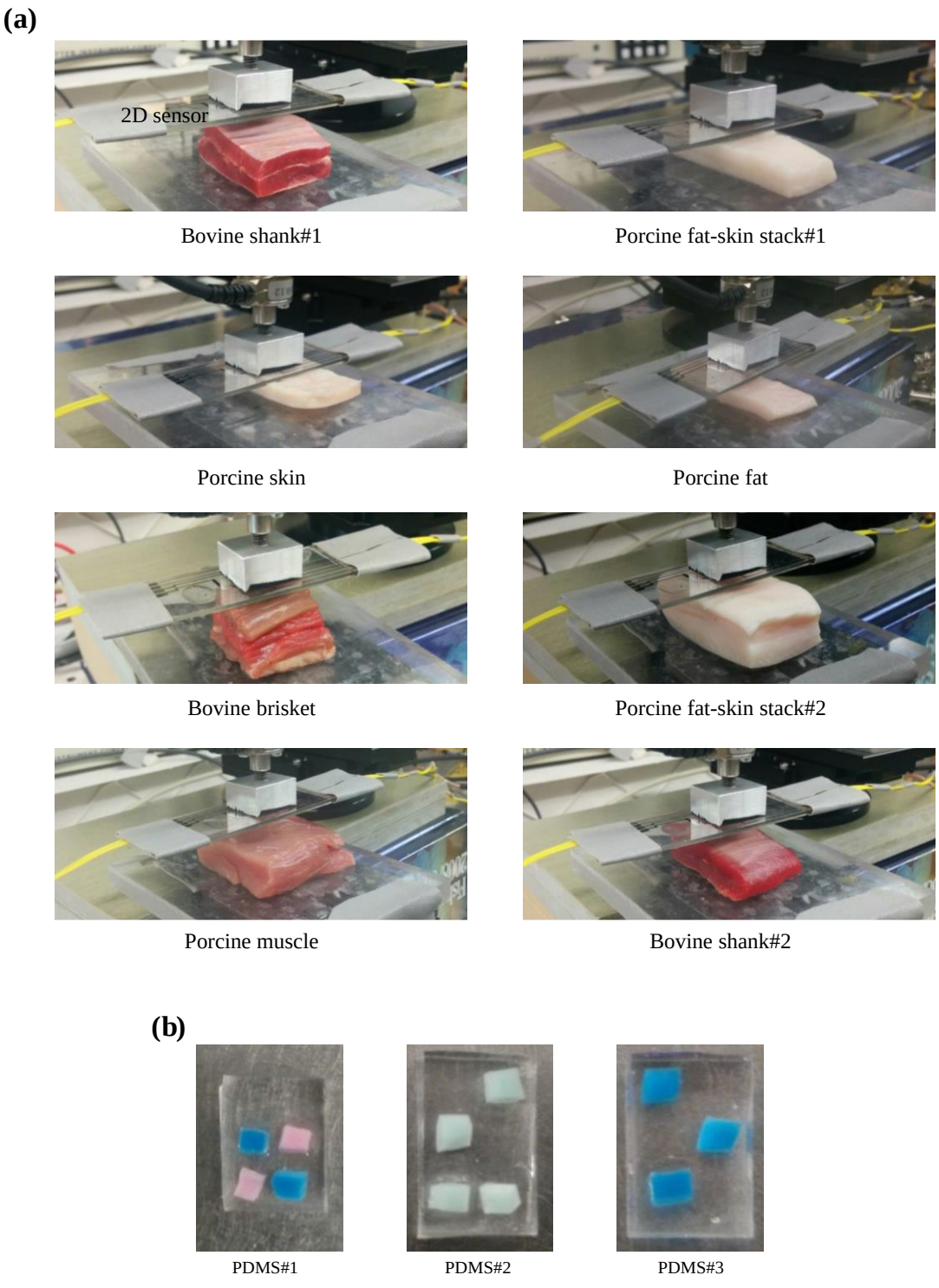

Figure 4.1 Pictures of the prepared soft animal tissues and their dimensions relative to the 2D tactile sensor and three PDMS samples (a) eight soft animal tissues and (b) three PDMS samples.

Table 4.1 Key parameters and their values of (a) the PDMS (P1-P6)/silicone rubbers (SR1-SR3), (b) normal tissues (NT1-NT6), (c) normal tissues without (NT1_NO_DT-NT3_NO_DT)/ with dummy tumor (NT1_DT-NT3_DT), and (d) the PDMS samples with embedded silicone rubbers.

(a)

Sample No.	Soft materials	*h* (mm)	*x*×*y* (mm)	*E* (kPa)
P1	1:10 PDMS (1:10_6)	6	18×17	580
P2	1:20 PDMS (1:20_6)	6	18×17	445
P3	1:30 PDMS (1:30_6)	6	18×17	170
P4	1:10 PDMS (1:10_10)	10	19×16	580
P5	1:20 PDMS (1:20_10)	10	19×17	445
P6	1:30 PDMS (1:30_10)	10	19×18	170
SR1	Mold Star 30 (MS30)	4	18×17	662
SR2	Mold Max 10T (MM10T)	4	18×18	200
SR3	Dragon Skin 10 (DS10)	6	18×17	152

(b)

Tissue No.	Normal tissues	*h* (mm)	*x*×*y* (mm)
NT1	Bovine shank#1 (BS1)	11	26×37
NT2	Bovine shank#2 (BS2)	10	27×42
NT3	Bovine brisket (BB)	19	33×34
NT4	Porcine skin (PS)	4	23×47
NT5	Porcine fat (PF)	5	20×44
NT6	Porcine fat-skin stack#1 (PFSS1)	10	20×50

(c)

Tissue No.	Normal tissues	*h* (mm)	*x*×*y* (mm)
NT1_NO_DT	Porcine fat-skin stack#2 (PFSS2)	18	29×42
NT1_DT	Porcine fat-skin stack#2 with dummy tumor	21	29×42
NT2_NO_DT	Porcine muscle (PM)	13	43×40
NT2_DT	Porcine muscle with dummy tumor	16	43×40
NT3_NO_DT	Chicken heart	18	-
NT3_DT	Chicken heart with dummy tumor	21	-

(d)

Tissue No.	Soft materials	*h* (mm)	*x*×*y* (mm)
PSR1	PDMS#1 with shallow inclusions	3	9×12
PSR2	PDMS#2 with median inclusions	3	8×14
PSR3	PDMS#3 with deep inclusions	3	8×11

samples (Young's modulus, 170 ± 70 kPa [84]) were embedded with silicone rubbers (Smooth-on, Inc.) for achieving different elasticity. Different colors represented different types of silicone rubbers. PDMS#1 was embedded at a shallow depth with two silicone rubbers (Mold Max®30, pink, Young's Modulus, 758kPa) and two silicone rubbers (Mold Star®30, blue, Young's Modulus, 662kPa). PDMS#2 was embedded at an intermediate depth with four silicone rubbers (Mold Max®40, mint green, Young's Modulus, 1310kPa). PDMS#3 was embedded at a deep depth with three silicone rubbers (Mold Star®30, blue, Young's Modulus, 662kPa). The thicknesses and in-plane dimension of these samples were summarized in Table 4.1 (d).

4.1.2 Experimental Setup and Procedure

4.1.2.1 Measurements on Soft Materials

As illustrated in Figure 3.2(b), the testing parameters of the proposed method includes incremental depth, z_{step}, hold time, t_{hold}, and ramp speed, v_{ramp}. A three-factor-three-level factorial design was applied to the data of the PDMS/silicone rubbers to evaluate the effects of testing parameters. The description of testing parameters was listed in Table 4.2, the independent testing parameters were incremental depth, z_{step} (X_1, 3 levels: 100μm, 200μm, and 300μm), hold time, t_{hold} (X_2, 3 levels: 5s, 15s, and 30s), and ramp speed, v_{ramp} (X_3, 3 levels: 250μm/s, 500μm/s, and 1000μm/s). The low, center and high levels of each parameters were coded as -1, 0, and 1, respectively. The analytical selection of the maximum and minimum ranges for each independent parameter were selected based on the previous measurements. Therefore, in this study three factors were considered. A total of 27 measurements were made on each of the nine PDMS/silicone rubber samples with varied incremental depth, z_{step}, hold time, t_{hold}, and ramp speed, v_{ramp}, respectively. The final compression depth was fixed at 2.4mm for all the measurements, and each measurement was repeated three times. For all measurements, the

alignment between the sensor and tested tissue was kept the same to alleviate the measurement error associated with misalignment. The measured data were the time-dependent sensor deflections at the nine sensing-plates at each compression depth. The average of the sensor deflections at the nine sensing-plates was used to represent the averaged sensor deflection.

Table 4.2 Experimental range and levels of independent testing parameters.

Testing parameters	Symbol	-1	0	1
Incremental depth, z_{step} (μm)	X_1	100	200	300
Hold time, t_{hold} (s)	X_2	5	15	30
Ramp speed, v_{ramp}, (μm/s)	X_3	250	500	1000

4.1.2.2 Measurements on Normal Tissues and PDMS Samples Embedded with Silicone Rubbers

The measurements on all the samples were performed with the same experimental setup and the same 2D sensor. As shown in Figure 4.1, a sample was simply placed on a rigid substrate underneath the sensor. The sensor was fixed on a micropositioner for controlling its displacement. The sensor was aligned at the center of each sample. Afterwards, the pre-defined compression pattern in Figure 3.2(a) was used for pressing the sensor against a sample. The ramp speed of 1mm/s and the hold time of 5s were used for all the samples. For the tissue samples, a step incremental depth of 75μm and a final compression depth of 3mm were used. As to the PDMS samples, the step incremental depth and final compression depth used were 50μm and 2mm, respectively, due to their small thickness. The measured data were the time-varying sensor deflections at the nine sensing-plates at each compression depth. The average of the sensor deflections at the nine sensing-plates was used to represent the averaged sensor deflection. Three trials of the identical measurement were performed on each sample, with a recovery time of 5 minutes between two consecutive trials. Meanwhile, to maintain the hydration of the testing tissue samples, Phosphate Buffered Saline (PBS) solution was sprayed on the testing tissue samples.

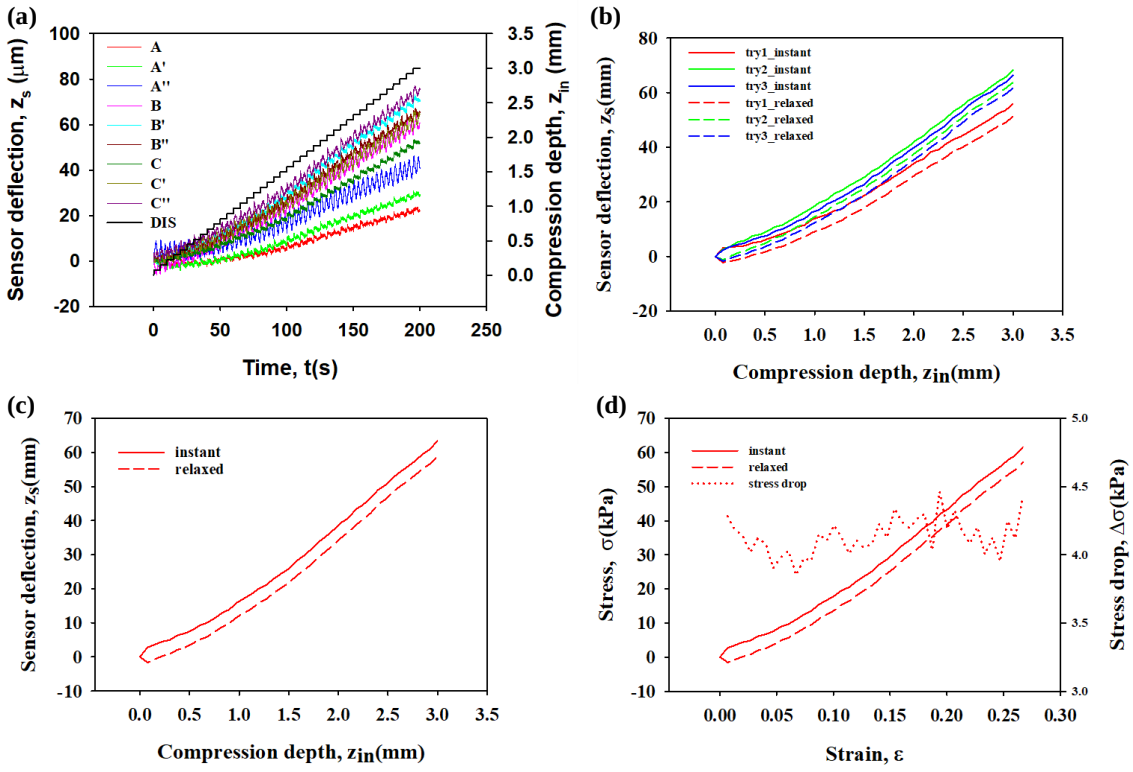

Figure 4.2 Measured results on the bovine shank #1 (a) sensor deflection and compression depth as a function of time from the first trial (b) average instant and relaxed sensor deflection of the nine sensing-plates as a function of the compression depth from three trials (c) average relations of the instant and relaxed sensor deflection versus compression depth of three trials and (d) average instant/relaxed-stress-strain relations and stress drop-strain relation of three trials.

As an example, Figure 4.2 shows the measured results on bovine shank #1. As illustrated in Figure 4.2(a), the originally recorded data from one trial are the sensor deflections of the nine sensing-plates as a function of time, together with the compression depth input. The originally recorded data of three trials are converted to the averaged instant and relaxed sensor deflections as a function of the compression depth, as shown in Figure 4.2(b). Note that the result of the first trial is very different from the results of the two following trials, indicating that a tissue in vitro loses capability of full recovery and thus may exhibit a viscoelastic deviation from its *in vivo*

condition [46]. Nevertheless, further analysis utilized the average value of the measured data of three trials for minimizing the measurement variability among three trials.

Figure 4.2(c) shows the average instant and relaxed sensor deflections as a function of the compression depth of three trials. According to Equation 3.10, the instant elasticity of the tissue can be obtained from the average instant deflection-depth slope in Figure 4.2(c). The average instant and relaxed stress-strain relations of three trials are illustrated in Figure 4.2(d). Meanwhile, the stress drop as a function of strain is also plotted in Figure 4.2(d). Note that the stress drop remains constant with moderate fluctuation over the strain range, indicating that pre-stressing the tissue might not affect its stress relaxation behavior. The tissue loss tangent was estimated based on the average value of the stress drop over the strain range.

Experimental errors from uncertainty in contact point were alleviated by using the measured deflection-depth slopes. Experimental errors from non-perfect normal contact between the sensor and a sample were alleviated by using the averaged sensor deflection from the sensing-plate array [70, 77]. The data in the lower compression range fluctuates significantly due to tissue surface unevenness, while the data in the higher compression range may be subjected to nonlinear behavior. Therefore, only the data in the middle compression range are used for estimating the instant elasticity and loss tangent of the samples. It should be noted that the strain range of each testing tissue sample is selected to ensure a good quality of fitness. Table 4.5 summarized the strain range, slope, $\hat{z}$, and goodness of fit (R^2).

4.1.3 Statistical Analysis

To reveal significant differences of mechanical properties among the measured tissues and their dependencies on the three testing parameters, we statistically evaluated the experimental data on the three groups of commercial available PDMS/silicone rubber samples

(10mm PDMS, 6mm PDMS and silicone rubbers, respectively). First, comparison between possible tissue pairs in the measured instant elasticity and loss tangent was performed using a Student's t-test. All the measured results were displayed as mean values with standard deviations noted by error bar. Next, to determine the significant main effects and interaction effects of testing parameters on the two mechanical properties, instant elasticity and loss tangent, the measured results of the PDMS/silicone rubbers were analyzed using 3-factor ANOVA (n=3). All statistical analysis was performed by using the Statistics and Machine Learning Toolbox in Matlab R2017b (The MathWorks, Inc. Natick, Massachusetts, United States). For all tests a statistical significance is assumed for a *p*-value less than 0.01.

4.2 Results

4.2.1 Measured Results of Soft Materials

In this section, the measured results on three groups of PDMS/silicone rubber samples (10mm PDMS, 6mm PDMS and silicone rubbers) were presented. First, the results of comparative statistical analysis performed on PDMS/silicone rubber samples with respect to the two mechanical properties, instant elasticity and loss tangent were illustrated. Next, individual effects and interaction effects of the three testing parameters on instant elasticity and loss tangent, respectively, were presented.

4.2.1.1 Method Validation: Comparisons of the Measured Mechanical Properties

As shown in Figure 4.3(a), there were significant differences in the instant elasticity, $E_{instant}$, among groups of PDMS and silicone rubber samples, as denoted by the asterisks. For the 10mm PDMS (620.89±9.24 vs 440.90±14.07 vs 290.75 ± 3.17), 6mm PDMS (576.95 ± 17.49 vs 459.37 ±32.22 vs 293.90 ± 7.05) and silicone rubbers (665.06 ± 177.00 vs 296.04 ± 11.30 vs 219.26 ± 6.46). Values of instant elasticity were higher in 1:10 PDMS than in the 1:20 PDMS,

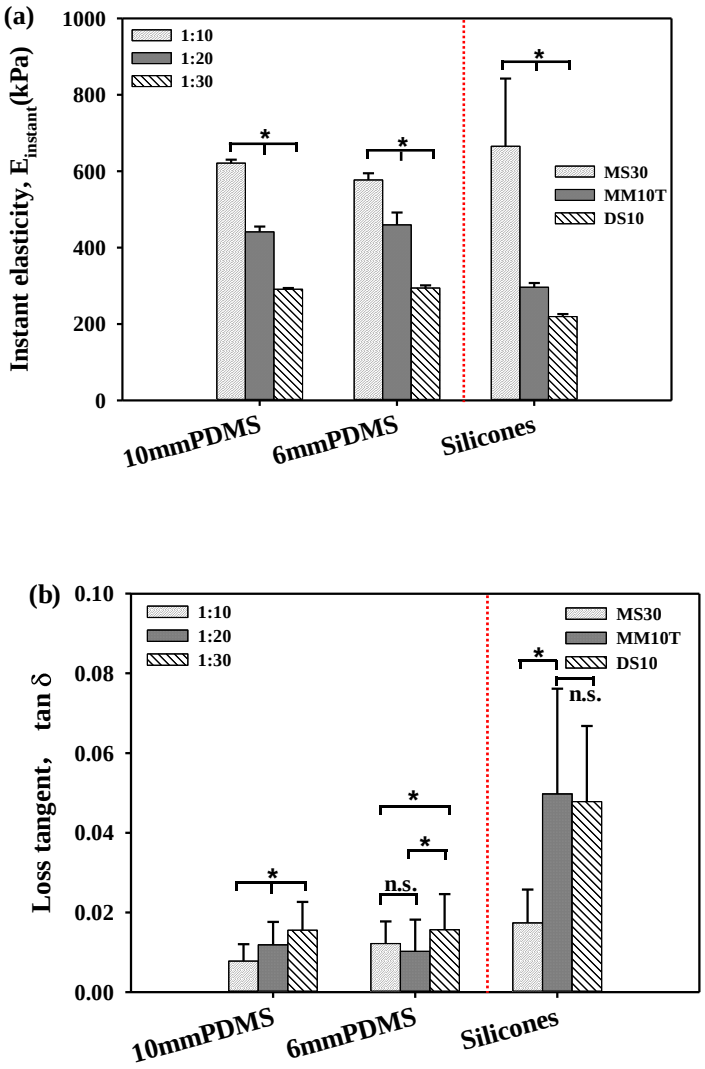

Figure 4.3 Comparison among the tissue samples with respect to the measured mechanical properties. Bar plot of (a) instant elasticity, $E_{instant}$, and (b) loss tangent, tan δ within the groups of PDMS/silicone rubbers. Values were expressed in means and standard deviations. Asterisks (*p<0.01) denote statistically significant differences from the Student's t-tests.

while 1:30 PDMS showed a lower instant elasticity than the 1:20 PDMS for both the 10mm PDMS and 6mm PDMS samples (p<0.01). Moreover, value of instant elasticity of MS30 was found to be the highest among the three silicone rubbers, and DS10 revealed the lowest value in instant elasticity (p<0.01). Figure 4.5(a) compares the elasticity and viscoelasticity among the

PDMS/silicones, respectively. In terms of instant elasticity, 1:10>1:20:>1:30, and MS30>MM10T>DS10. However, the loss tangent of 1:30 was higher than 1:10 and1:20, and DS10>MM10>MS30. This implied viscous behavior was primary for samples with low instant elasticity. On the other hand, elastic behavior was predominantly for samples with higher instant elasticity (1:10 PDMS and MS30). These observations on the PDMS and silicone rubbers were consistent with the results that has been reported in literatures [83-88].

Instead, as illustrated in Figure 4.3(b), with respect to viscoelasticity, there was statistically significant difference among the three 10mm PDMS samples (p<0.01). According the measured results on the three 10mm PDMS samples, 1:30 PDMS exhibited higher loss tangent than either 1:10 or 1:20 PDMS (p<0.01), while no significant difference was found between 1:10 and 1:20 PDMS samples of the 6mm PDMS samples. There were significant differences in the loss tangent of the three silicone rubber samples, as denoted by the asterisks (p<0.01). The results showed that loss tangent of MS30 was significant lower than MM10T and DS10, and no significant difference was found between MM10T and DS10. The measured results indicated that the measured instant elasticity may serve as a better mechanical property for distinguishing these PDMS and silicone rubbers compared with the measured loss tangent.

4.2.1.2 Influence of Testing Parameters on the Measured Mechanical Properties

Table 4.3(a) shows that incremental depth showed a lower p-value compared with hold time and ramp speed, suggesting that incremental depth has strongly affected the instant elasticity and loss tangent of the tested samples except for the instant elasticity of the 10mm 1:10 PDMS and 1:20 PDMS, and the 6mm 1:10 PDMS. Table 4.3(a) also depicts that hold time affected the loss tangent significantly except for the 10mm 1:10 PDMS and 1:20 PDMS, the 6mm 1:20 PDMS, and the MS30. However, ramp speed only exhibited a significant effect on the

loss tangent on 10mm 1:30 PDMS. As shown in Table 4.3(b), among the testing parameters interactions, the interaction effect of the z_{step}*t_{hold} (incremental depth and hold time) exhibited a significant effect on the instant elasticity of 6mm 1:20 PMDS and DS10, and the loss tangent of 6mm 1:30 PDMS. While the z_{step}*v_{ramp} (incremental depth and ramp speed) showed significant effects on the loss tangent of the 10mm and 6mm 1:30 PDMS. In addition, the interaction effects of t_{hold}*v_{ramp} (hold time and ramp speed) were not significant on the mechanical properties of the testing samples except for the instant elasticity of 1:30.

Table 4.3 Analysis of variance of the two mechanical properties, instant elasticity, and viscoelasticity of the measured PDMS and silicone rubbers in response to variable testing parameters. (a) individual effects, and (b) interaction effects. Shaded cells highlight *p*-values less than 0.01 indicates significant effects.

(a)

Tissue Samples	Mechanical Properties	Individual Effects		
		z_{step}	t_{hold}	v_{ramp}
1:10_10	$E_{instant}$	0.38	0.89	0.09
	tan δ	**<0.01**	0.03	0.96
1:20_10	$E_{instant}$	0.02	0.64	0.21
	tan δ	**<0.01**	0.03	0.66
1:30_10	$E_{instant}$	**<0.01**	**<0.01**	0.21
	tan δ	**<0.01**	**<0.01**	**<0.01**
1:10_6	$E_{instant}$	0.02	0.03	0.14
	tan δ	**<0.01**	**<0.01**	0.02
1:20_6	$E_{instant}$	**<0.01**	0.11	0.46
	tan δ	**<0.01**	0.02	0.70
1:30_6	$E_{instant}$	**<0.01**	0.90	0.13
	tan δ	**<0.01**	**<0.01**	0.08
MS30	$E_{instant}$	**<0.01**	0.49	0.99
	tan δ	**<0.01**	0.04	0.69
MM10T	$E_{instant}$	**<0.01**	**<0.01**	0.02
	tan δ	**<0.01**	**<0.01**	0.23
DS10	$E_{instant}$	**<0.01**	0.67	0.55
	tan δ	**<0.01**	**<0.01**	0.01

(b)

Tissue Samples	Mechanical Properties	Interaction Effects		
		z_{step}*t_{hold}	z_{step}*v_{ramp}	t_{hold}*v_{ramp}
1:10_10	$E_{instant}$	0.74	0.30	0.27
	tan δ	0.05	0.24	0.45
1:20_10	$E_{instant}$	0.18	0.59	0.53
	tan δ	0.27	0.66	0.84
1:30_10	$E_{instant}$	0.43	0.12	**<0.01**
	tan δ	0.07	**<0.01**	0.11
1:10_6	$E_{instant}$	0.14	0.04	0.11
	tan δ	0.13	0.43	0.12
1:20_6	$E_{instant}$	**<0.01**	0.41	0.43
	tan δ	0.04	0.75	0.47
1:30_6	$E_{instant}$	0.03	0.17	0.34
	tan δ	**<0.01**	**<0.01**	0.66
MS30	$E_{instant}$	0.20	0.55	0.90
	tan δ	0.41	0.98	0.74
MM10T	$E_{instant}$	0.14	0.73	0.13
	tan δ	0.07	0.20	0.34
DS10	$E_{instant}$	**<0.01**	0.20	0.28
	tan δ	0.59	0.64	0.50

These results implied that there was a significant dependency of the measured elasticity and viscoelasticity on the testing parameters, especially the incremental depth and hold time. The testing parameters showed a significant effect on the measured results for the sample with a lower elasticity, such as the 1:30 PDMS. These observations indicated that samples measured using the same testing parameters were comparable via their elasticity and viscoelasticity

4.2.2 Measured Results of Normal Tissues

Figure 4.4 illustrates the measured instant and relaxed deflection-compression depth slopes, their corresponding instant and relaxed stress-strain relations and stress-drop-strain relations of the soft porcine/bovine tissues. Table 4.4(b) summarizes the measured results of the normal tissues. As shown in Figure 4.4, the porcine/bovine tissues were paired together for better comparison, based on their measured tissue stiffness and thickness.

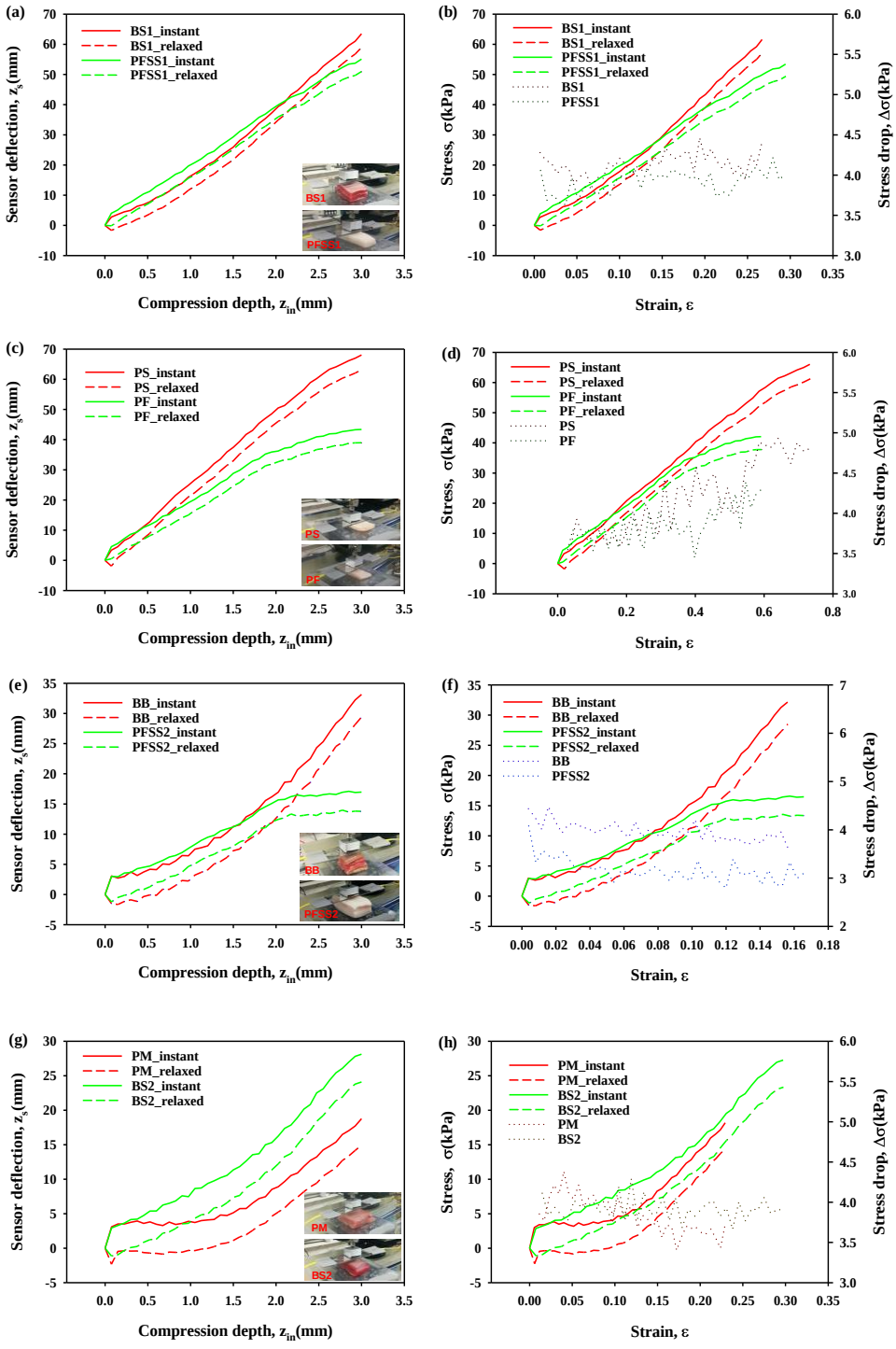

Figure 4.4 Measured instant and relaxed sensor deflection-compression depth relations, corresponding instant and relaxed stress-strain relations and stress drop-strain relations of the tested soft animal tissues.

As to the porcine/bovine tissues, the measured tissue stiffness range and instant tissue elasticity range are 3N/m-9N/m and 47kPa-161kPa, respectively, and the measured loss tangent range is 0.16~2.04. Figures 4.4(a) and 4.4(b) show the measured results on the 11mm-thick bovine shank #1 (BS1) and the 10mm-thick porcine fat-skin stack #1 (PFSS1). Their measured deflection-depth slopes are both about 0.0185. According to Equation 3.8, these similar measured deflection-depth slopes translate to similar measured tissue stiffness of ~9N/m. However, the bovine shank #1 is thicker than the porcine fat-skin stack #1, and thus registers a higher instant elasticity than the porcine fat-skin stack #1, based on Equation 3.10. This can be clearly observed in Figures 4.4(a) and 4.4(b). In Figure 4.4(a), the two tissues register similar measured deflection-depth slopes, which translate to similar tissue stiffness. In Figure 4.4(b), their stress-strain relations reveal that the bovine shank #1 has a higher instant elasticity than the porcine fat-skin stack #1.

Figures 4.4(c) and 4.4(d) show the measured results on the 4mm-thick porcine skin (PS), and the 5mm-thick porcine fat (PF). The measured deflection-depth slopes are about 0.024 and 0.017 for the porcine skin and the porcine fat, respectively. Therefore, the extracted tissue stiffness is 12N/m and 8.4N/m for the porcine skin and the porcine fat, respectively. Since the porcine skin is 20% thinner than the porcine fat, their large difference in tissue stiffness does not translate to a large difference in their instant elasticity. The instant elasticity of the porcine skin is 77.9kPa, which is about 11kPa higher than the porcine fat. Since the thickness of the two tissues is lower than 6mm, their genuine instant elasticity is expected to be lower than these values.

The measured results on the 19mm-thick bovine brisket (BB) and the 18mm-thick porcine fat-skin stack #2 (PFSS2), are illustrated in Figures 4.4(e) and 4.4(f). Their measured

deflection-depth slopes are about 0.007, which is much smaller than their counterparts of the four tissues in Figures 4.4(a)-4.4(d). This indicates that the sensor deflection is very small in the whole compression range and thus carries a large amount of measurement errors. As shown in these two figures, the lower range of the data fluctuates dramatically, as compared with the data in Figures 4.4(a)-4.4(d). The low measured deflection-depth slopes translate to low tissue stiffness of ~3.5N/m for both tissues. Consequently, the instant elasticity of the two tissues is about ~100kPa. Note that the slight difference of ~2kPa in instant elasticity between the two tissues is not reliable, due to measurement errors.

Figures 4.4(g) and 4.4(h) show the measured results on the 13mm-thick porcine muscle (PM) and the 10mm-thick bovine shank #2 (BS2). The measured deflection-depth slopes are about 0.009 and 0.006 for the porcine muscle and the bovine shank #2, respectively. These slopes are close to those for the bovine brisket and the porcine fat-skin stack #2. As such, these results also carry large measurement errors. The measured tissue stiffness becomes 4.44N/m and 2.92N/m for the porcine muscle and the bovine shank #2, respectively. Consequently, the measured instant elasticity is ~92kPa and ~47kPa for the porcine muscle and the bovine shank #2.

As shown in Figure 4.4, the stress drop of the tissue samples remains constant with moderate fluctuation over the strain range. The value of the stress drop varies slightly among the tissue samples and falls into a narrow range of 3kPa-5kPa. However, other than the stress drop, the loss tangent is also related to the instant elasticity and the thickness of a tissue. Thus, the loss tangent of the soft tissues varied from 0.18 to 2.04, as shown in Table 4.4.

Figure 4.5(b) compares the instant elasticity and loss tangent among the porcine/bovine samples, respectively. Note that the instant elasticity of the samples is 80% of the value calculated using Equation 3.10. The measured instant elasticity and loss tangent show no

correlation with the tissue thickness. Although the 13mm-thick porcine muscle (PM) and the 10mm-thick bovine shank #2 (BS2) have similar thickness to the 11mm-thick bovine shank #1 (BS1) and the 10mm-thick porcine fat-skin stack #1 (PFSS1), their measured instant tissue

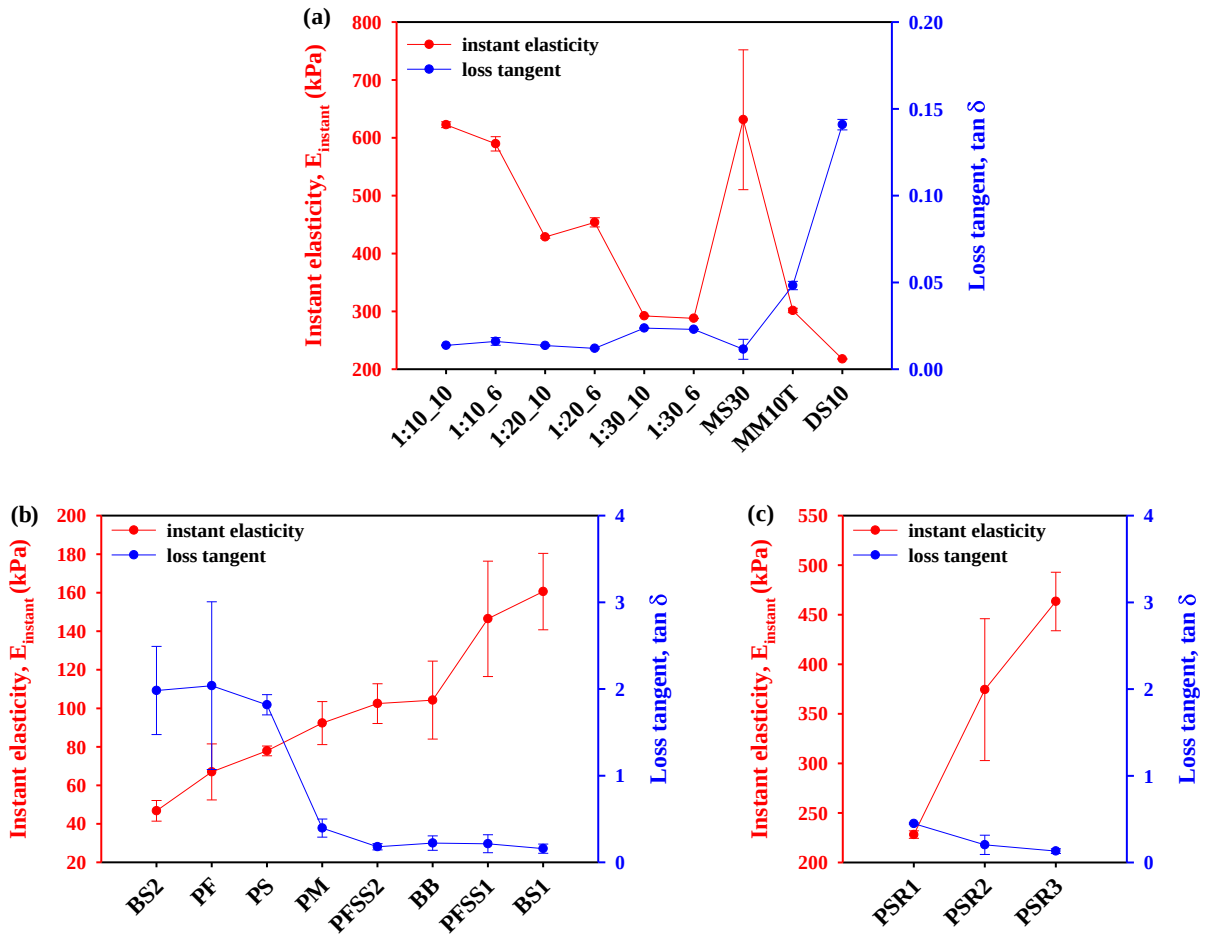

Figure 4.5 Comparison of the measured instant elasticity and loss tangent (average value and standard deviation) measured using comparable testing parameters among (a) PDMS samples and silicone rubbers (z_{step}=100μm, t_{hold}=5s, and v_{ramp}=1000μm/s), and (b) porcine/bovine tissues (z_{step}=75μm, t_{hold}=5s, and v_{ramp}=1000μm/s), and (c) PDMS samples with embedded silicone inclusions (z_{step}=50μm, t_{hold}=5s, and v_{ramp}=1000μm/s).

Table 4.4 Comparison of the key parameters and measured mechanical properties among (a) the PDMS samples and silicone rubbers, (b) the soft tissues, and (c) the PDMS samples with embedded silicone rubbers.

(a)

	h (mm)	$k_{instant}$ (N/m)	$E_{instant}$ (kPa)	tan δ
1:10_10	10	31.13	622.63±5.05	0.014±0.0002
1:10_6	6	49.14	589.67±12.41	0.016±0.002
1:20_10	10	21.43	428.58±2.11	0.014±0.0005
1:20_6	6	37.83	453.93±7.88	0.012±0.0003
1:30_10	10	14.61	292.15±0.77	0.023±0.0002
1:30_6	6	24.00	287.95±0.42	0.023±0.0001
MS30	4	74.55	631.28±120.76	0.012±0.006
MM10T	4	34.54	301.80±3.09	0.048±0.002
DS10	6	17.14	217.71±0.94	0.141±0.003

(b)

	h (mm)	$k_{instant}$ (N/m)	$E_{instant}$ (kPa)	tan δ
BS2	10	2.92	46.78±5.38	1.983±0.508
PF	5	8.37	66.95±14.54	2.039±0.967
PS	4	12.17	77.90±2.54	1.819±0.117
PM	13	4.44	92.33±11.20	0.396±0.105
PFSS2	18	3.56	102.45±10.31	0.180±0.035
BB	19	3.43	104.26±20.23	0.223±0.083
PFSS1	10	9.15	146.46±29.94	0.215±0.104
BS1	11	9.12	160.58±19.84	0.159±0.053

(c)

	h (mm)	$k_{instant}$ (N/m)	$E_{instant}$ (kPa)	tan δ
PSR1	3	47.55	228.24±3.77	0.450±0.007
PSR2	3	78.02	374.50±71.64	0.204±0.111
PSR3	3	96.56	463.48±29.52	0.132±0.026

elasticity and loss tangent are completely different, indicating that the SCR testing method is immune to tissue thickness. Both the elasticity and the loss tangent differentiated the porcine fat (PF) and the porcine skin (PS). Although the bovine brisket and the porcine fat-skin stack #2 (PFSS2) cannot be reliably differentiated via their instant elasticity, the difference in loss tangent

differentiated these two tissues. Thus, both tissue properties are needed for reliably differentiating soft tissues via their mechanical behavior.

As shown in Figure 4.5(b), bovine brisket (BB) exhibits a higher instant elasticity and a lower loss tangent than bovine shank #2 (BS2). As can be seen in Figure 4.1, the biological structure of these two tissues is quite different, since they are obtained from different locations. The bovine shank #1 (BS1) and the bovine shank #2 (BS2) of similar thickness were obtained from two different locations of the same original whole chunk. However, the bovine shank #1 (BS1) has a white layer in it, which may explain the significant difference in the instant elasticity and loss tangent between these two tissues. The white layer renders the bovine shank #1 (BS) to be stiffer and less viscous.

The five porcine tissue samples were from the same original chunk. The 18mm-thick porcine fat-skin stack #2 contains a thicker fat layer than the 10mm-thick porcine fat-skin stack #1. Thus, the porcine fat-skin stack #2 (PFSS2) exhibits a lower instant elasticity and a lower loss tangent than the porcine fat-skin stack #1 (PFSS1). The porcine fat was obtained from the fat next to the porcine skin. The porcine skin is a higher elasticity and lower viscoelasticity than the porcine fat. The porcine fat-skin stack #1 is approximately equivalent to a combination of the porcine skin (PS) and porcine fat (PF). This combination exhibits a much higher instant elasticity than the fat and the skin themselves, indicating that the interface between the fat and the skin may play an important role in determining the elasticity of the fat-skin stack. Meanwhile, this interface affects the viscoelasticity of the fat-skin stack, in the sense that the stack registers a lower value of loss tangent that the skin and the fat. The porcine muscle showed a higher elasticity than the porcine fat and skin, but a lower viscoelasticity than the fat and the skin. These

observations were comparable with the published values [89]. Overall, the bovine and porcine muscle tissues exhibit lower value of loss tangent, as compared with the porcine fat and skin.

We qualitatively compare the measured results among the eight tissues. All the bovine and porcine muscles exhibit a fast stress increase, as the strain goes up. Conversely, all the porcine fat, skin and fat-skin stacks reveal a slow stress increase as the strain goes up. This may indicate that the biological compositions in porcine fat and porcine skin share some commonalities; bovine and porcine muscles also share some common biological features; and there is a salient difference in biological compositions or structures between muscle and fat/skin.

4.2.3 Measured Results of PDMS Samples with Embedded Dummy Tumors

The measured results on the three PDMS samples with embedded silicone inclusions (PSR) were illustrated in Figures 4.6(a) and 4.6(b). These heterogeneous samples are treated as homogeneous materials for comparison among the animal tissue samples. Because of the inclusion of the hard silicone rubbers into these soft PDMS (1:30) samples, these samples are much stiffer than the porcine/bovine tissues. Therefore, their measured deflection-depth slopes and stiffness are much higher than their counterparts of the tissue samples. Meanwhile, the stress drop of the PSR samples is a little higher than the tissue samples. These samples have a smaller in-plane dimension than the in-plane dimension of the sensor and meanwhile are all 3mm thick. Based on the finite element analysis, the small in-plane dimension and the 3mm thickness cause an underestimate and an overestimate of the sample stiffness and the instant elasticity, respectively. Taken together, the measured stiffness and the instant elasticity of these PSR samples might be consistent with those values of the porcine/bovine tissues.

In terms of instant elasticity, the three PSR samples follow the order: PSR1 < PSR2 < PSR3. Based on the depth and types of silicone rubbers embedded in these samples, we can

conclude that the Young's modulus of the silicone rubbers does not influence the measured results as much as their embedded depth.

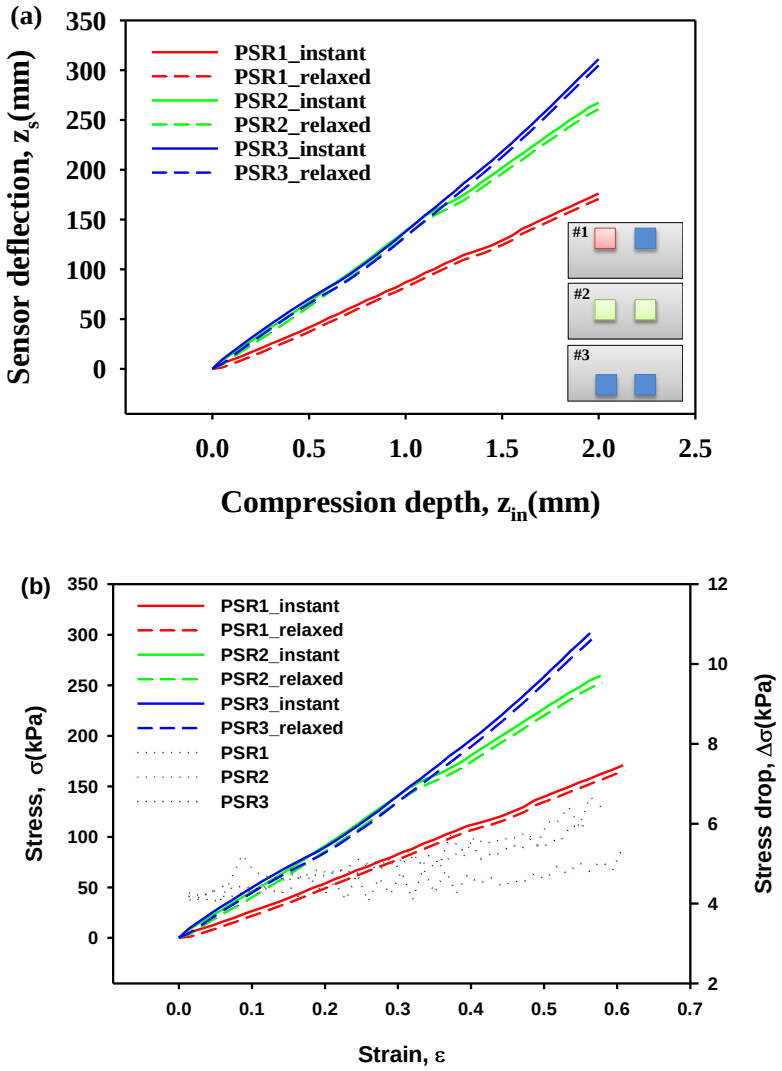

Figure 4.6 Instant and relaxed sensor deflection-compression depth relations, and (b) instant and relaxed stress-strain relations, relationship between stress drop and strain of the measured PDMS samples with embedded silicone rubbers (PSR).

Although the Young's modulus of the deep-embedded rubbers in PSR3 is much lower than that of intermediate-embedded rubbers in PSR2, a deep depth yields a higher instant elasticity than a shallow depth. As pointed out earlier, the rigid substrate increases the measured

tissue stiffness by amplifying the force at the sensor-sample interface. The influence of the rigid substrate is transmitted to the sensor-sample interface via the material between the rigid substrate and the sensor-sample interface. Thus, the deep-embedded rubbers close to the rigid substrate further amplify the force at the sensor-sample interface. In other words, the material near the bottom surface of a PSR sample plays a critical role in determining its measured properties. As shown in Table 4.4(c), the loss tangent of the PDMS samples follows the order of the depth of the embedded rubbers: PSR1> PSR2> PSR3.

Table 4.5 Comparison of the measurement errors and the standard deviations of the instant deflection-depth slope of (a) PDMS samples, (b) silicone rubbers and PDMS samples with embedded silicones, (c) and (d) porcine and bovine tissues.

(a)

		1:10_10	1:10_6	1:20_10	1:20_6	1:30_10	1:30_6
Trial#1	$\hat{z}_1$	0.0478	0.0718	0.0340	0.0591	0.0233	0.0377
	$\varepsilon_{\hat{z}_1}$	0.0004	0.0011	0.0002	0.0010	0.0002	0.0001
	$\%\varepsilon_{\hat{z}_1}$	0.76%	1.58%	0.72%	1.62%	0.69%	0.36%
	R^2	0.9994	0.9995	0.9996	0.9947	0.9999	1.0000
Trial#2	$\hat{z}_2$	0.0483	0.0746	0.0336	0.0573	0.0233	0.0376
	$\varepsilon_{\hat{z}_2}$	0.0003	0.0013	0.0002	0.0007	0.0002	0.0001
	$\%\varepsilon_{\hat{z}_2}$	0.72%	1.80%	0.63%	1.23%	0.66%	0.36%
	R^2	0.9999	0.9998	0.9999	0.9972	0.9996	0.9999
Trial#3	$\hat{z}_3$	0.0485	0.0740	0.0338	0.0578	0.0234	0.0377
	$\varepsilon_{\hat{z}_3}$	0.0003	0.0012	0.0002	0.0008	0.0002	0.0001
	$\%\varepsilon_{\hat{z}_3}$	0.63%	1.63%	0.66%	1.37%	0.69%	0.39%
	R^2	0.9999	0.9998	0.9999	0.9963	0.9998	0.9999
Average	$\bar{\hat{z}}$	0.0482	0.0734	0.0338	0.0580	0.0233	0.0377
Strain range		(0.01,0.23)	(0.02,0.37)	(0.01,0.23)	(0.02,0.38)	(0.01,0.23)	(0.02,0.38)
Average error	$\bar{\varepsilon}_{\hat{z}}$	0.0003	0.0012	0.0002	0.0008	0.0002	0.0001
	$\%\bar{\varepsilon}_{\hat{z}}$	0.70%	1.67%	0.67%	1.40%	0.68%	0.37%
Standard deviation	$s_{\hat{z}}$	0.0003	0.0015	0.0002	0.0009	0.0001	0.0001
	$\%s_{\hat{z}}$	0.70%	2.00%	0.49%	1.63%	0.25%	0.15%

(b)

		MS30	MM10T	DS10	PSR1	PSR2	PSR3
Trial#1	$\hat{z}_1$	0.0861	0.0538	0.0272	0.0906	0.1114	0.1557
	$\varepsilon_{\hat{z}_1}$	0.0012	0.0008	0.0004	0.0004	0.0007	0.0009
	$\%\varepsilon_{\hat{z}_1}$	1.36%	1.52%	1.62%	0.45%	0.63%	0.56%
	R^2	0.9992	0.9981	0.9942	0.9996	0.9992	0.9992
Trial#2	$\hat{z}_2$	0.1081	0.0526	0.0271	0.0879	0.1505	0.1713
	$\varepsilon_{\hat{z}_2}$	0.0016	0.0008	0.0004	0.0004	0.0012	0.0018
	$\%\varepsilon_{\hat{z}_2}$	1.49%	1.60%	1.63%	0.48%	0.81%	1.08%
	R^2	0.9997	0.9981	0.9945	0.9995	0.9987	0.9970
Trial#3	$\hat{z}_3$	0.1184	0.5339	0.0273	0.0893	0.1526	0.1709
	$\varepsilon_{\hat{z}_3}$	0.0019	0.0008	0.0005	0.0004	0.0009	0.0019
	$\%\varepsilon_{\hat{z}_3}$	1.60%	1.55%	1.96%	0.40%	0.58%	1.09%
	R^2	0.9992	0.9980	0.9917	0.9997	0.9993	0.9969
Average	$\bar{\hat{z}}$	0.1042	0.0533	0.0272	0.0893	0.1382	0.1660
Strain range		(0.02,0.51)	(0.02,0.52)	(0.02,0.38)	(0.06,0.40)	(0.03,0.33)	(0.19,0.56)
Average error	$\bar{\varepsilon}_{\hat{z}}$	0.0016	0.0008	0.0005	0.0004	0.0009	0.0015
	$\%\bar{\varepsilon}_{\hat{z}}$	1.48%	1.55%	1.74%	0.44%	0.67%	0.91%
Standard deviation	$s_{\hat{z}}$	0.0165	0.0006	0.0001	0.0013	0.0232	0.0089
	$\%s_{\hat{z}}$	15.83%	1.21%	0.43%	0.04%	16.79%	5.35%

(c)

		BS1	PFSS1	PS	PF
Trial#1	$\hat{z}_1$	0.0160	0.0142	0.0238	0.0129
	$\varepsilon_{\hat{z}_1}$	0.0003	0.0003	0.0004	0.003
	$\%\varepsilon_{\hat{z}_1}$	2.01%	2.25%	1.62%	1.95%
	R^2	0.9948	0.9860	0.9961	0.9909
Trial#2	$\hat{z}_2$	0.0204	0.0202	0.0253	0.0198
	$\varepsilon_{\hat{z}_2}$	0.0003	0.0001	0.0001	0.0001
	$\%\varepsilon_{\hat{z}_2}$	1.47%	0.54%	0.51%	0.68%
	R^2	0.9972	0.9992	0.9996	0.9989
Trial#3	$\hat{z}_3$	0.0190	0.0211	0.0243	0.0182
	$\varepsilon_{\hat{z}_3}$	0.0004	0.0001	0.0002	0.0001
	$\%\varepsilon_{\hat{z}_3}$	1.89%	0.50%	0.93%	0.78%
	R^2	0.9954	0.9993	0.9987	0.9985
Average	$\bar{\hat{z}}$	0.0185	0.0185	0.0245	0.0170
Strain range		(0.04,0.13)	(0.01,0.22)	(0.20,0.49)	(0.01,0.38)
Average error	$\bar{\varepsilon}_{\hat{z}}$	0.0003	0.0001	0.0002	0.0001
	$\%\bar{\varepsilon}_{\hat{z}}$	1.53%	0.70%	0.73%	0.83%
Standard deviation	$s_{\hat{z}}$	0.0022	0.0037	0.0008	0.0036
	$\%s_{\hat{z}}$	12.14%	20.12%	3.18%	21.40%

(d)

		BB	PFSS2	PM	BS2
Trial#1	$\hat{z}_1$	0.0085	0.0081	0.0103	0.0066
	$\varepsilon_{\hat{z}_1}$	0.0003	0.0001	0.0002	0.0001
	$\%\varepsilon_{\hat{z}_1}$	3.19%	1.53%	1.75%	1.77%
	R^2	0.9850	0.9956	0.9939	0.9944
Trial#2	$\hat{z}_2$	0.0067	0.0070	0.0086	0.0062
	$\varepsilon_{\hat{z}_2}$	0.0003	0.0001	0.0002	0.0001
	$\%\varepsilon_{\hat{z}_2}$	4.18%	1.99%	2.84%	1.90%
	R^2	0.9744	0.9925	0.9841	0.9935
Trial#3	$\hat{z}_3$	0.0058	0.0067	0.0083	0.0052
	$\varepsilon_{\hat{z}_3}$	0.0003	0.0002	0.0001	0.0002
	$\%\varepsilon_{\hat{z}_3}$	5.18%	3.21%	1.67%	3.69%
	R^2	0.9613	0.9808	0.9944	0.9761
Average	$\bar{\hat{z}}$	0.0070	0.0073	0.0091	0.0060
Strain range		(0.02,0.08)	(0.03,0.11)	(0.05,0.13)	(0.01,0.16)
Average error	$\bar{\varepsilon}_{\hat{z}}$	0.0002	0.0001	0.0002	0.0001
	$\%\bar{\varepsilon}_{\hat{z}}$	3.52%	1.46%	1.84%	1.88%
Standard deviation	$s_{\hat{z}}$	0.0014	0.0007	0.0011	0.0007
	$\%s_{\hat{z}}$	19.26%	9.99%	12.02%	11.44%

It is well known that misalignment between a sensor array and a tissue region introduces measurement errors and poses the risk of yielding distorted mechanical properties of the tissue region. Such measurement errors in the SCR testing method have been alleviated with a correction mechanism [77]. Ideally, the measured data at the low compression depth (<1mm) reveal elastic behavior of a tissue. However, these tissues do not contain a completely flat surface and are even covered with fur and skin. As such, instead of its elastic behavior, these data manifest the surface feature of a tissue and are not utilized for extracting the mechanical properties. In contrast, the effect of the surface feature in the measured data is believed to become trivial at high compression depths (1mm~4mm). Since the final compression depth is comparable to the thickness of the tissues, the measured data at high compression depths reveal

the nonlinear behavior of the tissues. Thus, the measured instant elasticity and relaxation extent represents the strength and viscosity of a tissue in its nonlinear region.

Table 4.5 compares the measurement errors and the standard deviations in the measured instant deflection-depth slope of the twenty soft tissues among three trials. In a measurement, there is an error, $\varepsilon_{\hat{z}}$, in the measured instant deflection-depth slope. Then, the percentage error in the measured instant deflection-depth slope becomes:

$$\%\varepsilon_{\hat{z}} = \frac{\varepsilon_{\hat{z}}}{\hat{z}} \times 100 \tag{4.1}$$

The percentage of standard deviation in the measured instant deflection-depth slope is defined as:

$$\%\mathrm{s}_{\hat{z}} = \frac{s_{\hat{z}}}{\hat{z}} \times 100 \tag{4.2}$$

The measurement errors in the measured deflection-depth slope are consistent among three trails for each tissue sample and well below the percentage of the standard deviation of three trials. As illustrated in Figure 4.2(b), a significant difference in the measured instant deflection-depth slope between the first trial and the following two trails is observed in all the tissues. Therefore, the percentage of standard deviation is well above the measurement errors in the measured deflection-depth slope.

4.3 Discussion

This chapter aims to present a mechanical testing method (SCR) that allows viscoelasticity measurement consistency among soft tissues of different thickness so that soft tissues can be reliably differentiated via their mechanical properties. In this study, PDMS/silicone rubbers, porcine/bovine normal tissues, PDMS sample with inclusions were measured. There are no established standards for calibrating viscoelasticity measurements in soft tissues although precision and consistency can be tested by using comparisons among

independent measurement techniques [63]. Meanwhile, it is unrealistic to compare the measured results with those related data in the literature, due to the significant difference of the measured viscoelasticity reported on the same type of tissue in the literature. For instance, the reported Young's modulus of porcine skin is in the range of 56-111MPa [90], and the reported Young's modulus of human epidermis is in the range of 140-600kPa [91]. The three testing parameters dramatically affect the measured tissue viscoelasticity [46, 63, 92, 93]. Furthermore, arising from the 3D nature of the tissue-equipment interaction, testing equipment and the associated model used for extracting tissue viscoelasticity also greatly influence the measured tissue viscoelasticity. For instance, the plate compression testing and indentation testing on the same gelatin sample yield different estimated viscoelasticity, with the same testing parameters being used [63]. Different compression testing equipment give rise to different measured viscosity on the same sample [45]. Thus, the significant difference in the measured viscoelasticity on the same type of tissue is believed to mainly result from different measurements, rather than the great variability in soft tissue properties themselves.

Evidently, the measured instant elastic modulus and loss tangent are both expected to vary with the three testing parameters and the sensor design. The theoretical model overestimates the genuine elasticity of a tissue. It is expected that this overestimate will vary with the sensor design. Thus, viscoelasticity measurement consistency among soft tissues can be achieved by utilizing the same sensor design to rule out the variation in the actual 3D nature of the tissue-sensor interaction among measurements and utilizing the same testing parameters to rule out the effect of their variation on the measured tissue viscoelasticity

Above all, it is the relative difference in the measured tissue viscoelasticity that holds the key for differentiating soft tissues, instead of their absolute values. The PDMS/silicone

rubber/PSR samples exhibit viscoelastic behavior completely different from the porcine/bovine tissues. As described in Figure 4.5 and Table 4.4, the relative difference in both the instant elastic modulus and the loss tangent is capable of reliably differentiating the measured soft tissues. First, the PDMS/silicone rubber/PSR samples maintain their linear stress-strain relations, as the strain increases. Second, owing to their surface smoothness, their measured data in the lower compression range do not fluctuate as much as those of the tissue samples, indicating that surface unevenness in the tissue samples is the key factor for significant measurement errors in the data in the lower compression range. Lastly, the significant difference in stress-strain relation between the PDMS/silicone rubber samples and the porcine/bovine tissues indicates that PDMS/silicone rubbers may not serve well as substitutes for studying soft biological tissues.

4.4 Conclusion

In this chapter, PDMS/silicone rubbers, porcine/bovine normal tissues, PDMS sample with inclusions, mouse breast tumor tissues, mouse pancreatic tumor tissues were measured by using the SCR testing method for characterizing their mechanical behavior, respectively. The inter-connection among the sensing-plate/transducer array of the 2D sensor allows the sensor to interact with a tissue in a continuous manner so that similar small tilt angles are formed at different sites of a tissue, and thus unify the misalignment errors. Arising from fabrication variation and misalignment performance variation among the array is identified by the original resistance of the sensing-plate stiffness and the initial resistance of the initial transducer height after the sensor is being aligned with a tissue. The effect of the performance variation is removed from their measured results based on the correction mechanism for the sensor stiffness variation and the transducer height variation.

A three-factor-three-level factorial design was applied to the experimental data of PDMS/silicone rubbers enabled evaluation of testing parameters on the mechanical properties. The results suggested that only measured tissue mechanical properties using the same testing parameters were comparable. Next, with the experimental testing parameters being fixed and the same sensor being utilized, a combination of the testing method and these two properties enables achieving consistent measurements of soft tissues.

In summary, the results showed muscle tissues were different from fat/skin tissues in the measured mechanical properties. Furthermore, differences in mechanical properties between muscle tissues and PDMS were also observed. For better differentiation of soft tissues, both the elasticity and viscoelasticity need to be measured.

CHAPTER 5

TUMOR DETECTION BASED ON MEASURED ELASTICITY

This chapter presents the tumor detection based on the elasticity measured using the Stepwise Compression Relaxation (SCR) testing method. To validate the feasibility, *ex vivo* measurements and *in vivo* measurements were conducted on mouse breast and pancreatic tumor tissues, respectively. Details about the sample preparation, experimental setup, experimental procedures, measured results, discussion and conclusion were presented.

5.1 Materials and Methods

5.1.1 Preparation of Mouse Breast and Pancreatic Tumor Tissues

The group of *ex vivo* measurement on orthotopic mouse breast cancer model was established by injection of 10^6 4T1 or 4T1-luc cells in 50uL PBS into the left posterior mammary gland [94]. 4T1-luc cells are generated from 4T-1 cells after transfected with a Luiferase gene (from a firefly) for easy detection of tumors in live animals by IVIS Spectrum *In Vivo* Imaging System (Caliper Life Sciences). 4T1 tumors were observed to grow slightly faster than 4T1-luc tumors in this study, and they both are invasive and spontaneously metastatic cancers. Five breast tumor (BT) tissues were from five individual mice and were illustrated in Figure 5.1, together with their palpated areas. While BT1 and BT2 were from the 4T1 cancer model and were harvested after a 27day growth, the other tumor tissues were from the 4T1-luc cells model and were harvested after a 37day growth. Two growth times were aimed to get tumors of similar sizes. The dark areas in BT3, BT4 and BT5 correspond to necrosis areas, which resulted from tumor fast growth outpacing blood supply. Note that the tumor in each tissue was quite near to the skin and none of the tissues contain bones. Owing to different sizes of tumors in the tissues,

the thickness varies among the five tumor tissues. Thus, the tissue thickness is indicative of the tumor size. Details of the key parameters and their values were presented in Table 5.1(a).

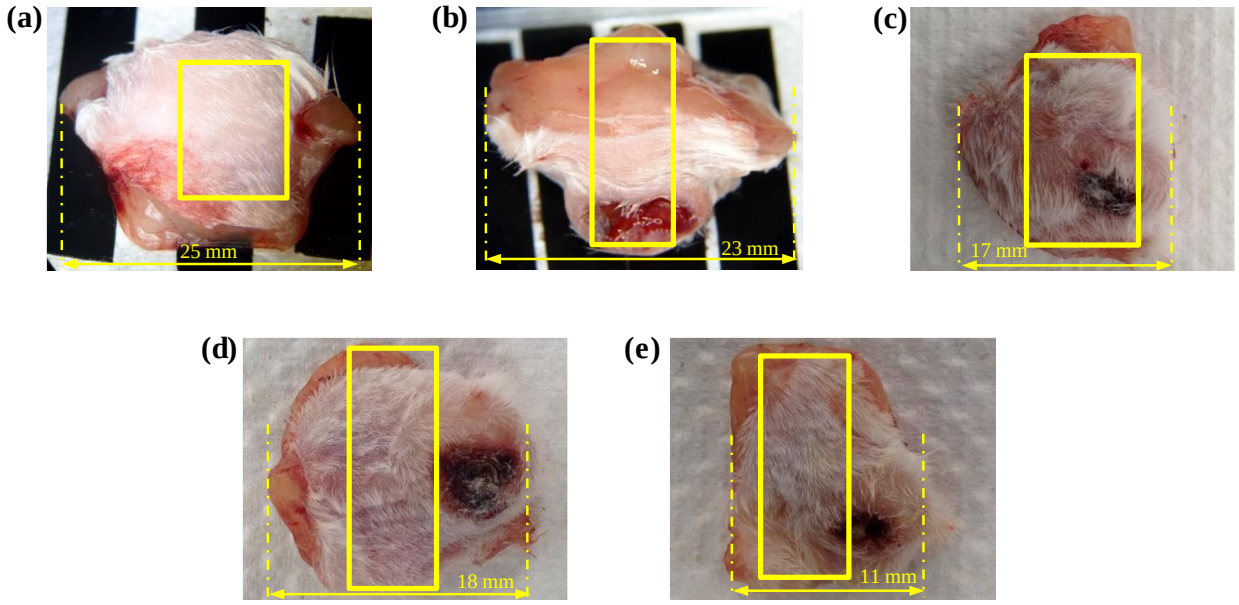

Figure 5.1 Pictures of the breast tumor (BT) tissues and their palpated areas (a) BT1 and palpated area of 9mm×11.25mm (b) BT2 and palpated area of 6mm×15mm (c) BT3 and palpated area of 9mm×15mm (d) BT4 and palpated area of 6mm×26.25mm (e) BT5 and palpated area of 6mm×15mm.

The group of *in vivo* measurement on two mouse pancreatic tumor (PT) tissues were from injection of PAN02 cells on the left flank and were measured after a 7day growth. Afterwards, the two tumors were treated with irreversible electroporation [95] and were measured 27day after treatment. Mice were euthanized during measurement. The experimental protocol was approved by Old Dominion University Institutional Biosafety Committee (IBC) and Institutional Animal Care and Use Committee (IACUC). A red rectangular marker denoted the palpated area in each PT tissue in Figure 5.2. Details of the key parameters and their values were presented in Table 5.1(b).

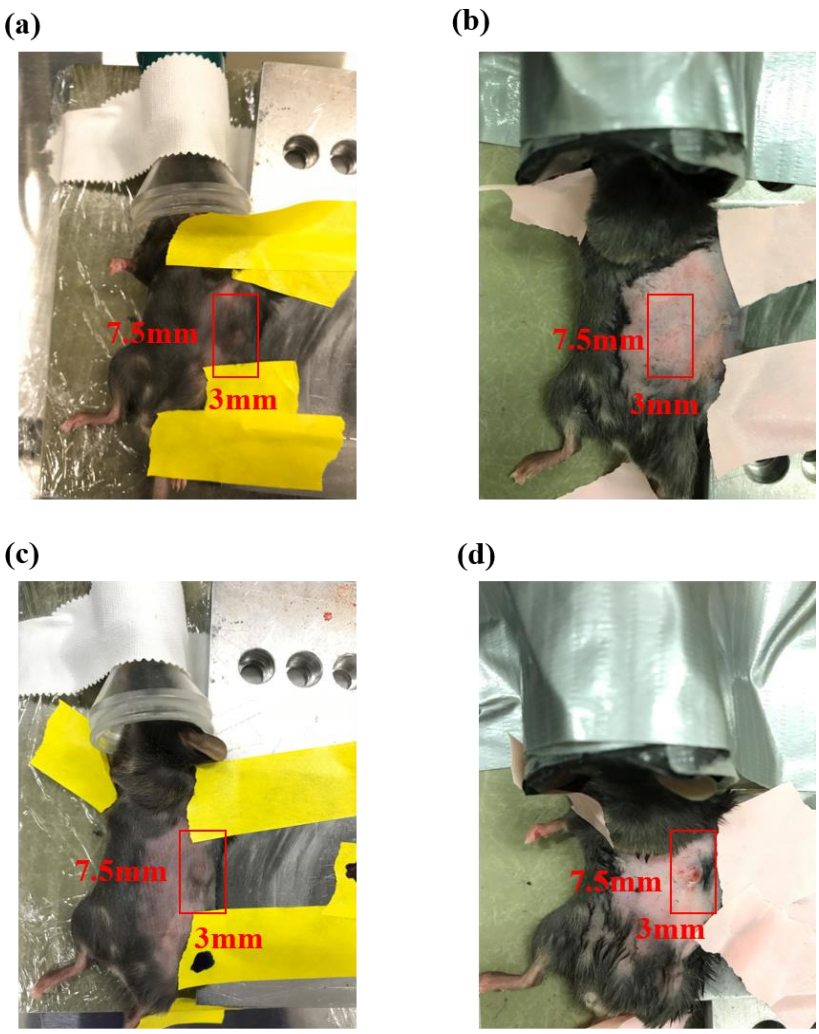

Figure 5.2 Pictures of the pancreatic tumor (PT) tissues and their palpated areas (a) PT1 before treatment and palpated area of 3mm×7.5mm (b) PT1 after treatment and palpated area of 3mm×7.5mm (c) PT2 before treatment and palpated area of 3mm×7.5mm, and (d) PT2 after treatment and palpated area of 3mm×7.5mm.

5.1.2 Experimental Setup and Procedure

5.1.2.1 *Ex Vivo* Measurements on Mouse Breast Tumor Tissues

Figure 5.3 shows pictures of the experimental setup for characterizing the mechanical behavior of a mouse breast tumor tissue. The details about this setup can be found in the literature [70]. The sensor is mounted on a micropositioner. The micropositioner is then utilized

to manually adjust the position of the sensor for aligning its sensing region with a targeted tissue region, and afterwards automatically exert a pre-defined compression pattern, z_{in}, on the tissue region. Figure 5.4(a) illustrates this compression pattern: the sensor is brought down an incremental compression depth of 200μm each time with a ramp-up speed of 200μm/s and a 5s hold-on time until reaching the final compression depth of 4mm. The corresponding instant and relaxed sensor deflection, $z_{s\text{-}instant}$ and $z_{s\text{-}relaxed}$, at the start and end of the 5s hold time at each compression depth, respectively, are acquired by the sensor.

Table 5.1 Two groups of (a) mouse breast tumor tissues (BT1-BT5), and (b) mouse pancreatic tumor tissues (PT1-before, PT2_before, PT1_after, and PT2_after).

(a)

Tissue No.	Harvest days	Cells injected	*h* (mm)
BT1	d27	4T1	9
BT2	d27	4T1	14
BT3	d37	4T1-luc	11
BT4	d37	4T1-luc	9
BT5	d37	4T1-luc	7

(b)

Tissue No.		Days growing/after treatment	Cells injected	*h* (mm)
Before treatment	PT1_before	d7	PAN02	5
	PT2_before	d7	PAN02	6
After treatment	PT1_after	d24	-	2
	PT2_after	d24	-	2

A LabVIEW program is written to implement the palpation and record the data. The originally measured data are the instant sensor deflection, $z_{s\text{-}instant}$, relaxed sensor deflection, $z_{s\text{-}relaxed}$, and compression depth, z_{in}, as a function of time, as shown in Figure 5.4(a). Consequently, the two relations: instant sensor deflection versus compression depth, $z_{s\text{-}instant}$~z_{in}, and relaxed sensor deflection versus compression depth, $z_{s\text{-}relaxed}$~z_{in}, can be obtained, as shown in Figure 5.4(b). The slopes of the $z_{s\text{-}instant}$~z_{in} relation and the $z_{s\text{-}relaxed}$~z_{in} relation give rise to the instant

stiffness, $k_{t\text{-}instant}$, and the relaxed stiffness, $k_{t\text{-}relaxed}$ of a measured tissue site. Covered with fur and skin, the tissue surface is not smooth. Thus, the sensor deflection at low compression depth bears significant amount of errors, and the slopes of the two relations are extracted from the data in a higher compression depth range.

(a)

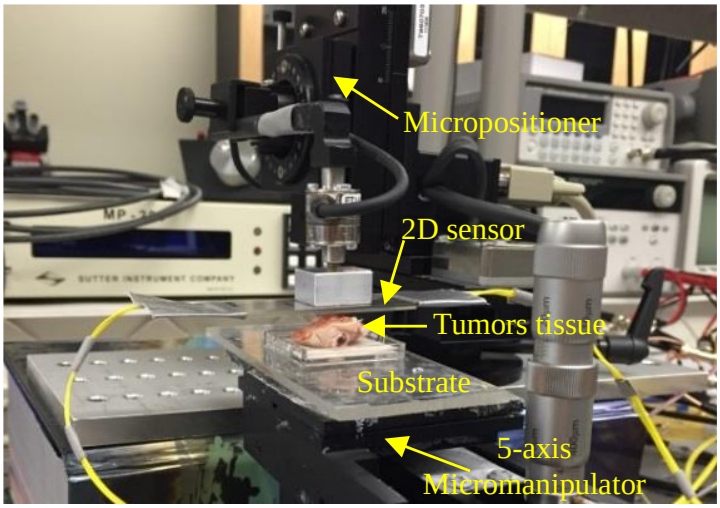

(b)

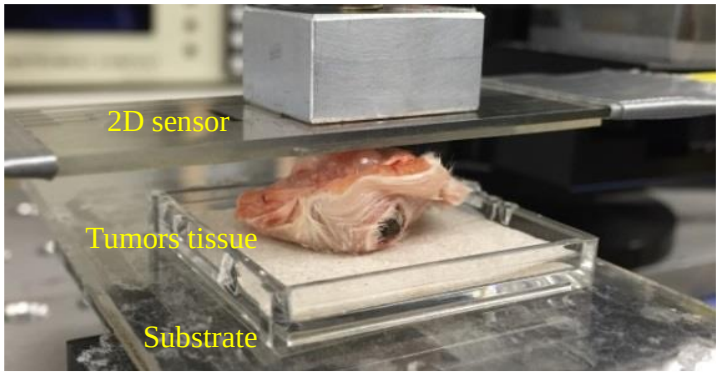

Figure 5.3 Pictures of the experimental setup for characterizing the mechanical behavior of a breast tumor (BT) tissue *ex vivo* (a) the whole setup (b) the 2D sensor being aligned with a tumor tissue.

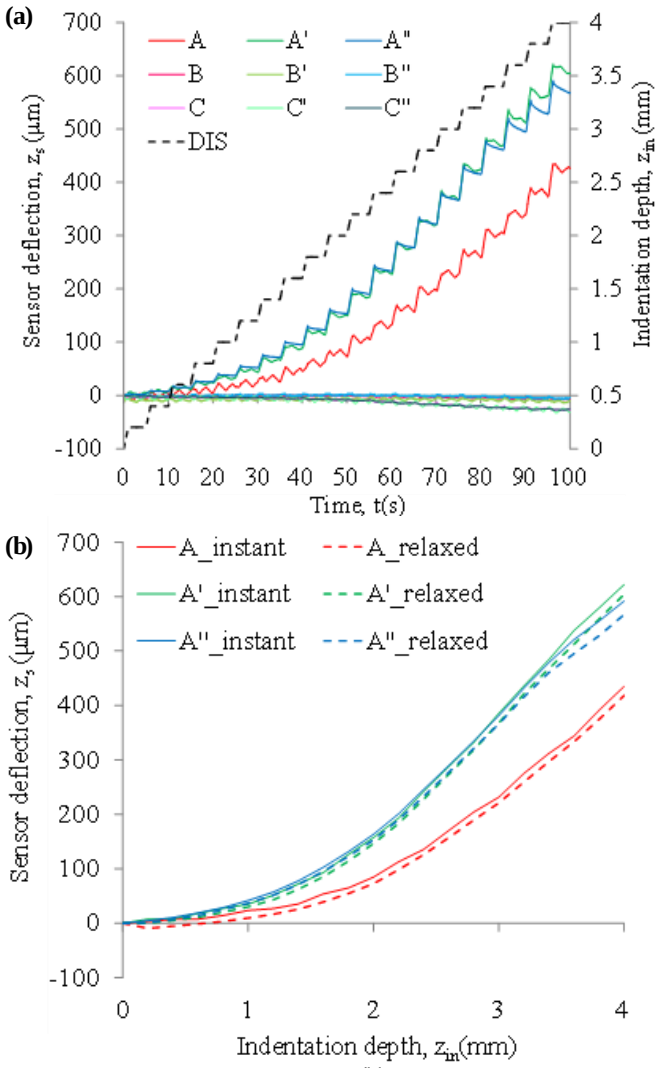

Figure 5.4 Measured data on BT2 (a) originally recorded data: instant and relaxed sensor deflection, z_s, and compression depth as a function of a time, t, and (b) processed data: the instant and relaxed sensor deflection, z_s, as a function of compression depth, z_{in}.

Depending on the measured results of a previously palpated tissue region, the sensor is moved accordingly to map out the location, shape and size of the tumor in a tissue. Since the shape and size of a tumor vary among the tumor tissues, the size of the palpated tissue area varies among them. The same sensor is utilized to palpate the five tumor tissues to avoid the effect of performance variation among individual sensors on the measured results.

5.1.2.2 *In Vivo* Measurements on Mouse Pancreatic Tumor Tissues

Figure 5.5 shows pictures of the experimental setup for *in vivo* measurement of the mechanical behavior of a pancreatic tumor tissue. The 2D sensor was mounted on a micropositioner. The micropositioner is then utilized to manually adjust the position of the 2D sensor for aligning its sensing region with a targeted tissue region, and afterwards automatically exert a pre-defined compression pattern, z_{in}, on the tissue region. Mouse tissues were relatively soft, making them extremely difficult to compress during *in vivo* measurement. Thus, the mouse tissue with an embedded pancreatic tumor was placed on top of a rigid substrate for conducting tissue palpation. The mouse tissue was fixed using paper tape to avoid slippage. Next, similar as the compression pattern shown in Figure 5.4(a), the 2D sensor was brought down an incremental compression depth of 200μm each time with a ramp speed of 200μm/s and a 30s hold time until reaching the final compression depth of 1.2mm. The corresponding instant and relaxed sensor deflection, $z_{s\text{-}instant}$ and $z_{s\text{-}relaxed}$, at the start and end of the 30s hold time at each compression depth, respectively, were measured by the 2D sensor.

A LabVIEW program was written to implement the tissue palpation and collect the data. The raw data were the instant sensor deflection, $z_{s\text{-}instant}$, relaxed sensor deflection, $z_{s\text{-}relaxed}$, and compression depth, z_{in}, as a function of time. Consequently, the two relations: instant sensor deflection versus compression depth, $z_{s\text{-}instant}$~z_{in}, and relaxed sensor deflection versus compression depth, $z_{s\text{-}relaxed}$~z_{in}, can be obtained. The slopes of the $z_{s\text{-}instant}$~z_{in} relation and the $z_{s\text{-}relaxed}$~z_{in} relation give rise to the instant stiffness, $k_{t\text{-}instant}$, and the relaxed stiffness, $k_{t\text{-}relaxed}$ of a measured tissue site. The hair of tissue region with an embedded tumor was removed using Nair hair removal cream (Figures 5.2(b) and 5.2(d)). Mice were euthanized during the operation.

Since the tumor in each PT tissue was only 2~3mm in diameter, only one measurement on each PT tissue was conducted, with the middle row of the transducer array aligned on top of the tumor.

(a)

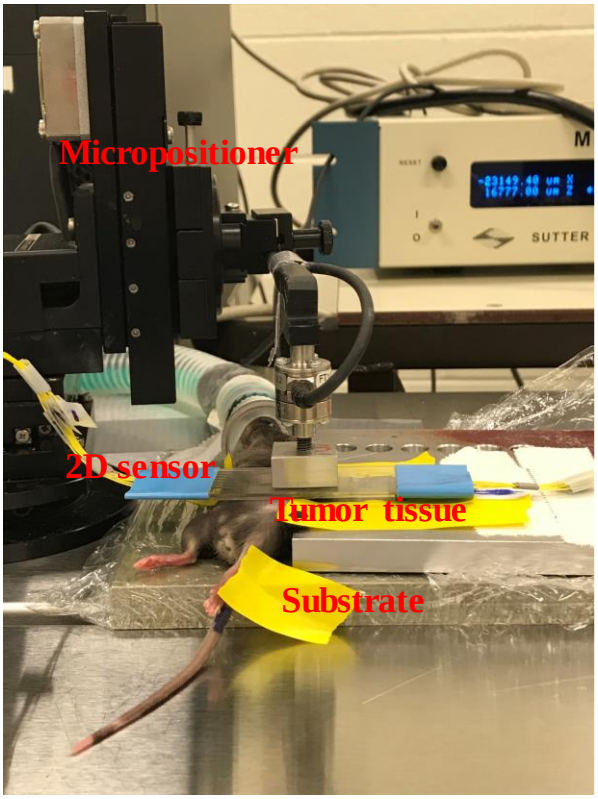

(b)

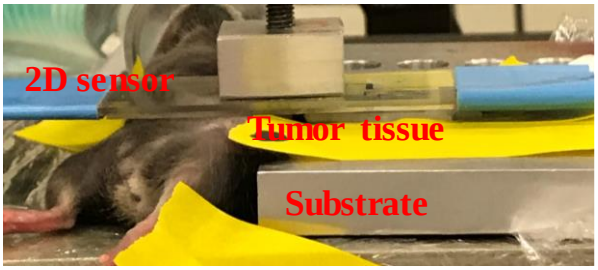

Figure 5.5 Pictures of the experimental setup for *in vivo* measurement on the mechanical behavior of a pancreatic tumor (PT) tissue (a) the whole setup (b) the 2D sensor being aligned with a pancreatic tumor tissue.

The palpated tissue area was 3mm×7.5mm. The same sensor is utilized to palpate the four tumor tissues to avoid the effect of performance variation among individual sensors on the measured results. The transducers in the two edge rows could not register any meaningful data due to the PT small size, and thus their results were no included.

5.2 Results

5.2.1 *Ex Vivo* Measurements on Mouse Breast Tumor Tissues

5.2.1.1 Measured Stiffness and Instant-Relaxed Stiffness Change

Figure 5.6 shows how the measured instant and relaxed stiffness vary among the measured tissue sites, which are simply labeled as numbers, in a tumor tissue. Meanwhile, their corresponding instant-relaxed stiffness change is also plotted. Note that some tissue sites register a negative measured stiffness, because a stiff tumor dramatically deflects the sensing-plate above it and thus squeezes the electrolyte underneath to follow into other transducers. This is not believed to influence the mechanical characterization of a tumor, since the tissue sites registered with a negative stiffness represent healthy tissue. The instant stiffness and relaxed stiffness are very close, and the tissue sites with relatively high instant and relaxed stiffness represent the location of a tumor. The instant-relaxed stiffness change is at least one order of magnitude smaller than the instant and relaxed stiffness at the location of a tumor. Thus, this instant-relaxed stiffness change is believed to carry larger measurement errors than the stiffness. However, the distribution of the instant-relaxed stiffness change still roughly follows how the instant and relaxed stiffness varies among the tissue sites in a tissue. Notably, the tissue site with the maximum instant stiffness coincides with the tissue site with the maximum instant-relaxed stiffness change in each tissue for all the tissues, except Tissue #5. Among all the tissues, Tissue #5 exhibits the lowest measured stiffness. Tissue site 25 in it registers the maximum instant-

relaxed stiffness change, which is believed to result from measurement errors, due to the relatively low instant elasticity of the tissue itself.

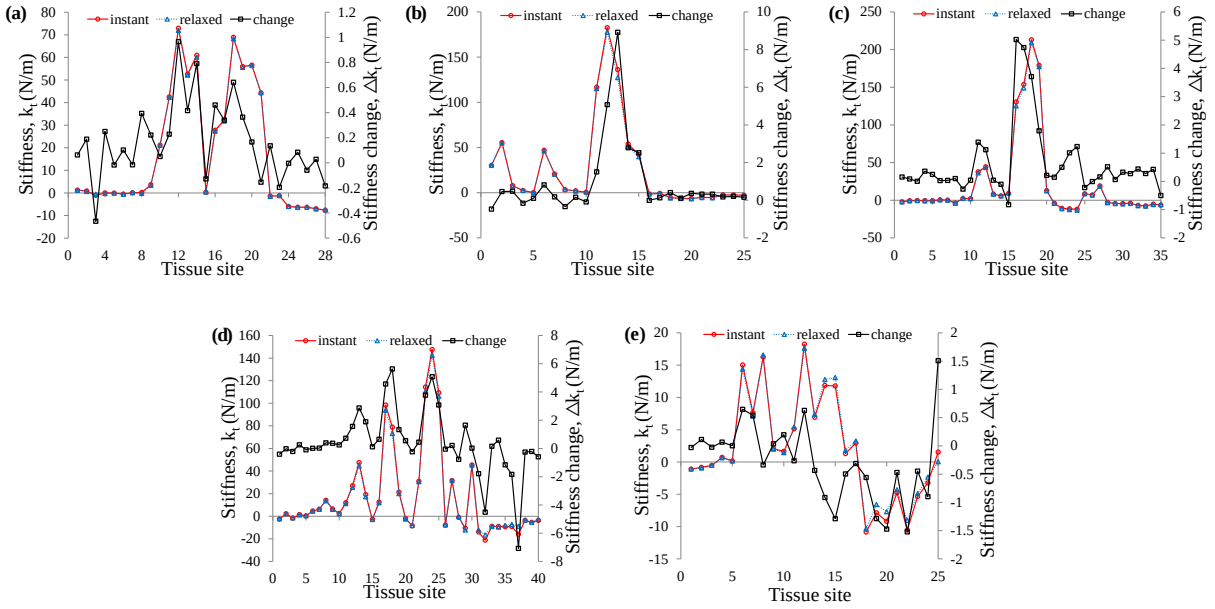

Figure 5.6 Measured instant stiffness, $k_{t\text{-}instant}$, relaxed stiffness, $k_{t\text{-}relaxed}$, and the instant-relaxed stiffness change, $\triangle k_t$, in the tumor tissues (a) Tissue #1 (b) Tissue #2 (c) Tissue #3 (d) Tissue #4 (e) Tissue #5.

As will be seen later, all the tumors in the tissues take their own irregular shapes, and the salient mechanical feature of a tumor is its high stiffness relative to its surrounding healthy tissue. Thus, the tissue site with the maximum instant stiffness in a tissue is chosen to represent the tumor center. The measured mechanical parameters and mechanical properties at the tumor center are utilized to represent those of the tumor. The instant stiffness and instant-relaxed stiffness change of the five tumors are summarized in Table 5.2, together with the tissue thickness. Evidently, the tumors follow the order: #3, #2, #4, #1 and #5, in terms of decreasing instant stiffness and instant-relaxed stiffness change. As mentioned in Section 5.1,1, the tissue

thickness is indicative of the tumor size. Thus, the tumors follow the order: #2, #3, #1&#4 and #5, in terms of decreasing size.

5.2.1.2 Measured Mechanical Properties

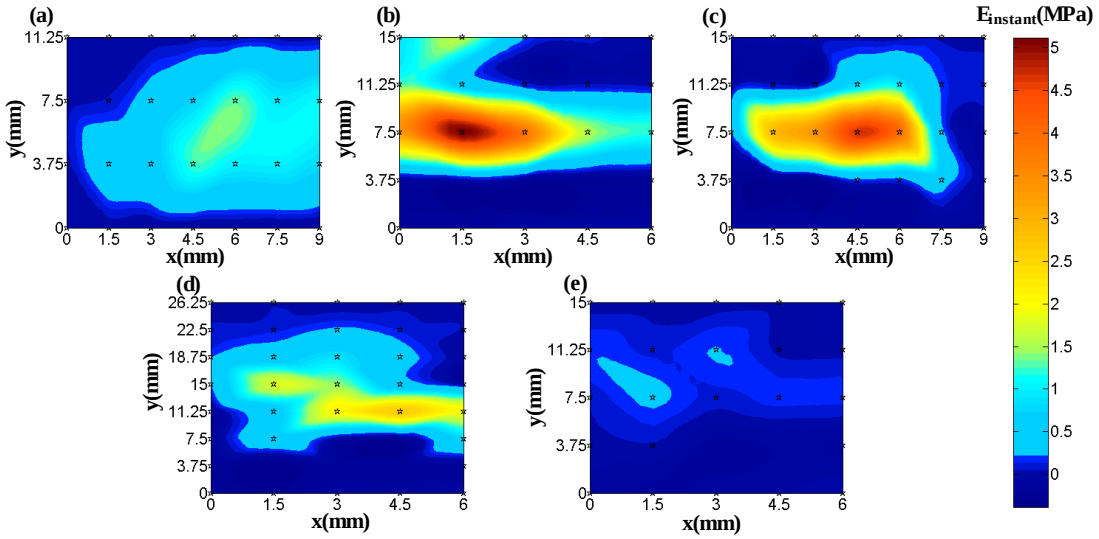

Figure 5.7 Instant elasticity, $E_{instant}$, distribution among the measured tissue sites in the tumor tissues for determining the location, shape and size of a tumor (a) Tissue #1 (b) Tissue #2 (c) Tissue #3 (d) Tissue #4 (e) Tissue #5.

Table 5.2 Comparison of the measured stiffness, stiffness change, instant elasticity, relaxation extent, and loss tangent among the five tumor tissues.

Tissue No.	$k_{instant}$ (N/m)	Δk_t (N/m)	$E_{instant}$ (MPa)	E'(MPa)	$tan\ \delta$
1	72.931	0.965	1.313	0.017	3.62
2	182.678	8.919	5.115	0.250	0.26
3	212.992	5.024	4.684	0.111	0.30
4	147.528	5.632	2.656	0.101	1.80
5	18.253	0.648	0.256	0.009	45.11

Figure 5.7 shows the instant compression modulus distribution among the measured tissue sites in the tissues. This distribution determines the existence, location, shape and size of the tumor in a tissue. Notably, all the tumors take their own irregular shapes. The instant

elasticity and relaxation extent of the five tumors are summarized in Table 5.2. Comparison of these two mechanical properties among the five tumors is further illustrated in Figure 5.8. The five BT tissues followed the order: #2, #3, #4, #1 and #5, in terms of decreasing instant elasticity and relaxation extent. However, these five BT tissues showed an increased loss tangent following the same order.

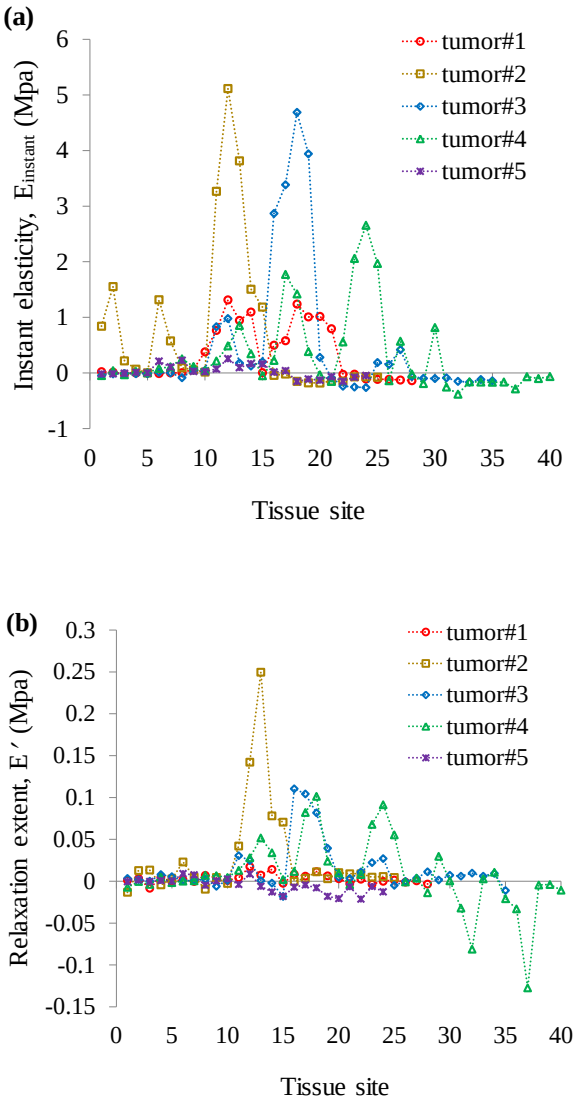

Figure 5.8 Comparison of (a) the instant elasticity (b) the relaxation extent among the five tumor tissues.

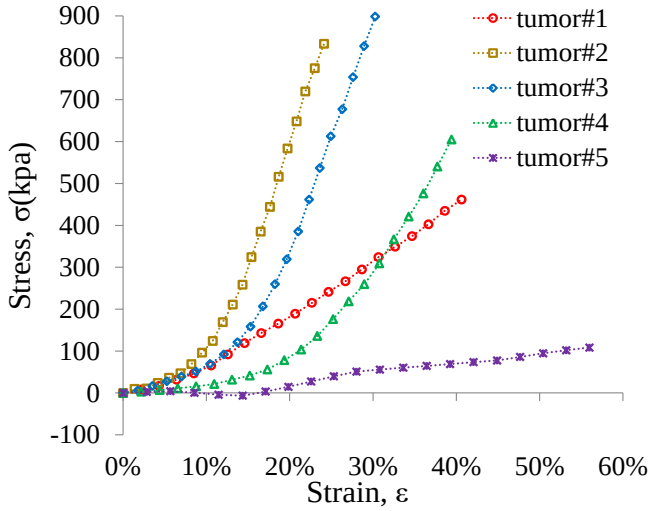

Figure 5.9 Comparison of the instant stress-strain relations among the five tumor tissues.

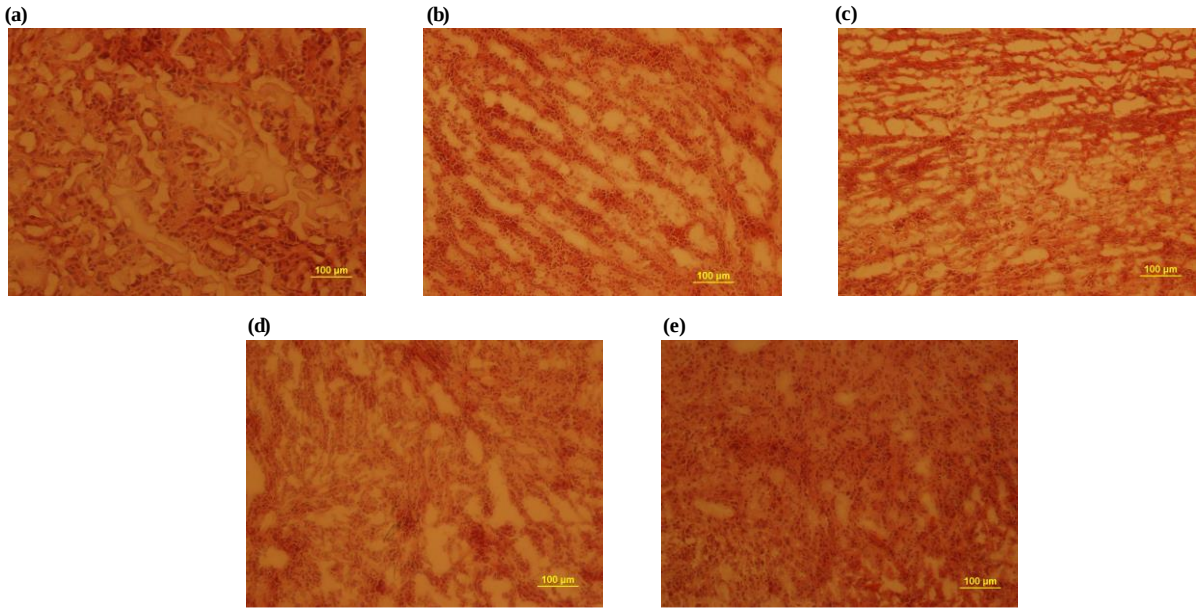

Figure 5.10 Histological analysis of the tumor tissues at 10X: (a) Tissue #1 (b) Tissue #2 (c) Tissue #3 (d) Tissue #4 (e) Tissue #5.

Figure 5.9 plots the instant stress-strain relations of the five tumors. Since the final compression depth is kept at 4mm, the maximum strain experienced by Tumor #2 is the smallest due to its largest thickness, while the maximum strain experienced by Tumor #5 is the largest,

due to its smallest thickness. While Tumor #2 reaches into nonlinear region at a very small strain (~5%), Tumor #5 reaches into nonlinear region at a much larger strain (~25%). The five tumors following the order: #2, #3, #4, #1, and #5, in terms of decreasing nonlinearity.

5.2.1.3 Histological Analysis

Figure 5.10 shows the representative pictures of H&E staining for five breast tumor tissues, separately. Although a 4T1 tumor grows slightly faster than a 4T1-luc tumor in mice, morphologically, both (4T1 Tumors #1 and #2 vs 4T1-luc Tumors #3-#5) cells are poorly differentiated and very aggressive. Note that the 4T1-luc tumors grew 10 days longer than the 4T1 tumors. The cancer cells have prominent large and distorted nucleus with great variety of sizes and shapes. No normal mammary glands and ducts are seen in all the tumors. Duct-like structures are present in all five tumors, but there are more of those structures in Tumors #2 and #3 than in Tumors #1, #4 and #5. In lumens of some duct-like structures, there are colloid substance, which occurs more abundant in Tumors #1, #4 and #5 than in Tumor #2 and #3.

5.2.2 *In Vivo* Measurements on Mouse Pancreatic Tumor Tissues

Figure 5.11 plots the instant and relaxed stress-strain relations of the two PT tissues. Since the final compression depth is kept at 1.2mm, the maximum strain experienced by PT2 is the smaller due to its larger thickness compared with PT1. These two PT tissues before treatment displayed a higher nonlinearity than these two tissues after treatment. Noted that these two PT tissues showed a lower nonlinearly compared with the five BT tissues. The instant elasticity ($E_{instant}$) and loss tangent (tan δ) of the two pancreatic tumors (PT) tissues *in vivo* before treatment and after treatment are summarized in Table 5.3. The PT2 before treatment showed a higher instant elasticity and relaxation extent than PT1 before treatment. The two PT tissues before treatment revealed a higher elasticity and relaxation extent than these two tissues after

treatment. However, PT2 before treatment showed a lower viscoelasticity than PT1 before treatment.

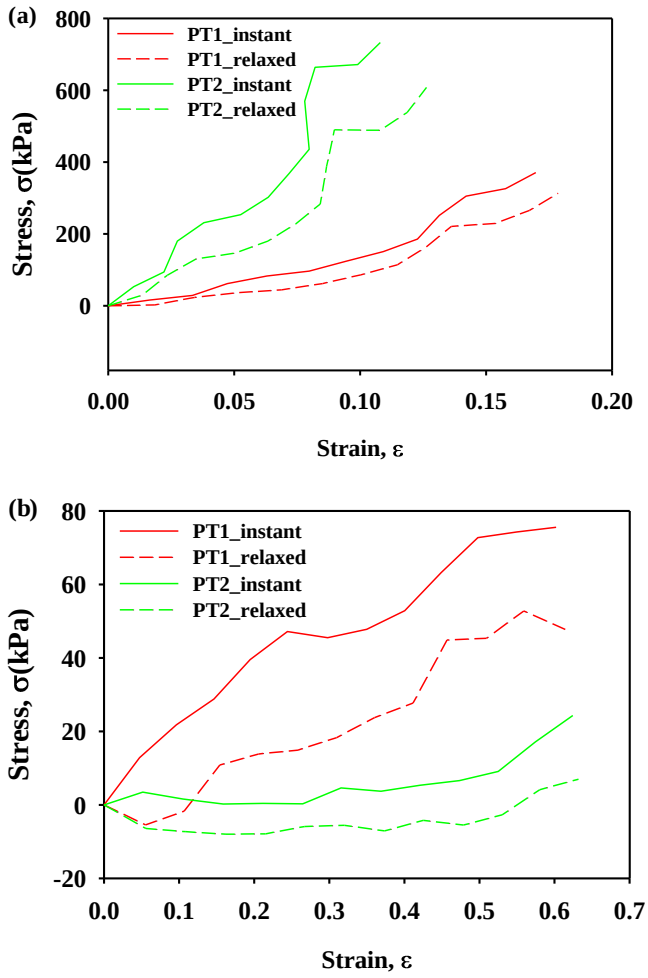

Figure 5.11 Measured instant stress-strain relations of the two PT tissues (a) before treatment, and (b)after treatment.

Table 5.3 Comparison of the measured stiffness, instant elasticity, and loss tangent among the two pancreatic tumor tissues before treatment and after treatment.

Tissue No.		$k_{instant}$ (N/m)	$E_{instant}$ (MPa)	E'(MPa)	$tan\ \delta$
Before treatment	PT1_before	211.34	2.23	0.42	13.83
	PT2_before	649.57	7.22	2.19	3.58
After treatment	PT1_after	31.64	0.12	0.02	-
	PT2_after	7.71	0.03	0.02	-

5.3 Discussion

The purpose of this study was to validate the feasibility of the instant elasticity of a tissue measured using the Stepwise Compression-Relaxation testing method to be used for tumor detection. It is well accepted that a tumor is much stiffer than its surrounding healthy tissue. Thus, the common practice for tumor identification in a tissue is examining whether some tissue sites exhibit a certain higher stiffness than the rest tissue sites, with no need to obtain their modulus. Thus, it is the relative values, rather than the absolute values, that are critical for tumor identification. As to comparing mechanical behavior among tumors in different tissues, whether the stiffness is suitable as the comparison metric depends on the tissue thickness. If the thickness is the same for all the tissues embedded with a tumor, then the stiffness and stiffness change can represent the instant elasticity and relaxation extent, respectively. If the tissue thickness varies among the tissues, then the stiffness fails to represent the mechanical properties of the tumors. This explains the reason that the tumors follow different orders, in terms of the measured stiffness and stiffness change versus in terms of the instant elasticity and relaxation modulus and nonlinearity. As shown in Table 5.2, Tumor #3 registers higher measured stiffness and stiffness change than Tumor #2, but reveals lower instant elasticity and relaxation extent than Tumor #2, simply because of their thickness difference.

In a traditional stress relaxation measurement, the sensor is pressed against a tissue region with a pre-defined compression depth at a ramp-up rate and is kept there for certain time. The reaction force of the tissue region as a function of time is recorded for quantifying its viscosity. However, the misalignment error between the sensor and the tissue region (i.e., uncertainty in contact point) varies among the five tumors and can significantly distort the absolute value of the

measured viscosity. To alleviate such misalignment errors, the viscosity of a tumor in this work is obtained from its multiple stress relaxation behavior at consecutive compression depths.

The mechanical characterization of the five tumors is consistent with the findings in the literature: the instant elasticity, relaxation extent and nonlinearity all show a positive correlation with the tumor progression. In the theoretical model for translating the measured stiffness and stiffness change to the instant elasticity and relaxation extent, the connectivity among different tissue sites is neglected. This will introduce errors in the absolute values of the instant elasticity and relaxation extent. However, the values of these two mechanical properties of the five tumors carry the same amount of errors from this model and thus do not influence the comparison results of the five tumors.

The five tumors were from either 4T1 or 4T1-luc cancel model and were harvested after two different growth times. Based on the histological analysis, there is no difference between these two tumor cells in term of cancer cell morphology. Interestingly, structural differences, such as duct-like structure, and secretion of colloid substance, are observed in the five tumors, and may be correlated with the mechanical measurement of tumors. Duct-like structures are more in Tumors #2 and #3 whereas lumen colloid substance is more often in Tumors #1, #4 and #5. This may explain why Tumors #2 and #3 exhibit higher instant elasticity, higher relaxation extent and larger nonlinearity than the rest tumors. However, more tumor samples and quantitative methods are needed to reach such a conclusion and explain the relatively small difference in mechanical behavior among Tumors #2 and #3 and among Tumors #1, #4 and #5, in terms of biological features. Finally, based on the measured mechanical behavior of the five tumors, it becomes evident that tumor cancer model and growth days do not directly correlate

with the tumor progression, indicating unpredictable tumor progression variability among individuals.

The two tumors were from either PAN02 cancel model and were first measured after a growth time of 7day. Afterwards, the two tumors were treated with irreversible electroporation and were measured 27day after the treatment. The measured instant elasticity and relaxation extent of PT2 was higher than that of PT1. However, PT1 showed a higher viscoelasticity that PT2. This observation was consistent with the measured results of the five BT tissues *ex vivo*. While based on the measured mechanical behavior of these two PT tissues it showed that the measured elasticity and viscoelasticity were different between the PT tissues before treatment and after treatment. This observation implied that the measured elasticity and viscoelasticity may have the potential to be used to evaluate the effect of applied treatment to the PT tissues.

5.4 Conclusion

The measured results on the mouse breast tumor tissues *ex vivo* were the relations of the instant and relaxed sensor deflection versus compression depth at the measured tissue sites. These relations give rise to the measured stiffness and instant-relaxed stiffness change, which were unsuitable for differentiating the mechanical behavior among the tumors, due to their difference in thickness. The measured results were further established to estimate the instant and relaxed elasticity, relaxation extent and nonlinearity of the tumor tissues. The instant elasticity distribution among the measure tissue sites is utilized to determine the location, shape and size of the tumor in a tissue, indicating that the five tumors all take their own irregular shapes. In terms of decreasing instant elasticity, relaxation extent and nonlinearity, the five tumors follow the same order: #2, #3, #4, #1 and #5. This is consistent with the related findings in the literature: the elasticity, viscosity and nonlinearity of a tumor go up with its progression [8, 13, 51]. Prominent

difference in biological structure is observed between the two relatively stiff tumors and the other three tumors. The difference in irregular shape and mechanical properties of the tumors reveals unpredictable tumor progression variability among individuals.

Similarly, the measured results of the mouse pancreatic tumor tissues *in vivo* were converted to the tissue elasticity and viscoelasticity. The results indicated the measured pancreatic tumor tissues showed different elasticity and viscoelasticity between before treatment and after treatment. Overall, the measured results of the soft normal tissues and tumor tissues suggested that the SCR testing method could be used for characterizing the mechanical properties of soft tissues and used as a basis for detection of tissue pathologies.

CHAPTER 6

TUMOR DETECTION BASED ON CORRELATION BETWEEN STRESS DROP AND APPLIED STRAIN

To date, elasticity and viscosity are the two most studied mechanical properties for tumor detection and differentiation. Elasticity may serve well for tumor detection, but fails to differentiate malignant tumors from benign tumors, due to overlap in elasticity between them [13, 57, 58]. In contrast, viscosity has been found to serve as a better indicator for tumor differentiation, with a clear margin between malignant tumors and benign tumors [2, 13, 59-62]. Stepwise compression-relaxation (SCR) testing method entails a cycle of multiple increasing applied strains as step inputs and followed by a period of stress relaxation at each applied strain, and thus is robust to misalignment errors and tissue surface unevenness, as compared with one step stress relaxation and creep testing [65].

This chapter describes the implementation of the SCR testing method for differentiation between tumor tissues and normal tissues. The relation between s stress drop ($\Delta\sigma$) and applied strain (ε) of the tested soft samples obtained by the SCR testing method were quantitatively analyzed using Pearson correlation analysis as slope (m) of $\Delta\sigma$ and ε and coefficient of determination (R^2) for tissue differentiation. Feasibility of the correlations of stress drop and strain for tumor detection was experimentally validated by measurements on soft samples, including commercially available PDMS/silicone rubbers, porcine/bovine normal tissues, mouse breast/pancreatic tumor tissues. First, a three-factor-three-level factorial design was applied to the PDMS/silicone rubbers. The measured results were used to investigate the individual and interaction effects of testing parameters on the m and R^2 via three-way ANOVA analysis. Next, the measured results on the normal tissues and tumor tissues were compared using unpaired

Student's t-test to study the feasibility of correlation of $\Delta\sigma$-ε relation (m and R^2) for tumor detection [96].

6.1 Materials and Methods

Five groups of soft materials and tissues, which including PDMS/silicone rubbers (n=4), mouse breast tumor tissues *ex vivo* (n=5), mouse pancreatic tumor tissues *in vivo* (n=2), normal tissues (n=6), and normal tissues with/without dummy tumor (n=3) were prepared and measured using the Stepwise Compression-Relaxation testing method, respectively. The key parameters of these groups of soft materials and tissues were summarized in Table 4.1 and Table 5.1. Details of the sample preparation of the PDMS, silicone rubbers, normal porcine and bovine tissues, mouse breast tumor tissues, and mouse pancreatic tumor tissues have been presented in Section 4.1.1 and Section 5.1.1. A brief introduction of the measured samples was presented in this chapter for completeness.

Two PDMS samples of two different mixing ratios (curing agent to base of Sylgards 184kit, Dow Corning Corp.): 1:10 (Young's modulus, 580kPa, [83]) and 1:20 (Young's modulus, 445kPa, [84]) were prepared. Two silicone rubbers (Mold Star^{TM}30, Young's Modulus, 662kPa; Mold Max^{TM} 10T, Young's Modulus, 200kPa) were also prepared. The PDMS samples and silicone rubbers (Table 4.1(d)) were labeled as P1, P2, SR1, and SR2, respectively. These soft material samples were tested for evaluating the influence of testing parameters on the measured correlation of stress drop and applied strain.

The group of five breast tumor (BT) tissues *ex vivo* (Table 5.1(a)) were from the orthotopic mouse breast cancer model established by injection of 10^6 4T1 or 4T1-luc cells in 50uL PBS into the left posterior mammary gland [94]. The thickness and the measured highest instant elasticity of these tissues were summarized in Table 5.2(a) [70]. The group of two mouse

pancreatic tumor (PT) tissues *in vivo* (Table 5.1(b)) were from injection of PAN02 cells on the left flank and were measured after a 7day growth. Afterwards, the two tumors were treated with irreversible electroporation [95] and were measured 27day after treatment. The experimental protocol was approved by Old Dominion University Institutional Biosafety Committee (IBC) and Institutional Animal Care and Use Committee (IACUC). A red rectangular marker denoted the palpated area in each PT tissue in Figure 5.2.

Table 4.1(b) summerizes the group of six normal bovine and porcine tissues. Table 4.1(c) lists the group of three normal tissues embeded with and without a dummy tumor (DT), which was a silicone rubber (Mold Star^{TM}30, Smooth-On, Inc) for the influence of dummy tumor on the measured results. Figures 6.4 and 6.5 show the pictures of these two groups of tissue samples, respectively, and their palpated area with three highlighted tissue sites to show the measured results on theses tissue sites. A blue rectangular marker denoted the location of the dummy tumor in a tissue Figure 6.5.

6.1.1 Measurements on Soft Materials, Normal Tissues and Tumor Tissues

As presented in Chapter 3, the Stepwise Compression-Relaxation testing method built upon the 2D sensor was conducted on the soft tumor tissues to characterize their mechanical properties. The core of the sensor was a PDMS microstructure embedded with a 3×3 sensing-plate/transducer array of 3mm×7.5mm (spatial resolution: 1.5mm×3.75mm), the sensing region. The in-plane dimension of each sensing-plate was 0.5mm×1mm. Details of the 2D tactile sensor was presented in Chapter 2. The deflection acting on a sensing-plate, defined as the sensor deflection, z_s, was recorded by the transducer underneath. Although the sensing region of the sensor was small, the in-plane dimension of the PDMS microstructure is much larger than the

sample thickness. Thus, the sensor-tissue interaction was treated as a tissue being axially compressed by the PDMS microstructure.

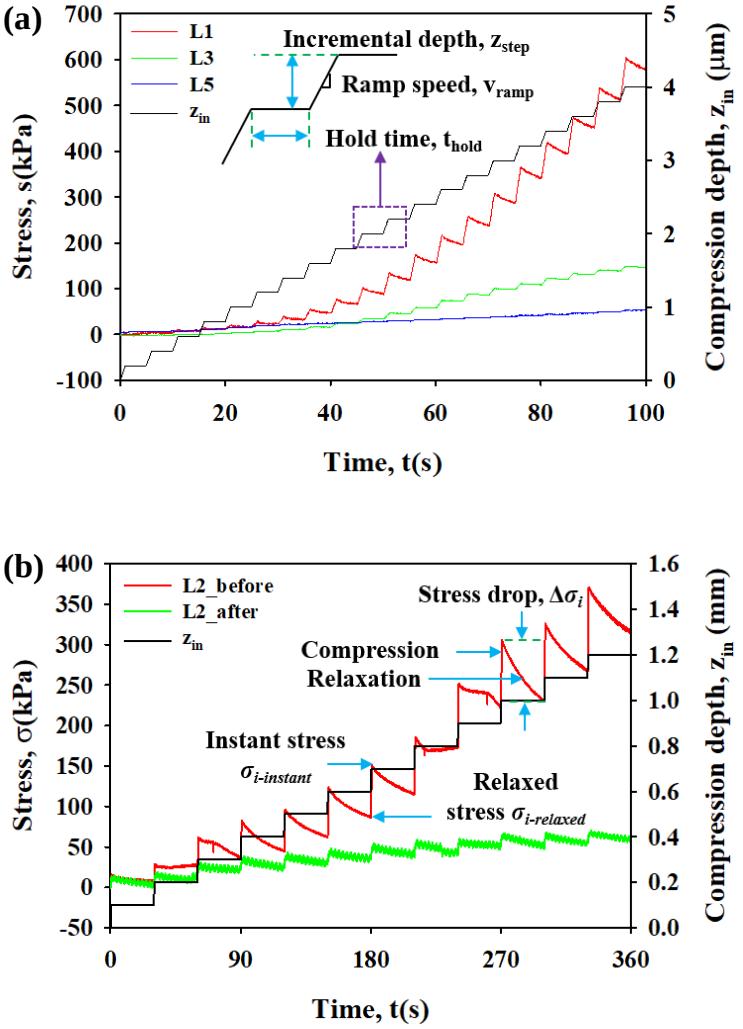

Figure 6.1 Measured results on the tumor tissues using the Stepwise Compression-Relaxation testing method. (a) measured stress, σ, and applied compression depth, z_{in}, as a function of time, t, of a mouse breast tumor tissue (BT4) at L1, L3, and L5, and (b) measured stress, σ and applied compression depth, z_{in}, as a function of time, t, of a mouse pancreatic tumor tissue (PT1) before and after treatment at L2.

Prior to testing, a tissue was placed on a rigid substrate fixed on a 5-axis stage. Then, the

sensor was brought down to the sample surface until all the sensing-plates exhibited a small output (or was deformed). Afterwards, the 5-axis stage was manually adjusted [70, 77] until the outputs of the sensing-plates at the four corners had similar small outputs to minimize tilt misalignment, which could not be alleviated by the Δσ-ε relation. As such, a sample was initially pre-compressed a little bit, and the strain experienced by the sample was assumed to be zero after alignment. Afterwards, the sensor was used to compress a sample with an incremental step depth, z_{step}, at a ramp speed, v_{ramp}, and held there for a hold time, t_{hold}, and this compression-relaxation step was repeated multiple times until a final compression depth, z_{final}, was reached. Therefore, every incremental step input was followed by a t_{hold}-period of stress relaxation. The step inputs of the sensor were controlled by a micropositioner. The reaction force at the tissue site underneath a transducer was recorded by the transducer. A custom LabVIEW program was utilized to conduct all the measurements and record all the original data [70].

Since the measured viscoelastic behavior of a tumor/ normal tissue is affected by its previous measurement, even given enough relaxation time [46], only the group of PDMS/silicone rubbers was utilized for examining the influence of the testing parameters on the measured results. A total of 27 measurements were made on each of the PDMS/silicone rubber samples with each testing parameter at three values: z_{step}: 100μm, 200μm, and 300μm; v_{ramp}: 250μm/s, 500μm/s, and 1000μm/s; and t_{hold}: 5s, 15s, and 30s. The selection of these values was based on our previous work [70].

Table 6.1 lists the testing parameters used for the rest groups. The values of the testing parameters used in each group of soft tissues were chosen based on the following requirements: 1) z_{step} and t_{hold} hold time were chosen so that the measurement could be finished in a short-time period and yet had enough compression-relaxation steps to study the $\Delta\sigma$-ε relation; 2) v_{ramp} for

the tumor tissues was lower than that for the normal tissues, because the tumor tissues were stiffer than the normal tissues. Note that z_{final} was adjusted in accordance with the sample thickness for desirable final applied strain.

Table 6.1 Testing parameters and their values used in the Stepwise Compression-Relaxation testing method for measurements on the tumor tissues and normal tissues.

Measurements			Testing paramerters			
			z_{step} (μm)	t_{hold} (s)	v_{ramp}(μm/s)	z_{final} (mm)
Tumor tissues	Mouse breast tumor tissues (*ex vivo*)		200	5	200	4
	Mouse pancreatic tumor tissue (*in vivo*)	Before treatment	100	30	200	1.2
		After treatment				
Normal tissues	With no dummy tumor With embedded dummy tumor		75	5	1000	3

Owing to the large size of a tumor in the BT tissues, multiple measurements at different locations of the BT tissue surface were conducted for mapping out the instant elasticity distribution. Since the tumor in each PT tissue was only 2~3mm in diameter, only one measurement on each PT tissue was conducted, with the middle row of the transducer array aligned on top of the tumor. The transducers in the two edge rows could not register any meaningful data due to the PT small size, and thus their results were not included. While the purpose of measuring the normal tissues with/without dummy tumor was for comparison with the native tumor tissues, three repeated measurements were conducted on each normal tissue with/without dummy tumor. As compared with the results from the rest transducers, the measured results from the transducers in the middle row on the normal tissues with/without dummy tumor were immune to misalignment errors [77] and were utilized for analysis later on. As labeled in Figures 6.3, 6.4 and 6.5, the three tissue sites, L1, L2 and L3, corresponded to the transducers in the middle row of the 2D sensor (labeled as 4, 5, and 6 in Figure 3.1(a)).

6.1.2 Statistical Analysis

All statistical analysis was performed by using the Statistics and Machine Learning Toolbox in Matlab R2017b (The MathWorks, Inc. Natick, Massachusetts, United States). Pearson correlation analysis was conducted on the measured $\Delta\sigma$-ε data points for all the groups to quantify the $\Delta\sigma$-ε correlation as the slope, $m=\Delta\sigma/\varepsilon$, and coefficient of determination, R^2, with the latter being a measure of the goodness of fitness after linear regression between the stress drop ($\Delta\sigma$) and the applied strain (ε). A high R^2 translates to a strong $\Delta\sigma$-ε linear correlation. All the data on m and R^2 were expressed as mean ± standard deviation. Statistical comparisons of m and R^2 between groups, different tissue sites of before and after treatment were conducted for tumor detection by using unpaired Student's t-test. For any significant individual and interaction effects of the three testing parameters on the values of m and R^2, the experimental data on the group of PDMS/silicone rubbers were analyzed by using three-way ANOVA analysis. Statistical significance was set at $p<0.01$ for all analyses.

6.2 Results

6.2.1 Influence of Testing Parameters on the Correlation Between Stress Drop and Strain

The p-values of slope and coefficient of determination from the ANOVA analysis of the PDMS/silicone rubbers were used to evaluate the dependency of the $\Delta\sigma$-ε correlation on the three testing parameters. As shown in Table 6.2, the value of m showed the significant dependency on hold time, t_{hold}, ($p<0.01$) for all the samples, but was independent of ramp speed, v_{ramp}. Meanwhile, the value of m also showed significant dependency on incremental step depth, z_{step}, ($p<0.01$) for all the samples, except for P2. The interactions of any two testing parameters (i.e. $z_{step}*t_{hold}$, $z_{step}*v_{ramp}$, *and* $t_{hold}*v_{ramp}$) showed no statistically significant influence on the value of m, except the interaction of $z_{step}*t_{hold}$ for SR2 ($p<0.01$), which has the lowest elasticity among

the four samples. In contrast, the value of R^2 showed no dependency on any testing parameters and their interactions for all the four samples. As such, the slope might serve well for comparison of different samples collected using the same testing parameters, the coefficient of determination might be used for comparison of the data collected using different testing parameters.

Table 6.2 The *p*-values obtained from the three-way ANOVA analysis of the (a) individual effects, and (b) interaction effects of the three testing parameters on the slope (m) and coefficient of determination (R^2) of the group of PDMS/silicone rubbers. Effects are significant at *p*-value <0.01 (shaded cells).

(a)

Soft material	parameters	z_{step}	t_{hold}	v_{ramp}
P1	R^2	**0.0005**	**<0.0001**	0.0150
	m	0.0454	0.9673	0.5078
P2	R^2	0.0265	**<0.0001**	0.9611
	m	0.4029	0.6964	0.6346
SR1	R^2	**<0.0001**	**0.0001**	0.0543
	m	0.0747	0.5862	0.5196
SR2	R^2	**<0.0001**	**<0.0001**	0.2170
	R^2	0.0558	0.6731	0.3388

(b)

Soft material	parameters	z_{step}*t_{hold}	z_{step}*v_{ramp}	t_{hold}*v_{ramp}
P1	R^2	0.0213	0.4665	0.7500
	m	0.3369	0.3636	0.6095
P2	R^2	0.1382	0.2964	0.7459
	m	0.228	0.5656	0.3714
SR1	R^2	0.0193	0.4532	0.5717
	m	0.4348	0.4648	0.324
SR2	R^2	**0.001**	0.8718	0.5964
	R^2	0.8359	0.4054	0.5101

6.2.2 Correlations Between Stress Drop and Applied Strain

6.2.2.1 Mouse Breast Tumor Tissues *Ex Vivo*

Figure 6.2 and Table 6.3(a) illustrate the measured results on the five BT tissues. According to the measured instant elasticity distribution across each tumor tissue in Figure 6.2(a),

two tissue sites around the tumor center (the location with the highest instant elasticity), L1 and L2, were chosen and defined as BT_center sites; two sites near the tumor edge, L3 and L4, were selected and defined as BT_edge sites; and two sites outside the tumor, L5 and L6, were defined as BT_outside sites. Figure 6.2(b) plots the measured $\Delta\sigma$-ε data at the six sites of each BT tissue. For all the BT tissues, stress drop revealed a significant positive correlation (both $p<0.01$ and $R^2>0.5$) with applied strain at the BT_center sites, and did not reveal any significant correlation (either $p>0.01$ or $R^2<0.5$ or both) with applied strain at the BT_edge and BT_outside sites.

The value of m at the BT_center sites varied significantly from m=7.61 to m=169.84 among the five BT tissues. Comparison of the value of m at the BT_center sites with their measured instant elasticity in Table 6.3(a) revealed that a stiffer tumor translated to a larger value of m. Since a large stress drop upon an applied step strain indicates large relaxation behavior and thus high viscosity, a large value of m translates to a high viscosity. As such, the value of m at the BT_center sites were representative of the BT viscosity. Since BT2 and BT5 were the thickest and the thinnest among the five tissues, respectively, BT2 experienced the smallest applied step strain and BT5 experienced the highest applied step strain. Meanwhile, BT2 and BT5 experienced the largest and the smallest stress drop, respectively. Thus, BT2 and BT5 were the most and the least viscous tumors in this group.

Furthermore, according to the decreasing order of the value of m, the five BT tissues were listed as: BT2>BT3>BT4>BT1>BT5. Note that viscosity of the BT tissues was previously found to increase with their elasticity [70]. Despite being immune to variation in testing parameters, the value of R^2 is not capable of distinguishing the difference in viscosity among the five BT tissues. As to the five BT tumors, the tumor size (approximated by the tissue thickness) increased with the tumor viscoelasticity [70].

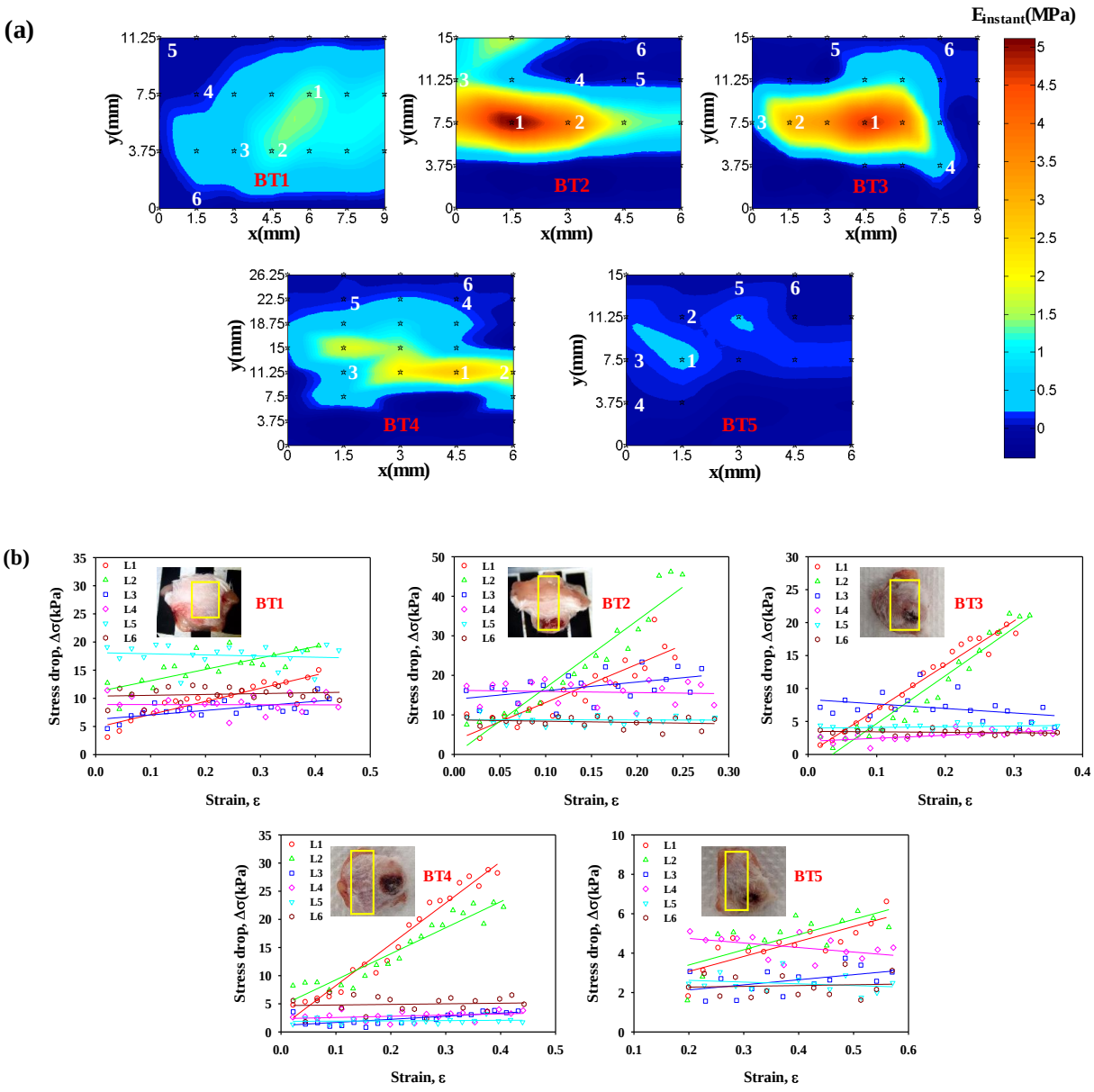

Figure 6.2 Measured instant elastic modulus distribution, and stress drop versus applied strain of the five mouse breast tumor tissues (BT1-BT5) from *ex vivo* measurements (a) Color map based on the instant elastic modulus with six highlighted tissue sites (L1 and L2 at the tumor center (BT_center), L3 and L4 at the tumor edge (BT_edge), L5 and L6 at the tumor outside (BT_outside) sites), and (b) stress drop versus applied strain of the six highlighted tissue sites, respectively.

Then, given the same tumor viscoelasticity, the influence of the tumor size on the Δσ-ε correlation could not be derived from the results on these tumors, although the measured stress at a given strain on a large tumor is expected to be higher than that on a small tumor embedded in the same size of a normal tissue.

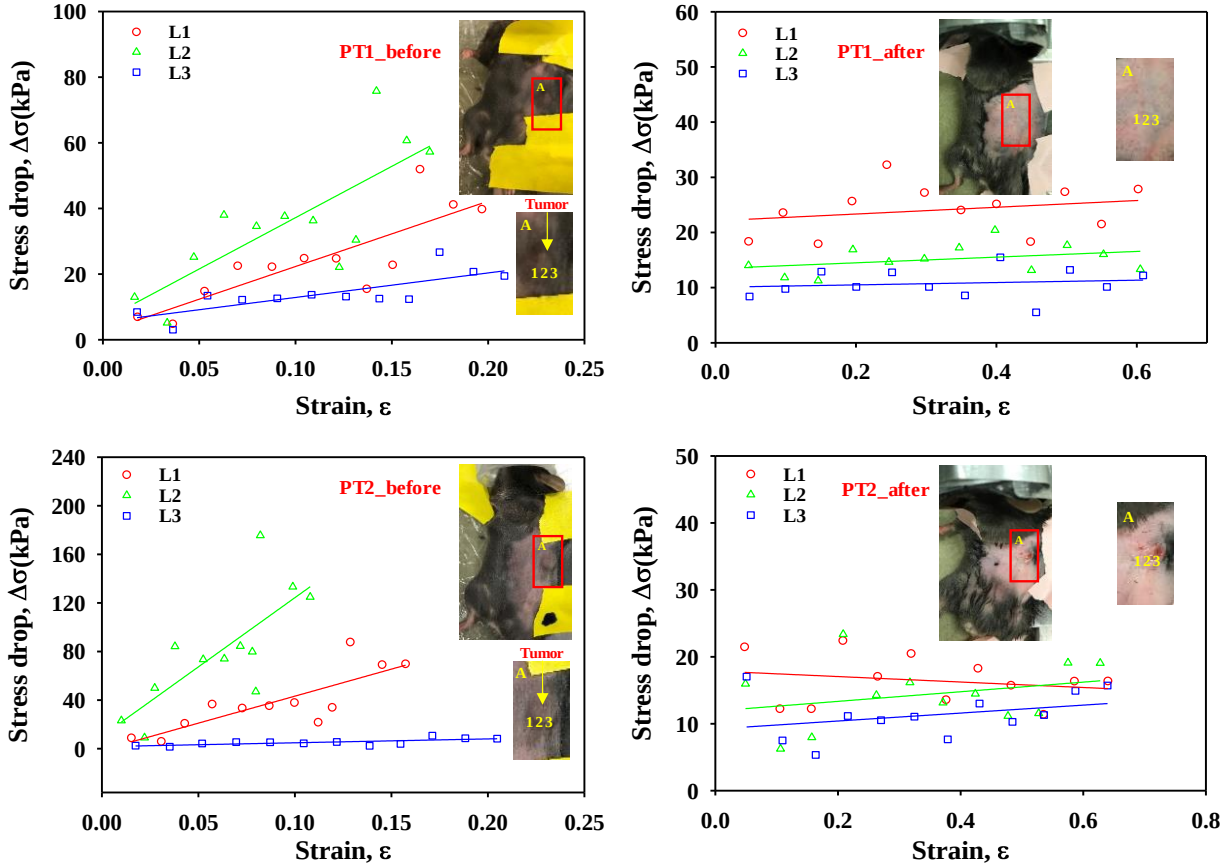

Figure 6.3 Measured stress drop versus applied strain of the three highlighted tissue sites (L1, L2, and L3) from *in vivo* measurements of the two mouse pancreatic tumor tissues before treatment (PT1_before and PT2_before) and after treatment (PT1_after and PT2_after).

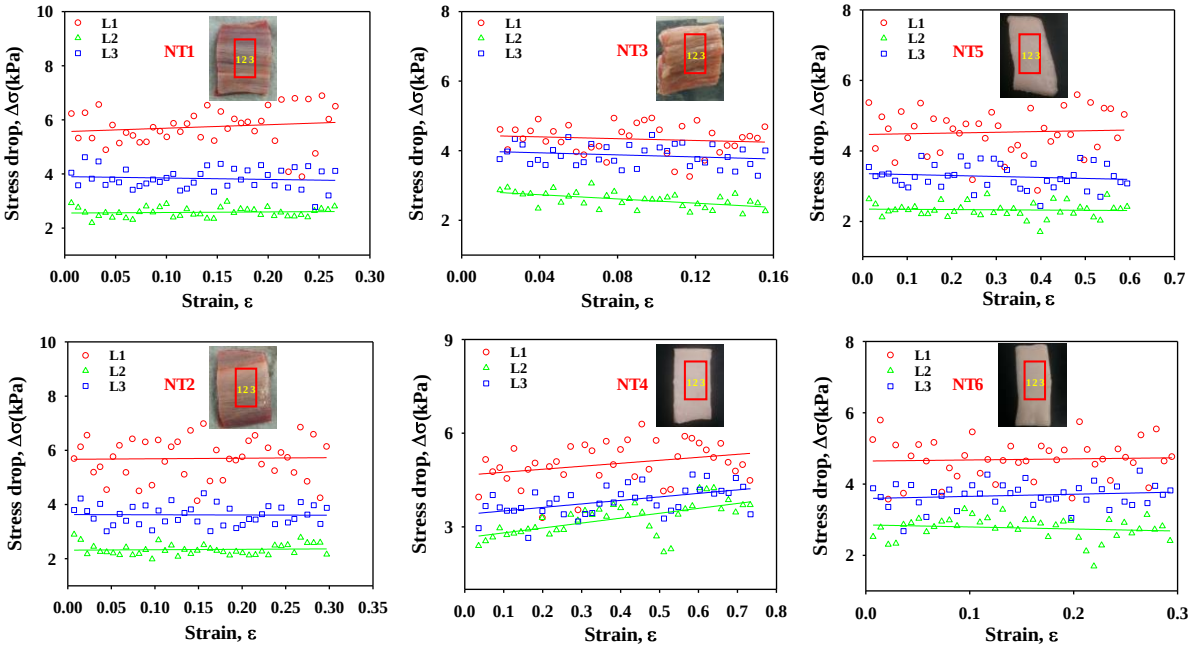

Figure 6.4 Measured stress drop versus applied strain of the three highlighted tissue sites (L1, L2, and L3) of the six normal tissues (NT1-NT6).

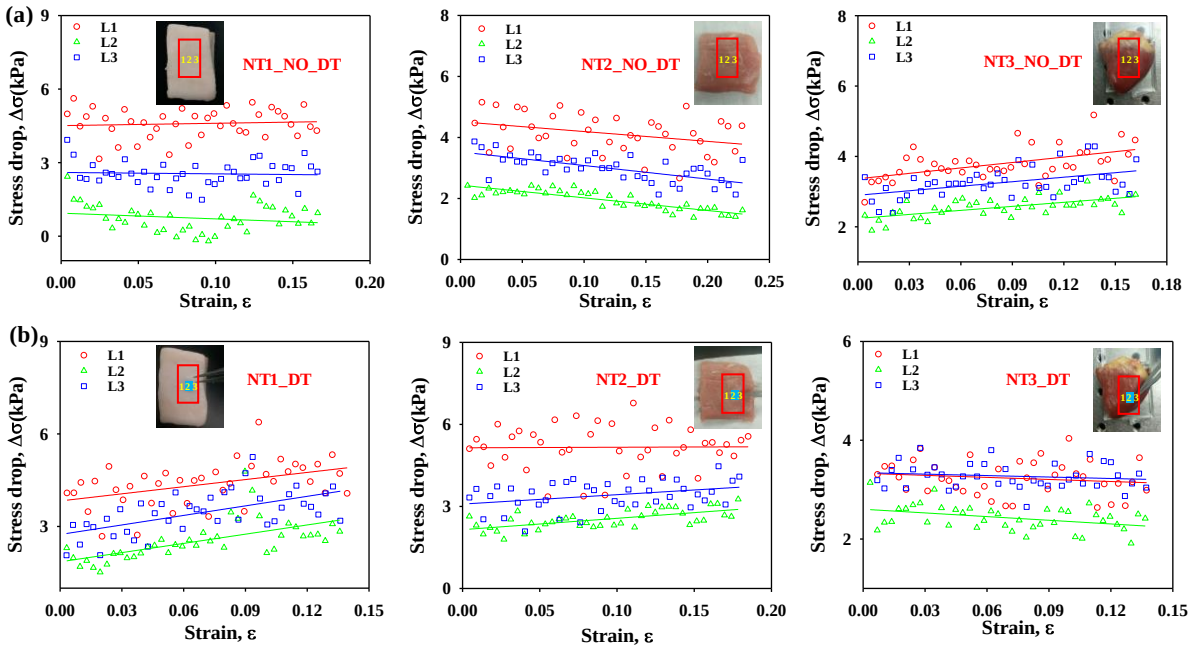

Figure 6.5 Stress drop as a function of strain of the three highlighted tissue sites (L1, L2, and L3) of (a) three normal tissue (NT1_NO_DT-NT3_NO_DT), and (b) these three tissues with embedded dummy tumor (NT1_DT, NT2_DT, and NT3_DT).

6.2.2.2 Mouse Pancreatic Tumor Tissues *In Vivo*

Figure 6.3 and Table 6.3(b) show the measured results on the group of the two PT tissues before and after treatment. For all the three tissue sites, stress drop registered a significant positive correlation (both $p<0.01$ and $R^2>0.5$) with applied strain before treatment, but demonstrate no significant correlation (both $p>0.01$ and $R^2<0.5$) with applied strain after treatment. L2 was deemed as the PT center, due to its highest value of m among the three sites before treatment. The value of m at L2 is much higher in PT2 than in PT1, indicating that PT2 is much more viscous than PT1. Again, the value of R^2 did not distinguish the difference in viscosity between the two PT tissues.

6.2.2.3 Normal Tissues

Figure 6.4 and Table 6.3(c) show the measured results on the group of six normal tissues by using the same testing parameters. For all the three tissue sites in each normal tissue, stress drop revealed no significant correlation (either $p>0.01$ or $R^2<0.5$ or both) with applied strain. The value of m is well below $m=10$. The variation in the values of m and R^2 among the three tissue sites in each tissue was believed to arise mainly from tissue surface unevenness and structural heterogeneity. Being obtained with no statistical significant correlation, the value of m for the six normal tissues was not suitable for evaluating the tissue viscosity.

6.2.2.4 Normal Tissues with and without an Embedded Dummy Tumor

Figure 6.5 and Table 6.3(d) illustrate the measured results on the group of three normal tissues with and without an embedded dummy tumor by using the same testing parameters. At the three tissue sites, stress drop showed no significant correlation (either $p>0.01$ or $R^2<0.5$ or both) with applied strain, regardless of whether a dummy tumor is present. Furthermore, the

presence of a dummy tumor did not cause any observable change in the values of m and R^2, suggesting that dummy tumors made from silicone rubbers behaved differently from native

Table 6.3 Values of slope (m), coefficient of determination (R^2), and p-value from pearson correlation analysis on the $\Delta\sigma$-ε relations of (a) mouse breast tumor tissues (BT1-BT5), (b) mouse pancreatic tumor tissues (PT1_before, PT2_before, PT1_after, and PT2_after), (c) normal tissues (NT1-NT6) and (d) normal tissues without (NT1_NO_DT-NT3_NO_DT)/with dummy tumor (NT1_DT-NT3_DT).

(a)

Tissue sites		Parameters	Tissue No. BT1	BT2	BT3	BT4	BT5
BT_center	L1	m	23.29	96.91	67.08	73.36	7.61
		R^2	0.81	0.81	0.97	0.97	0.65
		p	<0.0001	<0.0001	<0.0001	<0.0001	0.0005
	L2	m	20.17	169.84	72.48	46.24	7.70
		R^2	0.61	0.92	0.94	0.91	0.54
		p	<0.0001	<0.0001	<0.0001	<0.0001	0.003
BT_edge	L3	m	8.06	21.91	-6.84	5.50	2.58
		R^2	0.43	0.22	0.14	0.50	0.22
		p	0.002	0.04	0.11	0.0005	0.09
	L4	m	-0.14	-2.87	4.56	2.11	-2.30
		R^2	0.0001	0.01	0.43	0.11	0.21
		p	0.96	0.72	0.002	0.15	0.10
BT_outside	L5	m	-2.02	-0.43	1.06	0.48	-1.55
		R^2	0.02	0.001	0.08	0.02	0.11
		p	0.57	0.89	0.23	0.59	0.30
	L6	m	1.54	-3.26	-0.75	1.05	1.49
		R^2	0.02	0.05	0.05	0.01	0.07
		p	0.51	0.37	0.32	0.70	0.42

(b)

Tissue No.	Tissue sites L1			L2			L3		
	m	R^2	p	m	R^2	p	m	R^2	p
PT1_before	199.73	0.69	<0.001	312.79	0.60	<0.01	74.73	0.60	<0.01
PT2_before	444.80	0.66	<0.01	1138.85	0.57	<0.01	31.89	0.51	<0.01
PT1_after	6.13	0.06	0.43	5.16	0.13	0.26	2.13	0.02	0.65
PT2_after	-4.09	0.05	0.50	7.19	0.08	0.37	5.94	0.11	0.30

(c)

Tissue No.	Tissue sites								
	L1			L2			L3		
	m	R^2	*p*	*m*	R^2	*p*	*m*	R^2	*p*
NT1	1.28	0.02	0.37	0.21	0.008	0.59	-0.52	0.01	0.52
NT2	0.20	0.0006	0.89	0.16	0.004	0.69	-0.08	0.0003	0.91
NT3	-1.3	0.02	0.47	-3.68	0.41	<0.0001	-1.49	0.04	0.25
NT4	0.96	0.09	0.06	1.60	0.42	<0.0001	1.12	0.26	0.0009
NT5	0.21	0.003	0.72	-0.07	0.003	0.74	-0.28	002	0.40
NT6	0.31	0.002	0.77	-0.57	0.02	0.35	0.60	0.02	0.35

(d)

Tissue No.	Tissue sites								
	L1			L2			L3		
	m	R^2	*p*	*m*	R^2	*p*	*m*	R^2	*p*
NT1_NO_DT	0.96	0.006	0.63	-2.34	0.04	0.21	-0.57	0.003	0.73
NT1_DT	7.71	0.20	0.004	9.97	0.37	<0.0001	10.31	0.35	<0.0001
NT2_NO_DT	-3.22	0.11	0.04	-4.15	0.74	<0.0001	-4.45	0.44	<0.0001
NT2_DT	0.19	0.0002	0.94	4.15	0.40	<0.0001	3.44	0.12	0.03
NT3_NO_DT	5.15	0.27	0.0006	3.82	0.41	<0.0001	4.28	0.23	0.002
NT3_DT	-1.39	0.02	0.35	-2.48	0.15	0.01	-0.98	0.02	0.37

tumors. The variation of the values of *m* and R^2 between with and without a dummy tumor was believed to arise from the presence of a dummy tumor and the affected tissue surface unevenness from the dummy tumor.

6.2.3 Statistical Analysis on the Values of Slope and Coefficient of Determination for Tumor Detection

Figure 6.6 compares the values of *m* and R^2 among different sites of the BT tissues and the six normal tissues. There was statistically significant difference ($p<0.01$) in R^2 among the BT_center, BT_edge and BT_outside sites. No significant difference in R^2 was revealed between the BT_outside sites and the normal tissues, indicating that R^2 identified the BT_outside sites as normal tissues. In contrast, the value of m revealed significant difference between the BT_center sites and the BT_edge sites ($p<0.01$), but failed to manifest significant difference between the BT_edge sites and the BT_outside sites.

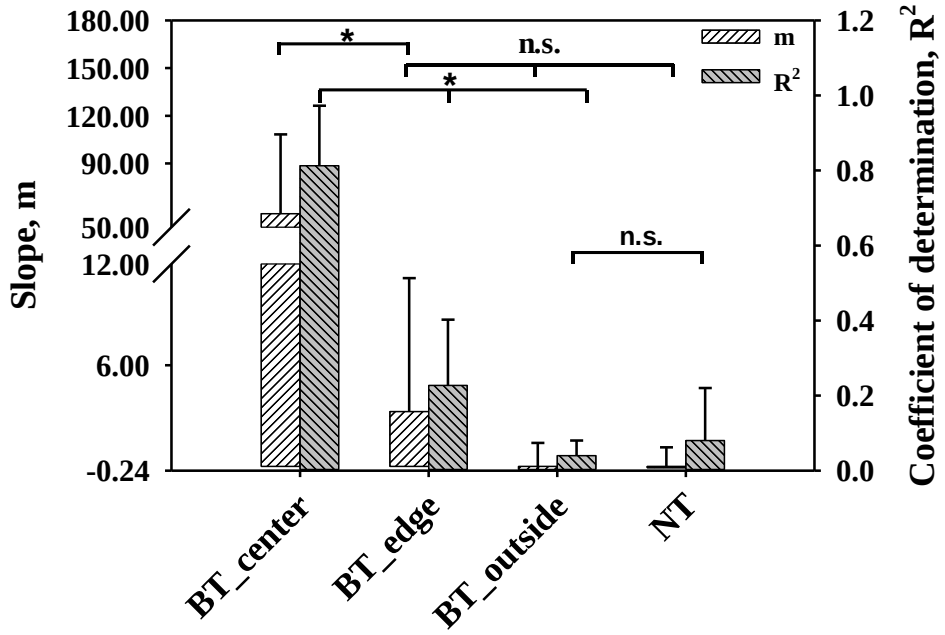

Figure 6.6 Comparison of slope (*m*) and coefficient of determination (R^2) among BT_center sites (L1 and L2), BT_edge sites (L3 and L4), BT_outside sites (L5 and L6) in the group of the mouse breast tumor tissues (BT1-BT5), and the tissue sites in the six normal tissues (NT). * symbol denotes statistical significance (*p*-value <0.01), and n.s. shows no significant difference.

As shown in Figure 6.7, statistically significant difference (p<0.01) was observed in both *m* and R^2 between before and after treatment of the PT tissues. The value of R^2 revealed no statistically significant difference between the PT tissues after treatment and the normal tissues, indicating that PT tissues after treatment were identified as normal tissues. Significant difference in *m* between the PT tissues after treatment and the normal tissues did not carry physical meaning, since the two groups were measured by using different testing parameters.

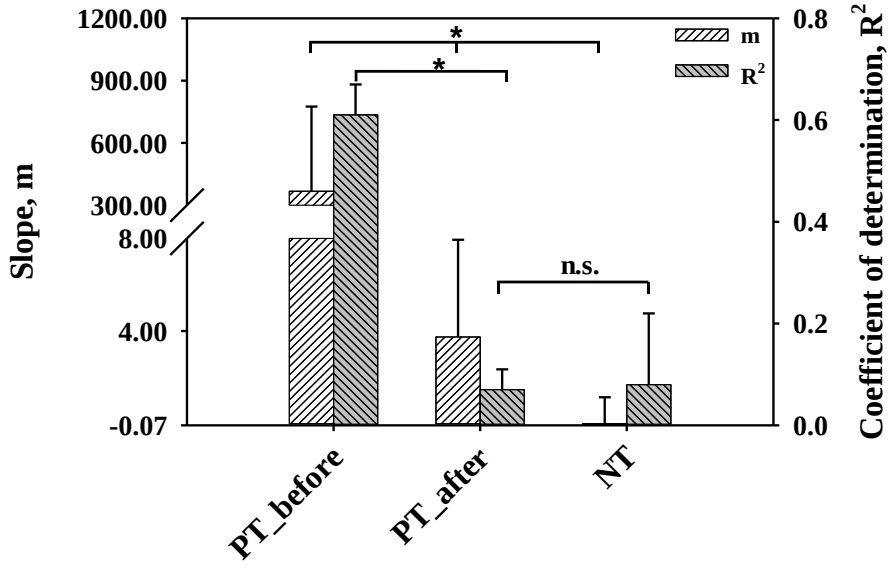

Figure 6.7 Comparison of the values of slope (m) and coefficient of determination (R^2) among the tissue sites in the group of the mouse pancreatic tumor tissues before treatment (PT-before), after treatment (PT-after), and the tissue sites in the six normal tissues (NT). * symbol denotes statistical significance (p-value <0.01), and n.s. shows no significant difference.

The PT tissues before treatment and the BT tissues are compared in Figure 6.8. The value of R^2 captured a significant difference (p<0.01) between the PT tissues before treatment and the BT_center sites. The values of R^2 of the PT tissues before treatment also revealed significant difference (p<0.01) from the BT_edge and BT_outside sites. Although the value of m revealed significant difference among the PT tissues before treatment, the BT_edge sites and the BT_outside sites, and showed no difference between the PT tissues before treatment and the BT_center sites, these observations might mainly arise from different testing parameters used. Figure 6.9 examines the influence of a dummy tumor on the values of m and R^2, showing that a dummy tumor did not generate statistically significant difference in the values of m and R^2 in the three normal tissues.

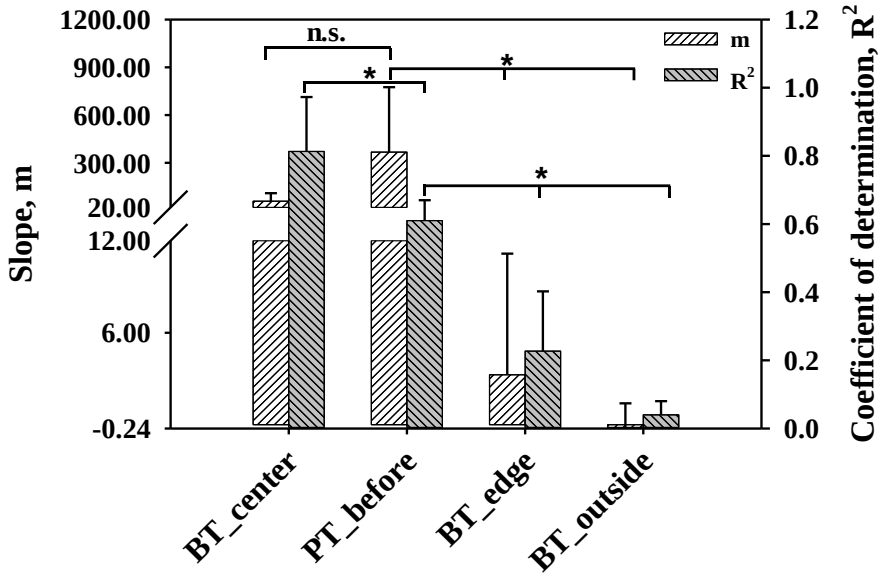

Figure 6.8 Comparison of the values of slope (m) and coefficient of determination (R^2) between the group of the mouse breast tumor tissues BT_center sites (L1 and L2), BT_edge sites (L3 and L4), BT_outside sites (L5 and L6) and the tissue sites in the mouse pancreatic tumor tissues before treatment (PT-before). * symbol denotes statistical significance (p-value <0.01), and n.s. shows no significant difference.

Despite the variation in testing parameters, the value of R^2 was capable of 1) differentiating between the center and the edge of the breast tumors and registering the tissue sites outside the breast tumors as normal tissues and 2) differentiating the pancreatic tumors from the breast tumors, and registering the pancreatic tumors after treatment as normal tissues. In contrast, the value of m failed to distinguish the pancreatic tumors from the breast tumors and register the pancreatic tumors after treatment as normal tissues, possibly due to different testing parameters used. Thus, the value of R^2 served better than the value of m as a biomarker for differentiating tumor tissues from normal tissues, despite being unsuitable for distinguishing the difference in viscosity among the different tumor tissues.

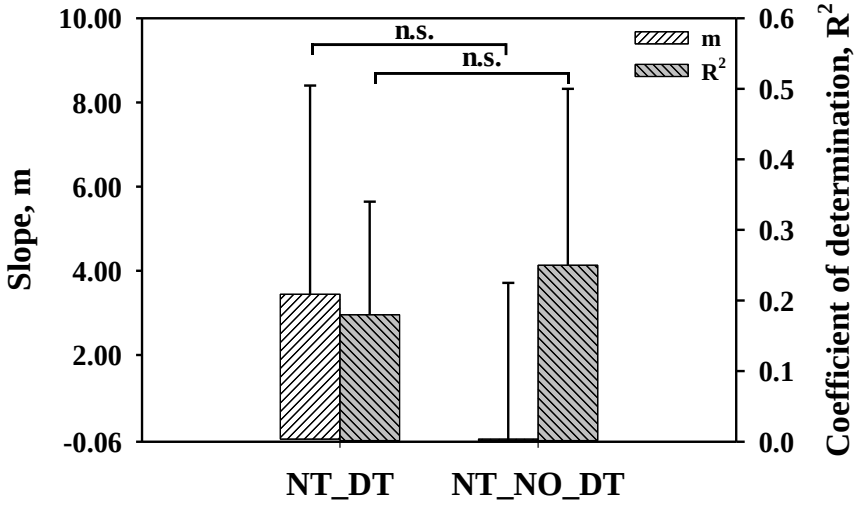

Figure 6.9 Comparison of the values of slope (m) and coefficient of determination (R^2) between normal tissue with an embedded dummy tumor (NT_DT) and with no dummy tumor (NT_NODT) of the group of the three normal tissues. n.s. shows no significant difference.

6.3 Discussion

The purpose of this study was to evaluate the feasibility of the correlation between stress drop and applied strain of a tissue measured using the Stepwise Compression-Relaxation testing method as a biomarker for tumor detection. Our results from several groups of samples suggests that 1) coefficient of determination of the $\Delta\sigma$-ε correlation is a promising for tumor detection and is independent of the testing parameters used; 2) the slope of the $\Delta\sigma$-ε correlation may work well in distinguishing the viscosity difference among the different tumors, when the same testing parameters are used, but the slope fails to distinguish the BT_edge sites from the BT_outside (normal) sites; and 3) the slope of the $\Delta\sigma$-ε correlation varies with the testing parameters, and is not suitable for comparison of the measured results from different testing parameters.

In the Stepwise Compression-Relaxation testing for measuring native tissues, tissue constructs, and biomaterials, the hold time was typically long (5min~1hr) so that a sample under

testing reached equilibrium at each applied strain [66-70]. Since a long hold time at each applied strain is unpractical in *in vivo* breast tumor detection, the hold time used in our testing was short (either 5s or 30s), and thus the tissue samples might not reach equilibrium. In one-step creep testing on breast tissues of sixteen patients, the hold time used was 10s [62]. They found that the retardation time of a first-order Kelvin-Voigt model was below 3s for the malignant and benign tumors and surrounding healthy tissues of these patients. Since the hold time was longer than this retardation time, the measured data captured the salient viscous behavior of the breast tissues. Our data successfully distinguished different tissue sites in the breast tumor tissues, before and after treatment of the pancreatic tumor tissues, the tumor tissues and the normal tissues. Thus, the hold time used in our study was long enough to register their stress relaxation behavior at each applied strain (Figure 6.1).

The measured stress distribution at the tissue surface upon compression is essentially the collective behavior of the tissue region (healthy tissue and tumor) underneath a compression plate (the PDMS microstructure in this study). According to the numerical study presented in [62], while the measured elastic parameter at a site in the tissue region under compression varies significantly with its distance to the boundaries, the retardation time at a site is relatively immune to its distance to the boundaries. Moreover, despite interference of the healthy tissue with the tumor upon compression, their retardation times were still manifested in the stress-strain relations. Since the retardation time did not generate a clear margin between the malignant tumors and the benign tumors, a contrast parameter of retardation time was defined as the ratio of the difference in retardation time between the healthy tissue and the tumor versus the mean of the two, and was found to capture statistically significant difference between the malignant tumors and the benign tumors. Additional work was conducted in their study in order to find the

edge of a tumor. As shown in Figure 6.6, the value of R^2 in our study distinguished the differences among the BT center, BT edge and the healthy tissue outside the BT.

In the study of Madani and Mojra on nine patients with breast tumors (with no differentiation between malignant tumors and benign tumors), a breast tissue region was compressed with a constant ramp speed of 1mm/s until a desirable final compression depth (8mm~22mm) was reached [61]. Since the applied strain kept increasing with time, no relaxation was allowed for the tissue region. The original collected data were the applied strain and the corresponding stress at the tissue surface as a function of time. Afterwards, these data were processed as the stress versus the applied strain. A five-element Maxwell-Wiechert model was found to best fit their experimental data. One coefficient, q_2, in this model was used to quantify the viscoelastic behavior of the breast tissues. Their results indicate that the q_2 coefficient exhibited large or small variation across different healthy regions of the breast, depending on individuals, and varied dramatically among different individuals. This coefficient was lower in the tumor regions than in the healthy regions in seven patients, except two patients showing the opposite. The difference in this coefficient between the healthy regions and the tumor region also varied significantly among different individuals. Therefore, they proposed personalized diagnosis of breast tumor.

In the above-mentioned two studies on breast tumors, significant amount of effort was taken in order to fit the collected data using their models so as to extract the retardation time and the q_2 coefficient. Not all the measured data translated to good fitness to these parameters, since the data over the whole recorded time needed to be matched. In this work, how the stress varied with time at each applied train was not used. Instead, we utilized the quality of fitness of linear

regression for the measured $\Delta\sigma$-ε data to quantify the viscoelastic behavior of the tissue samples. As such, the data-processing algorithm involved in our work is very time-efficient.

Dummy tumors have been embedded into different materials and tissues for facilitating the studies on tumor detection techniques under development [77, 97-103]. Silicone rubber is commonly used as dummy tumors. The elasticity distribution has been measured for tumor detection in those studies. Since silicone rubber exhibits viscous behavior quite different from the native tumor, it is not suggested for tumor detection using the viscosity distribution.

For the first time, this study observed strain-enhanced stress relaxation in the malignant tumors: as the applied strain increases, the tumors exhibited faster stress relaxation (i.e., their relaxation time drops with the applied strain). The observed strain-enhanced stress relaxation suggests that the malignant tumors dissipate elastic energy and diminish strain stiffening over time, with the pace increasing with the applied strain. Interestingly, stress relaxation in the normal tissues measured here remained unchanged with the applied strain. It is tempting to explain this striking difference between the malignant tumors and the normal tissues in terms of their microstructures. According to the literature [57, 104], the collagen fiber bundles (primary structural element of glandular tissue) are straight and less tortuous in malignant breast tumors and tend to be more tortuous and wavy in breast benign tumors and normal tissues. As the applied strain goes up, the stress increases faster and earlier in malignant tumors than in benign tumors and normal tissues. Such nonlinearity was clearly observed in the breast tumors, but not in the normal tissues with/without dummy tumor (Figure 6.10). The force-dependent unbinding of weak bonds between collage fibers might be behind strain-enhanced stress relaxation of collagen gels [105]. Nevertheless, the mechanism behind the strain-enhanced stress relaxation in the malignant tumors needs to be studied. Since the collagen fiber bundles in breast benign

tumors are similar to those in the breast normal tissue, the former could exhibit no correlation between stress drop and applied strain. As such, coefficient of determination has the potential of tumor differentiation.

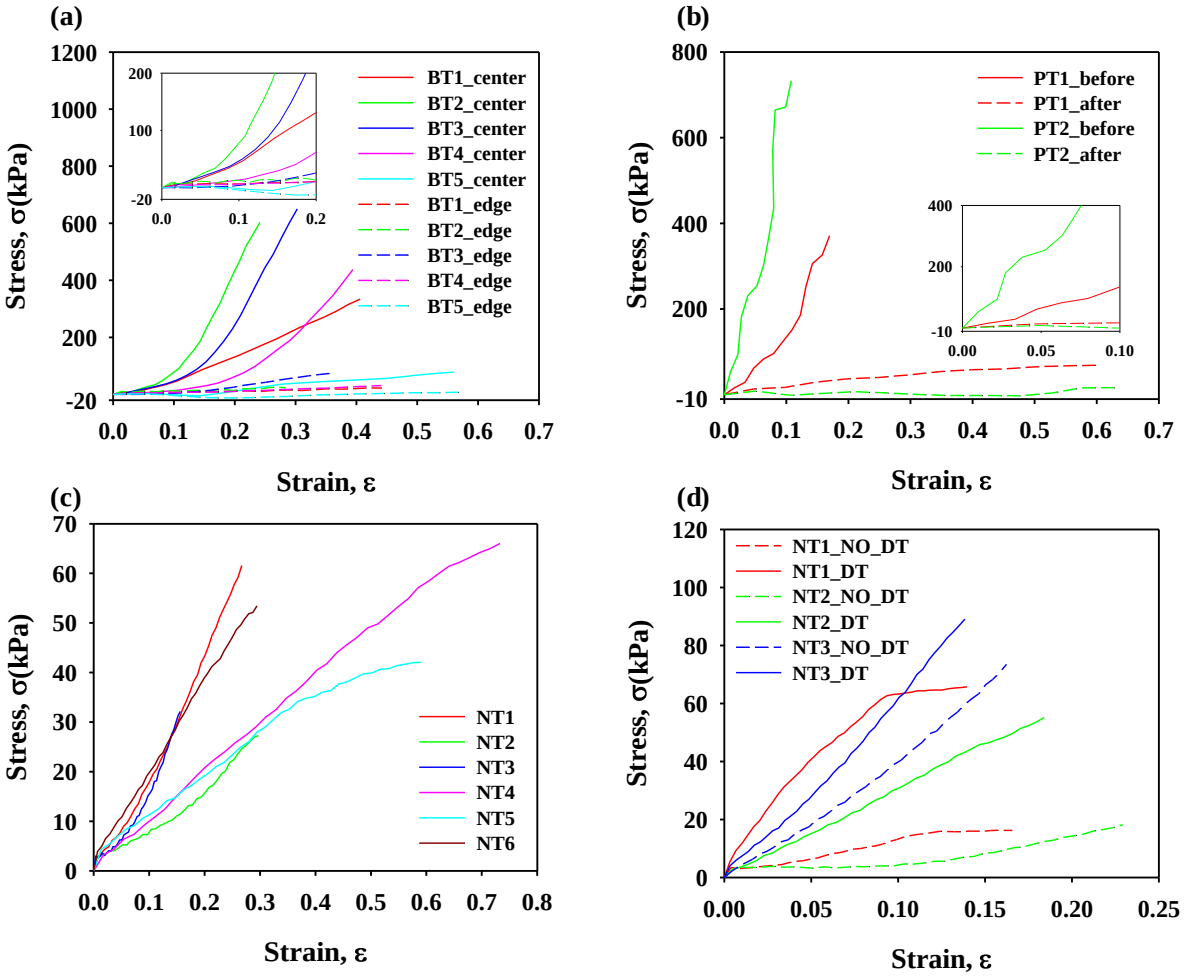

Figure 6.10 Measured stress-strain relation of the (a) tumor center (BT1_center-BT5_center), and tumor edge (BT1_edge-BT5_edge) of the five mouse breast tumor tissues (b) two mouse pancreatic tumor tissues before treatment (PT1_before and PT2_before) and after treatment (PT1_after and PT2_after) (c) three bovine tissues and three porcine tissues (NT1-NT6), and (d) two porcine tissues, one chicken heart (NT1_NO_DT-NT3_NO_DT), and these tissue with embedded dummy tumor (NT1_DT- NT3_DT), respectively.

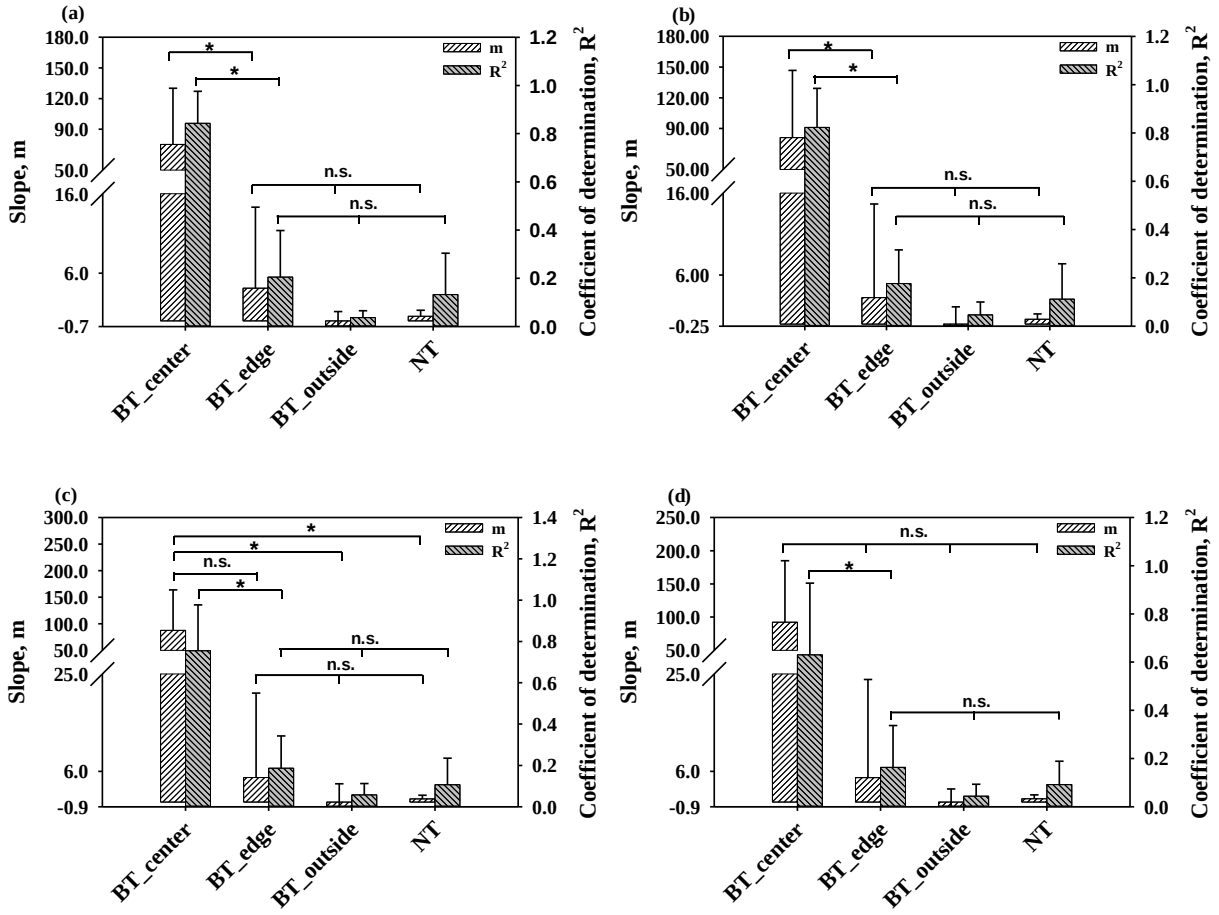

Figure 6.11 Comparison of slope (*m*) and coefficient of determination (R^2) among BT_center sites (L1 and L2), BT_edge sites (L3 and L4), BT_outside sites (L5 and L6) of the three BT tissues (BT1-BT3), and the tissue sites in the two normal porcine tissues (NT4 and NT5) at different pre-compression strain levels (a) 0 (b) 0.05, (c) 0.10, and (d) 0.15. * symbol denotes statistical significance (*p*-value <0.01), and n.s. shows no significant difference

Finally, *ex vivo* tissues behave differently from *in vivo* tissues, since the latter are confined by their surrounding tissues. However, the two *in vivo* PT tissues before treatment exhibited similar behavior as the *ex vivo* BT_center sites, in terms of registering significant difference in m and R^2 from normal tissues for tumor detection. In the future, more *in vivo* measurements need to be conducted for further validating this correlation for *in vivo* tumor detection. Different pre-compression levels in elastography affected the measured elasticity of

different types of tissues in the breast *in vivo* to different extent, including fat tissue [106]. In contrast, except excised fat tissue, the elasticity of all the other tissues of the breast *ex vivo*, including fibrous and glandular tissues and tumors, exhibited dependency on pre-compression level to different extent [107]. The measured difference on fat tissue was attributed to the different conditions: *ex vivo* versus *in vivo*.

For simplicity, we analyzed the measured $\Delta\sigma$-ε data points with different starting applied strain levels on three BT tumors (BT1, BT2, BT3) and two porcine tissues (NT4 and NT5) for examining possible effect of pre-compression on the measured $\Delta\sigma$-ε correlations. The two porcine tissues (skin and fat) were chosen because they were similar to the normal tissue types in the breast. Figure 6.11 compares the values of m and R^2 among the different sites of these three BT tissues and the two normal tissues at different pre-compression strain levels. At all the pre-compression strain levels, R^2 remained its capability of distinguishing the BT_center sites from the rest BT sites and the normal tissues. However, as the pre-compression strain levels went up, m failed to distinguish the BT_center sites from the normal tissues. These observations suggested that a small pre-compression level is preferred for better tumor detection, which is consistent with the *in vivo* results reported in [106].

6.4 Conclusion

In this chapter, we have investigated the feasibility of the measured $\Delta\sigma$-ε relation as a biomarker for tumor detection. Stepwise compression-relaxation testing was utilized to measure the viscoelastic behavior of tumor tissues as the $\Delta\sigma$-ε relation, and Pearson correlation analysis was conducted to quantify the measured $\Delta\sigma$-ε relation as slope of stress drop versus applied strain ($m=\Delta\sigma/\varepsilon$) and coefficient of determination (R^2). While slope was found to have dependency on the testing parameters used, coefficient of determination showed no significant

dependency on them. The value of R^2 revealed significant difference among the BT_center, BT_edge and BT_outside sites of five mouse breast tumor tissues *ex vivo*, and also identify the BT_outside sites as normal tissues. There was also a significant difference of R^2 between before and after treatment of two pancreatic tumor tissues *in vivo*. Meanwhile, the pancreatic tumor tissues after treatment showed no significant difference of R^2 from normal tissues. Despite the variation in the testing parameters used, the value of R^2 differentiated the breast tumors and the pancreatic tumors before treatment. In contrast, the value of m failed to distinguish the pancreatic tumors from the breast tumors and register the pancreatic tumors after treatment as normal tissues, possibly due to the different testing parameters used. Overall, our study on seven mouse tumor tissues and several normal tissues suggests that the correlation between stress drop and applied strain is promising in distinguishing tumor tissues from normal tissues.

CHAPTER 7

CONCLUSION AND FUTURE WORK

7.1 Conclusion

This dissertation focuses on the development of a Stepwise Compression-Relaxation testing method that was implemented on a 2D tactile sensor for measuring tissue mechanical properties and detecting tumors. The specific aims includes: 1) design and develop a tactile sensor with a 2D sensing-plates/transducer array for measuring the mechanical properties of soft tissues; 2) design and develop a mechanical testing method based on the 2D tactile sensor for characterization of the elasticity and viscoelasticity of soft tissues; validate the feasibility of the testing method and investigate the effects of testing parameters on the measured result; and 3) determine the mechanical biomarker from the measured mechanical properties for detection of tumor existence, location, size, and shape; and differentiation among tissue sites of tumor center, edge, outside region, and normal tissues with statistically significant difference. A series of three studies were performed to accomplish the specific aims, which including: 1) experimental study on soft materials to investigate the effects of testing parameters of the SCR testing method on the measured results; 2) experimental study on soft tissues to validate the feasibility of the SCR testing method for measuring their mechanical properties; and 3) experimental study on tumor tissues *ex vivo* and *in vivo* to validate the feasibility of the SCR testing method for distinguishing tumor tissues from normal tissues.

7.1.1 Tissue Characterization Study

The objective of the soft materials study was to create a phantom to mimic the mechanical properties of soft tissues for validation the measured tissue elasticity and investigating the effects of the testing parameters on the measured results. In this dissertation,

nine soft materials were prepared and measured, which include: six PDMS samples with different mixing ratios (curing agent to base of Sylgards 184kit, Dow Corning Corp.) of 1:10, 1:20, and 1:30 and two different thickness, 6mm and 10mm; and three silicone rubbers, Mold Star^{TM}30, Mold Max^{TM} 10T, Dragon Skin$^{®}$ 10.

The measured results of these soft materials was found to be consistent with their values that has been reported in literature [83, 84] and the technical bulletin [85-87]. The same order among the PDMS samples and the silicone rubbers was found in terms elasticity. Statistical analysis on the measured results showed significant differences among these soft materials. The results validated the analytical methods used for extracting the mechanical properties from the measured sensor deflections. A three-factor-three-level factorial design was applied to the experimental data of PDMS samples and silicone rubbers to investigate the effects of testing parameters on the mechanical instant elasticity, $E_{instant}$, loss tangent, tan δ, slope, m, of stress drop and applied strain, and coefficient of determination, R^2. The results from the three-way ANOVA indicated that instant elasticity and loss tangent displayed a significant dependency on the testing parameters, suggesting that only tissues measured using the same testing parameters were comparable based on the measured instant elasticity, $E_{instant}$, loss tangent, tan δ. While slope, m, was found to have dependency on the testing parameters used, but coefficient of determination, R^2, showed no significant dependency on them. This implied that coefficient of determination, R^2 could be used for distinguishing tumor tissues and normal tissues that were measured using different testing parameters, while m is not recommended for distinguishing the tumor tissues from normal tissues which were measured using different testing parameters.

The objective of the tissue characterization study was to validate feasibility of the SCR testing method to characterizing the mechanical properties of soft tissues. In this dissertation,

several groups of normal tissues and tumor tissues were prepared and measured using the SCR testing method, which including porcine and bovine tissues with variable thickness and mechanical properties, five BT tissues, and two PT tissues before treatment and after treatment.

Different mechanical behaviors were found between the muscle tissues and the fat/skin tissues. Furthermore, differences in mechanical behaviors between muscle tissues and PDMS were also observed. Since no correlation exists between elasticity and viscosity for a soft tissue, both properties need to be measured for better differentiation of soft tissues. The *ex vivo* measurement on the five BT tissues showed that the five BT tissues followed the same order: #2, #3, #4, #1 and #5 according to the decreasing elasticity, viscoelasticity, and nonlinearity. The two PT tissues were found to show different elasticity and viscoelasticity between before treatment and after treatment. Overall, the measured results of the soft normal/tumor tissues indicated that the SCR testing method could be used for characterizing the mechanical properties of soft tissues which were important for study the tissue pathologies.

7.1.2 Tumor Detection Study

The objective of the tumor detection study was to develop mechanical biomarkers based on the measured results using the SCR testing method for tumor detection, which including detecting the tumor location, shape, size; differentiation among the tissue sites of tumor center, tumor edge, outside region; and differentiation between tumor tissues and normal tissues.

The measured instant elasticity among the palpated tissue sites of the five BT tissues was used to determine the location, shape and size of the tumor in a BT tissue. These five BT tissues revealed irregular shapes. The value of R^2 revealed significant difference among the tissue sited of the center, edge and outside region of five BT tissues. The outside BT sites were identified as normal tissues. The two PT tissues measured *in vivo* showed a significant difference between

these two tissues before and after treatment; and the two PT tissue after treatment showed no significant difference of R^2 from normal tissues. Overall, the measured results on the soft normal tissues and tumor tissues suggested that the correlation between stress drop and applied strain obtained using the SCR testing method is promising for tumor detection.

7.2 Recommendations for Future Work

First, regarding the sensor used in the SCR testing method, improvements could be made in increasing the spatial resolution and the number of transducers. The current 2D sensor used in the SCR testing method consists a 3×3 sensing-plates/transducer array with a spatial resolution of 1.5mm×3.75mm. Sensor with increased number of transducers and improved spatial resolution for accurate measurement of tissue mechanical properties should be employed in the future. The measurement range of the sensor should be quantified. On the other hand, there is opportunity to improve 2D tactile sensor for *in vivo* measurements of soft tissues at micro and nanoscale. The current 2D tactile sensor used in the SCR testing method can measure the macro-scale mechanical properties of soft tissues in compression, however, it is limited in detecting tumors located well below the limit of manual palpability, such as internal human organs *in vivo* (e.g., liver, lung), which is a common drawback of mechanical imaging methods. Thus, more efforts should be taken into designing and developing novel tactile sensor that could be coupled with Minimally Invasive Surgery (MIS) grasper or internal tissues *in vivo* to identify their mechanical properties at nanoscale.

Second, *in vivo* measurements using the SCR testing method to measure the mechanical properties of both malignant tumor tissues and benign tumor tissues are needed in the future, with the aim to investigate the potential of the SCR testing method to be used for differentiation between malignant and benign tumor tissues. Enough sample size of tumor tissues for statistical

analysis needs to be measured using the same sensor and the same testing parameters including incremental depth, hold time, and ramp speed.

Third, the observed significant differences in m and R^2 between the pancreatic tumor tissues before treatment and after treatment implies that the SCR testing method has the potential to be used for monitoring the cancer treatment failure and success.

REFERENCES

[1] A. C. Society, "Cancer facts&figures 2018," *Atlanta: American Cancer Society,* 2018.

[2] Y. P. Qiu, M. Sridhar, J. K. Tsou *et al.*, "Ultrasonic viscoelasticity imaging of nonpalpable breast tumors: preliminary results," *Academic Radiology,* vol. 15, no. 12, pp. 1526-1533, Dec, 2008.

[3] C. R. Gentle, "Mammobarography - a possible method of mass breast screening," *Journal of Biomedical Engineering,* vol. 10, no. 2, pp. 124-126, Apr, 1988.

[4] H. Shojaku, H. Seto, H. Iwai *et al.*, "Detection of incidental breast tumors by noncontrast spiral computed tomography of the chest," *Radiation Medicine,* vol. 26, no. 6, pp. 362-367, Jul, 2008.

[5] H. Degani, V. Gusis, D. Weinstein *et al.*, "Mapping pathophysiological features of breast tumors by MRI at high spatial resolution," *Nature Medicine,* vol. 3, no. 7, pp. 780-782, Jul, 1997.

[6] C. M. Sehgal, S. P. Weinstein, P. H. Arger *et al.*, "A review of breast ultrasound," *Journal of Mammary Gland Biology and Neoplasia,* vol. 11, no. 2, pp. 113-123, Apr, 2006.

[7] J. H. Lee, and C. H. Won, "The tactile sensation imaging system for embedded lesion characterization," *IEEE Journal of Biomedical and Health Informatics,* vol. 17, no. 2, pp. 452-458, Mar, 2013.

[8] Y. Wang, and M. F. Insana, "Viscoelastic properties of rodent mammary tumors using ultrasonic shear-wave imaging," *Ultrasonic Imaging,* vol. 35, no. 2, pp. 126-145, Apr, 2013.

[9] E. I. Deryugina, and J. P. Quigley, "The role of matrix metalloproteinases in cellular invasion and metastasis," *Extracellular Matrix Degradation,* pp. 145-191, 2011.

[10] P. F. Lu, K. Takai, V. M. Weaver *et al.*, "Extracellular matrix degradation and remodeling in development and disease," *Cold Spring Harbor Perspectives in Biology,* vol. 3, no. 12, Dec, 2011.

[11] A. Mangia, A. Malfettone, R. Rossi *et al.*, "Tissue remodelling in breast cancer: human mast cell tryptase as an initiator of myofibroblast differentiation," *Histopathology,* vol. 58, no. 7, pp. 1096-1106, Jun, 2011.

[12] R. Roy, W. J. Chen, L. A. Goodell *et al.*, "Microarray-facilitated mechanical characterization of breast tissue pathology samples using contact-mode atomic force microscopy (AFM)," *2010 3rd IEEE Ras and Embs International Conference on Biomedical Robotics and Biomechatronics,* pp. 710-715, 2010.

[13] V. Egorov, T. Kearney, S. B. Pollak *et al.*, "Differentiation of benign and malignant breast lesions by mechanical imaging," *Breast Cancer Research and Treatment,* vol. 118, no. 1, pp. 67-80, Nov, 2009.

[14] R. G. Barr, "Real-time ultrasound elasticity of the breast initial clinical results," *Ultrasound Quarterly,* vol. 26, no. 2, pp. 61-66, Jun, 2010.

[15] T. Xydeas, K. Siegmann, R. Sinkus *et al.*, "Magnetic resonance elastography of the breast - correlation of signal intensity data with viscoelastic properties," *Investigative Radiology,* vol. 40, no. 7, pp. 412-420, Jul, 2005.

[16] B. F. Kennedy, R. A. McLaughlin, K. M. Kennedy *et al.*, "Investigation of optical coherence microelastography as a method to visualize cancers in human breast tissue," *Cancer Research,* vol. 75, no. 16, pp. 3236-3245, 2015.

[17] M. Ayyildiz, B. Guclu, M. Z. Yildiz *et al.*, "An optoelectromechanical tactile sensor for detection of breast lumps," *IEEE Transactions on Haptics,* vol. 6, no. 2, pp. 145-155, Apr-Jun, 2013.

[18] P. S. Wellman, and R. D. Howe, "Extracting features from tactile maps," *Medical Image Computing and Computer-Assisted Intervention, Miccai'99, Proceedings,* vol. 1679, pp. 1133-1142, 1999.

[19] X. Xu, C. Gifford-Hollingsworth, R. Sensenig *et al.*, "Breast tumor detection using piezoelectric fingers: first clinical report," *Journal of the American College of Surgeons,* vol. 216, no. 6, pp. 1168-1173, Jun, 2013.

[20] M. M. Doyley, "Model-based elastography: a survey of approaches to the inverse elasticity problem," *Physics in Medicine and Biology,* vol. 57, no. 3, pp. R35-R73, Feb 7, 2012.

[21] J. R. Grajo, and R. G. Barr, "Compression elasticity imaging of the breast: an overview," *Applied Radiology,* vol. 41, no. 10, pp. 18, 2012.

[22] J. Bishop, A. Samani, J. Sciarretta *et al.*, "Two-dimensional MR elastography with linear inversion reconstruction: methodology and noise analysis," *Physics in medicine and biology,* vol. 45, no. 8, pp. 2081, 2000.

[23] J. B. Weaver, E. E. Van Houten, M. I. Miga *et al.*, "Magnetic resonance elastography using 3D gradient echo measurements of steady-state motion," *Medical Physics,* vol. 28, no. 8, pp. 1620-1628, 2001.

[24] S. J. Kirkpatrick, R. K. Wang, and D. D. Duncan, "OCT-based elastography for large and small deformations," *Optics Express,* vol. 14, no. 24, pp. 11585-11597, Nov 27, 2006.

[25] H. J. Ko, W. Tan, R. Stack *et al.*, "Optical coherence elastography of engineered and developing tissue," *Tissue Engineering,* vol. 12, no. 1, pp. 63-73, Jan, 2006.

[26] M. S. Taljanovic, L. H. Gimber, G. W. Becker *et al.*, "Shear-wave elastography: basic physics and musculoskeletal applications," *Radiographics,* vol. 37, no. 3, pp. 855-870, 2017.

[27] A. Goddi, M. Bonardi, and S. Alessi, "Breast elastography: a literature review," *Journal of ultrasound,* vol. 15, no. 3, pp. 192-198, 2012.

[28] X. Gong, Y. Wang, and P. Xu, "Application of real-time ultrasound elastography for differential diagnosis of breast tumors," *Journal of Ultrasound in Medicine,* vol. 32, no. 12, pp. 2171-2176, Dec, 2013.

[29] L. Huwart, F. Peeters, R. Sinkus *et al.*, "Liver fibrosis: non‐invasive assessment with MR elastography," *NMR in Biomedicine: An International Journal Devoted to the Development and Application of Magnetic Resonance In vivo,* vol. 19, no. 2, pp. 173-179, 2006.

[30] C. Balleyguier, A. B. Lakhdar, A. Dunant *et al.*, "Value of whole breast magnetic resonance elastography added to MRI for lesion characterization," *NMR in Biomedicine,* vol. 31, no. 1, pp. e3795, 2018.

[31] Y.-c. Fung, *Biomechanics: mechanical properties of living tissues*: Springer Science & Business Media, 2013.

[32] M. Sridhar, J. Liu, and M. F. Insana, "Elasticity imaging of polymeric media," *Journal of Biomechanical Engineering-Transactions of the Asme,* vol. 129, no. 2, pp. 259-272, Apr, 2007.

[33] M. Sridhar, J. Liu, and M. F. Insana, "Viscoelasticity imaging using ultrasound: parameters and error analysis," *Physics in Medicine and Biology,* vol. 52, no. 9, pp. 2425-2443, May 7, 2007.

[34] S. Catheline, J. L. Gennisson, G. Delon *et al.*, "Measurement of viscoelastic properties of homogeneous soft solid using transient elastography: an inverse problem approach," *Journal of the Acoustical Society of America,* vol. 116, no. 6, pp. 3734-3741, Dec, 2004.

[35] K. Hoyt, B. Castaneda, and K. J. Parker, "Two-dimensional sonoelastographic shear velocity imaging," *Ultrasound in Medicine and Biology,* vol. 34, no. 2, pp. 276-288, Feb, 2008.

[36] L. A. Taber, "Nonlinear theory of elasticity: applications in biomechanics," *World Scientific*, 2004.

[37] A. Sarvazyan, "Mechanical imaging: A new technology for medical diagnostics," *International Journal of Medical Informatics,* vol. 49, no. 2, pp. 195-216, Apr, 1998.

[38] F. J. Carter, T. G. Frank, P. J. Davies *et al.*, "Measurements and modelling of the compliance of human and porcine organs," *Medical Image Analysis,* vol. 5, no. 4, pp. 231-236, Dec, 2001.

[39] P. S. Wellman, R. D. Howe, N. Dewagan *et al.*, "Tactile imaging: a method for documenting breast masses." p. 1131 vol. 2.

[40] P. S. Wellman, E. P. Dalton, D. Krag *et al.*, "Tactile imaging of breast masses - First clinical report," *Archives of Surgery,* vol. 136, no. 2, pp. 204-208, Feb, 2001.

[41] V. Vuskovic, "Device for in-vivo measurement of mechanical properties of internal human soft tissues," Diss., Technische Wissenschaften ETH Zürich, Nr. 14222, 2001, 2001.

[42] D. Valtorta, and E. Mazza, "Dynamic measurement of soft tissue viscoelastic properties with a torsional resonator device," *Medical Image Analysis,* vol. 9, no. 5, pp. 481-490, Oct, 2005.

[43] J. Rosen, J. D. Brown, S. De *et al.*, "Biomechanical properties of abdominal organs in vivo and postmortem under compression loads," *Journal of Biomechanical Engineering-Transactions of the Asme,* vol. 130, no. 2, Apr, 2008.

[44] B. Ahn, and J. Kim, "Measurement and characterization of soft tissue behavior with surface deformation and force response under large deformations," *Medical image analysis,* vol. 14, no. 2, pp. 138-148, 2010.

[45] A. Nabavizadeh, R. R. Kinnick, M. Bayat *et al.*, "Automated Compression Device for Viscoelasticity Imaging," *IEEE Transactions on Biomedical Engineering*, 2016.

[46] X. Wang, J. A. Schoen, and M. E. Rentschler, "A quantitative comparison of soft tissue compressive viscoelastic model accuracy," *Journal of the mechanical behavior of biomedical materials,* vol. 20, pp. 126-136, 2013.

[47] J. Palacio-Torralba, S. Hammer, D. W. Good *et al.*, "Quantitative diagnostics of soft tissue through viscoelastic characterization using time-based instrumented palpation," *journal of the mechanical behavior of biomedical materials,* vol. 41, pp. 149-160, 2015.

[48] B. An, and J. Kim, "Dynamic measurement and modeling of soft tissue behavior with an indentation device using indenters of various shapes." pp. 781-784.

[49] P. Scanlan, S. Hammer, D. Good *et al.*, "Development of a novel actuator for the dynamic palpation of soft tissue for use in the assessment of prostate tissue quality," *Sensors and Actuators A: Physical,* vol. 232, pp. 310-318, 2015.

[50] A. Sarvazyan, V. Egorov, J. Son *et al.*, "Cost-effective screening for breast cancer worldwide: current state and future directions," *Breast cancer: basic and clinical research,* vol. 1, pp. 91, 2008.

[51] V. Egorov, and A. P. Sarvazyan, "Mechanical imaging of the breast," *IEEE Transactions on Medical Imaging,* vol. 27, no. 9, pp. 1275-1287, Sep, 2008.

[52] A. P. Sarvazyan, and V. Egorov, "Mechanical imaging in medical applications," *2009 Annual International Conference of the IEEE Engineering in Medicine and Biology Society, Vols 1-20,* pp. 1975-1978, 2009.

[53] S. E. Cross, Y. S. Jin, J. Rao *et al.*, "Nanomechanical analysis of cells from cancer patients," *Nature Nanotechnology,* vol. 2, no. 12, pp. 780-783, Dec, 2007.

[54] M.-K. Tasoulis, K. E. Zacharioudakis, N. G. Dimopoulos *et al.*, "Diagnostic accuracy of tactile imaging in selecting patients with palpable breast abnormalities: a prospective comparative study," *Breast cancer research and treatment,* vol. 147, no. 3, pp. 589-598, 2014.

[55] M. K. Markey, *Physics of mammographic imaging*: Taylor & Francis, 2012.

[56] A. Sayed, G. Layne, J. Abraham *et al.*, "Nonlinear characterization of breast cancer using multi-compression 3D ultrasound elastography in vivo," *Ultrasonics,* vol. 53, no. 5, pp. 979-991, Jul, 2013.

[57] S. Goenezen, J.-F. Dord, Z. Sink *et al.*, "Linear and nonlinear elastic modulus imaging: an application to breast cancer diagnosis," *IEEE transactions on medical imaging,* vol. 31, no. 8, pp. 1628-1637, 2012.

[58] R. M. Sigrist, J. Liau, A. El Kaffas *et al.*, "Ultrasound elastography: review of techniques and clinical applications," *Theranostics,* vol. 7, no. 5, pp. 1303, 2017.

[59] D. W. Good, G. D. Stewart, S. Hammer *et al.*, "Elasticity as a biomarker for prostate cancer: a systematic review," *BJU international,* vol. 113, no. 4, pp. 523-534, 2014.

[60] K. Hoyt, B. Castaneda, M. Zhang *et al.*, "Tissue elasticity properties as biomarkers for prostate cancer," *Cancer Biomarkers,* vol. 4, no. 4-5, pp. 213-225, 2008.

[61] N. Madani, and A. Mojra, "Quantitative diagnosis of breast tumors by characterization of viscoelastic behavior of healthy breast tissue," *Journal of the mechanical behavior of biomedical materials,* vol. 68, pp. 180-187, 2017.

[62] M. Bayat, A. Nabavizadeh, V. Kumar *et al.*, "Automated in vivo sub-Hertz analysis of viscoelasticity (SAVE) for evaluation of breast lesions," *IEEE Transactions on Biomedical Engineering*, 2017.

[63] H. Zhang, Y. Wang, and M. F. Insana, "Ramp-hold relaxation solutions for the KVFD model applied to soft viscoelastic media," *Measurement Science and Technology,* vol. 27, no. 2, pp. 025702, 2016.

[64] H. Zhang, Q. zhe Zhang, L. Ruan *et al.*, "Modeling ramp-hold indentation measurements based on Kelvin–Voigt fractional derivative model," *Measurement Science and Technology,* vol. 29, no. 3, pp. 035701, 2018.

[65] S. Oman, and M. Nagode, "Observation of the relation between uniaxial creep and stress relaxation of filled rubber," *Materials & Design,* vol. 60, pp. 451-457, 2014.

[66] O. Bas, E. M. De-Juan-Pardo, C. Meinert *et al.*, "Biofabricated soft network composites for cartilage tissue engineering," *Biofabrication,* vol. 9, no. 2, pp. 025014, 2017.

[67] C. Bougault, L. Cueru, J. Bariller *et al.*, "Alteration of cartilage mechanical properties in absence of β1 integrins revealed by rheometry and FRAP analyses," *Journal of biomechanics,* vol. 46, no. 10, pp. 1633-1640, 2013.

[68] A. A. Jutila, D. L. Zignego, W. J. Schell *et al.*, "Encapsulation of chondrocytes in high-stiffness agarose microenvironments for in vitro modeling of osteoarthritis mechanotransduction," *Annals of biomedical engineering,* vol. 43, no. 5, pp. 1132-1144, 2015.

[69] D. G. Seifu, S. Meghezi, L. Unsworth *et al.*, "Viscoelastic properties of multi-layered cellularized vascular tissues fabricated from collagen gel," *Journal of the mechanical behavior of biomedical materials,* vol. 80, pp. 155-163, 2018.

[70] Y. Yang, S. Guo, and Z. Hao, "Mechanical characterization of mouse mammary tumors via a two-dimensional (2D) distributed-deflection sensor," *Sensors,* vol. 16116, pp. 1, 2016.

[71] W. T. Gu, P. Cheng, A. Ghosh *et al.*, "Detection of distributed static and dynamic loads with electrolyte-enabled distributed transducers in a polymer-based microfluidic device," *Journal of Micromechanics and Microengineering,* vol. 23, no. 3, Mar, 2013.

[72] J. Konstantinova, A. Jiang, K. Althoefer *et al.*, "Implementation of tactile sensing for palpation in robot-assisted minimally invasive surgery: A review," *IEEE Sensors Journal,* vol. 14, no. 8, pp. 2490-2501, 2014.

[73] P. Cheng, W. T. Gu, J. Y. Shen *et al.*, "Performance study of a PDMS-based microfluidic device for the detection of continuous distributed static and dynamic loads," *Journal of Micromechanics and Microengineering,* vol. 23, no. 8, Aug, 2013.

[74] Y. Yang, G. D. Johnson, D. J. Krusienski *et al.*, "A Microfluidic-based Tactile Sensor for Palpating Mice Tumor Tissues." pp. 83-92.

[75] A. V. Jagtiani, J. Carletta, and J. Zhe, "A microfluidic multichannel resistive pulse sensor using frequency division multiplexing for high throughput counting of micro particles," *Journal of Micromechanics and Microengineering,* vol. 21, no. 6, pp. 065004, 2011.

[76] W. Gu, P. Cheng, X.-L. Palmer *et al.*, "Concurrent spatial mapping of the elasticity of heterogeneous soft materials via a polymer-based microfluidic device," *Journal of Micromechanics and Microengineering,* vol. 23, no. 10, pp. 105007, 2013.

[77] Y. Yang, S. Guo, and Z. Hao, "A two-dimensional (2D) distributed-deflection sensor for tissue palpation with correction mechanism for its performance variation," *IEEE Sensors Journal,* vol. 16, no. 11, pp. 4219-4229, 2016.

[78] E. K. Dimitriadis, F. Horkay, J. Maresca *et al.*, "Determination of elastic moduli of thin layers of soft material using the atomic force microscope," *Biophysical journal,* vol. 82, no. 5, pp. 2798-2810, 2002.

[79] K. L. Johnson, and K. L. Johnson, *Contact mechanics*: Cambridge university press, 1987.

[80] C. S. Brazel, and S. L. Rosen, *Fundamental principles of polymeric materials*: John Wiley & Sons, 2012.

[81] Q. Xu, and B. Engquist, "A mathematical and physical model improves accuracy in simulating solid material relaxation modulus and viscoelastic responses," *arXiv preprint arXiv:1412.5225,* 2014.

[82] J. T. Iivarinen, R. K. Korhonen, P. Julkunen *et al.*, "Experimental and computational analysis of soft tissue stiffness in forearm using a manual indentation device," *Medical engineering & physics,* vol. 33, no. 10, pp. 1245-1253, 2011.

[83] J. Y. Park, S. J. Yoo, E.-J. Lee *et al.*, "Increased poly (dimethylsiloxane) stiffness improves viability and morphology of mouse fibroblast cells," *BioChip Journal,* vol. 4, no. 3, pp. 230-236, 2010.

[84] A. Sharfeddin, A. A. Volinsky, G. Mohan *et al.*, "Comparison of the macroscale and microscale tests for measuring elastic properties of polydimethylsiloxane," *Journal of Applied Polymer Science,* vol. 132, no. 42, 2015.
[85] "https://www.smooth-on.com/tb/files/MOLD_STAR_15_16_30_TB.pdf."
[86] "https://www.smooth-on.com/tb/files/MOLD_MAX_10T_15T_27T_TB.pdf."
[87] "https://www.smooth-on.com/tb/files/DRAGON_SKIN_SERIES_TB.pdf."
[88] Z. Hajjarian, and S. K. Nadkarni, "Evaluating the viscoelastic properties of tissue from laser speckle fluctuations," *Scientific reports,* vol. 2, pp. 316, 2012.
[89] J. L. Sparks, N. A. Vavalle, K. E. Kasting *et al.*, "Use of silicone materials to simulate tissue biomechanics as related to deep tissue injury," *Advances in skin & wound care,* vol. 28, no. 2, pp. 59-68, 2015.
[90] S. Ranamukhaarachchi, S. Lehnert, S. Ranamukhaarachchi *et al.*, "A micromechanical comparison of human and porcine skin before and after preservation by freezing for medical device development," *Scientific reports,* vol. 6, 2016.
[91] N. Lu, C. Lu, S. Yang *et al.*, "Highly sensitive skin-mountable strain gauges based entirely on elastomers," *Advanced Functional Materials,* vol. 22, no. 19, pp. 4044-4050, 2012.
[92] B. Qiang, J. Greenleaf, M. Oyen *et al.*, "Estimating material elasticity by spherical indentation load-relaxation tests on viscoelastic samples of finite thickness," *IEEE transactions on ultrasonics, ferroelectrics, and frequency control,* vol. 58, no. 7, pp. 1418-1429, 2011.
[93] M. Van Loocke, C. Lyons, and C. Simms, "Viscoelastic properties of passive skeletal muscle in compression: stress-relaxation behaviour and constitutive modelling," *Journal of biomechanics,* vol. 41, no. 7, pp. 1555-1566, 2008.
[94] K. Tao, M. Fang, J. Alroy *et al.*, "Imagable 4T1 model for the study of late stage breast cancer," *BMC cancer,* vol. 8, no. 1, pp. 228, 2008.
[95] C. M. Edelblute, J. Hornef, N. I. Burcus *et al.*, "Controllable moderate heating enhances the therapeutic efficacy of irreversible electroporation for pancreatic cancer," *Scientific reports,* vol. 7, no. 1, pp. 11767, 2017.
[96] Y. Yang, S. Guo, and Z. Hao, "Correlation between stress drop and applied strain as a biomarker for tumor detection," *Journal of the Mechanical Behavior of Biomedical Materials,* 2018.
[97] A. Garg, S. Sen, R. Kapadia *et al.*, "Tumor localization using automated palpation with gaussian process adaptive sampling." pp. 194-200.
[98] H. M. Ismail, C. G. Pretty, M. K. Signal *et al.*, "Finite element modelling and validation for breast cancer detection using digital image elasto-tomography," *Medical & biological engineering & computing,* pp. 1-15, 2018.
[99] H. M. Ismail, C. G. Pretty, M. K. Signal *et al.*, "Mechanical behaviour of tissue mimicking breast phantom materials," *Biomedical Physics & Engineering Express,* vol. 3, no. 4, pp. 045010, 2017.
[100] G. L. McCreery, A. L. Trejos, R. V. Patel *et al.*, "Evaluation of force feedback requirements for minimally invasive lung tumour localization." pp. 883-888.
[101] Y. Murayama, M. Haruta, Y. Hatakeyama *et al.*, "Development of a new instrument for examination of stiffness in the breast using haptic sensor technology," *Sensors and Actuators A: Physical,* vol. 143, no. 2, pp. 430-438, 2008.

[102] A. S. Naidu, R. V. Patel, and M. D. Naish, "Low-cost disposable tactile sensors for palpation in minimally invasive surgery," *IEEE/ASME Transactions on Mechatronics,* vol. 22, no. 1, pp. 127-137, 2017.

[103] H. Xie, H. Liu, L. D. Seneviratne *et al.*, "An optical tactile array probe head for tissue palpation during minimally invasive surgery," *IEEE Sensors Journal,* vol. 14, no. 9, pp. 3283-3291, 2014.

[104] G. Falzon, S. Pearson, and R. Murison, "Analysis of collagen fibre shape changes in breast cancer," *Physics in Medicine & Biology,* vol. 53, no. 23, pp. 6641, 2008.

[105] S. Nam, K. H. Hu, M. J. Butte *et al.*, "Strain-enhanced stress relaxation impacts nonlinear elasticity in collagen gels," *Proceedings of the National Academy of Sciences,* vol. 113, no. 20, pp. 5492-5497, 2016.

[106] R. G. Barr, and Z. Zhang, "Effects of precompression on elasticity imaging of the breast: development of a clinically useful semiquantitative method of precompression assessment," *Journal of Ultrasound in Medicine,* vol. 31, no. 6, pp. 895-902, 2012.

[107] T. A. Krouskop, T. M. Wheeler, F. Kallel *et al.*, "Elastic moduli of breast and prostate tissues under compression," *Ultrasonic imaging,* vol. 20, no. 4, pp. 260-274, 1998.

VITA

Yichao Yang received his B.S. degree in Measurement and Control Technology and Instrumentation from Yantai University, Yantai, China, in 2009 and received his M.E. degree in Control Engineering from University of Electronic Science and Technology of China, Chengdu, China, in 2013, respectively. He is currently a Ph.D. candidate in the Department of Mechanical and Aerospace Engineering at Old Dominion University. He has been working on the design, modeling, fabrication, characterization, and application of polymer-based microfluidic sensors since 2013. His research interests are development of mechanical testing method based on microfluidic/micro sensors for mechanical characterizations of soft tissue and tumor detections.